

https://dspace.org/

Experimental investigation of weak irregular shock wave reflections

Li, Gavin Sun Man

2010-03-25T06:10:53Z
http://hdl.handle.net/10539/7800

Downloaded from a DSpace repository. https://dspace.org/

Declaration

I declare that this dissertation is my own, unaided work, except where otherwise acknowledged. It is being submitted for the degree of Master of Science in Engineering in the University of the Witwatersrand, Johannesburg. It has not been submitted before for any degree or examination at any other university.

Signed this __ day of _____ 20__

_____

Gavin Sun Man Li

Acknowledgements

Firstly, I would like to thank my supervisor, Professor B. W. Skews, for giving me this great opportunity to undertake this challenging project. I would not make it this far without his guidance and advice.

Thanks to Mr. Antun Andreis, for helping me with all the equipment around the laboratory, and who taught me a lot about optical systems.

Thanks to Dr. Craig Law and Mr. Randall Paton, for their assistance with the Computational Fluid Dynamics (CFD) simulations.

Thanks to Mr. Jason Ashworth and Mr. Ralf Wintjens, for the design and modifications to improve the shock tube.

Thanks to Mr. John Cooper and the Laboratory staff, for their technical advice and modifications done on the shock tube.

Last but not least, thanks to my family and friends for all their support during both good and bad times.

Published Work

The following paper has been submitted to the journal Shock Waves:

Skews B. W., Li G., Paton R., *Experiments on Guderley reflection*, J. Shock Wave, 2008.

Abstract

An experimental investigation of weak shock wave reflections was conducted with the large scale shock tube in the Flow Research Unit, in the Mechanical Engineering Laboratory, at the University of the Witwatersrand, Johannesburg. The purpose of the study was to expand the current understanding of irregular shock wave reflections, especially the von Neumann reflection (vNR) and the Guderley reflection (GR). The experiments were conducted using a high sensitivity schlieren system for three Mach numbers in the region around M 1.10 with single-frame and multiple-frame cameras. The single-frame photographs were taken to visualise the sequences of expansion fans and shocklets behind the reflected shock wave, while the multiple-frame photographs were taken using a million-frame per second camera for the velocity calculation in the region near the triple point indicated in oblique shock wave theory. Most of the single-frame photographs show the first set of expansion fans and associated shocklet clearly, while a few of them show signs of the second set of expansion fans and shocklet. The third expansion fan is not very clear on some photographs, and there is no sign of the third shocklet at all. Most of the multiple-frame photographs were useful for the oblique shock calculations. The work done is the first time to obtain quantitative data on flow through a Guderley reflection. The lower burst pressure (1.8 bar) tests were proven to be most successful for the study while the higher burst pressure (3 bar) tests showed contradictions to the physical meaning of the flow behind the reflected shock wave. This is due to the assumption of plane shock waves in the oblique shock calculations, recognizing that the physical shock wave has a very large curvature and the substantial weakness of the reflected wave, being close to sonic conditions. Some primary computational fluid dynamics (CFD) simulations using an Euler code, were also conducted to inform the design of a new insert to vary the angle of the divergent section of the shock tube to improve the visibility of the expansion fans and shocklets behind the reflected shock wave. The new insert has not been tested due to time constraint.

Table of Contents

Declaration ..... **i**
Acknowledgements ..... **ii**
Published Work ..... **iii**
Abstract ..... **iv**
Table of Contents ..... **v**
List of Figures ..... **viii**
List of Tables ..... **xii**
List of Symbols ..... **xiii**
1 Introduction **1**
2 Background and Motivation **8**
2.1 Types of Shock Wave Reflections **8**
2.2 The von Neumann Paradox **10**
2.3 Oblique Shock Theory **13**
2.4 Schlieren Optical System **14**
3 Objectives **17**
4 Apparatus **18**
4.1 The Blue Shock Tube **18**
4.2 Control Panel **21**
4.3 Data Acquisition and Instrumentation **22**
4.4 Optical System **24**
4.4.1 Schlieren System 24
4.4.2 Contact Shadowgraph System 25
4.4.3 Light Sources 25
4.4.4 The Knife Edge 27
4.4.5 The Lenses 28
4.4.6 Parabolic Mirrors 29
4.4.7 Single-frame Camera 30
4.4.8 Multiple-frame Camera System 30
4.5 Diaphragm **31**

5 Experimental Procedure 32
5.1 Testing Procedure 32
5.2 Precautions 33
6 Results 35
6.1 Computational Investigation 35
6.2 Experimental Results 42
6.2.1 Single-frame Photographs 42
6.2.2 Multiple-frame Photographs 49
6.3 Data processing 57
6.3.1 Assumptions 57
6.3.2 Image Processing 57
6.3.3 Image Processing Procedure 59
6.3.4 Sample Calculations 61
6.3.5 Oblique Shock Calculations (Primary) 64
6.3.6 Oblique Shock Calculations (Secondary) 70
6.4 Pressure Traces 74
7 Discussion 78
7.1 Numerical Data 78
7.2 Experimental Data 82
7.2.1 Single-frame Photographs 83
7.2.2 Multiple-frame Photographs 87
7.3 Contact Shadowgraph Photography 88
7.4 Oblique Shock Wave Calculations (Primary) 89
7.5 Oblique Shock Wave Calculations (Secondary) 91
7.6 Pressure Traces 92
8 Conclusion 94
8.1 CFD Investigation 94
8.2 Schlieren Photographs 94
8.3 Contact Shadowgraph Photograph 95
8.4 Oblique Shock Wave Calculations 95
8.5 Pressure Traces 95
9 Recommendations 96
9.1 CFD Investigation 96
9.2 Photographic System 96
9.3 Oblique Shock Calculations 96
9.4 Blue Shock Tube 96
10 References 97

Appendix A – CFD.....99
Appendix B – EES and Matlab Calculations 101
Appendix C – Solid Edge Drawings 108
Appendix D – Xenon Light Sources Specifications.....113
Appendix E – Photographs DVD.....119

List of Figures

Figure 1: Schlieren photograph of a von Neumann reflection for weak shock (M_i = 1.10 and θ_w = 20°) (Kobayashi et al., 2004)..... 1
Figure 2: Schematic diagram of a Guderley reflection (GR) (Skews, 2006) 3
Figure 3: Schematic diagram of the structure of weak shock reflection (Hunter et al., 2000).. 4
Figure 4: The size of the supersonic region (Zakharian et al., 2000) 5
Figure 5: The structure near the triple point with a sequence of shocks, expansion fans, triple point and supersonic patches behind the reflection wave. The dashed line is the sonic line. (Hunter et al., 2002) 6
Figure 6: Schematic illustration of the three types of reflection: vNR, ?R and GR. Light gray regions are subsonic. (Vasilev et al., 2007)..... 7
Figure 7: Modified evolution-tree type presentation of the wave configurations of various types of shock wave reflection (Ben-Dor, 2006)..... 8
Figure 8: von Neumann reflection, (a) schematic illustration, (b) schlieren photograph. (Ben-Dor, 2006) 9
Figure 9: Single Mach reflection, (a) schematic illustration (b) interferometric photograph. (Ben-Dor, 2006) 10
Figure 10: (top) Incident shock wave, i, passing over a concave corner; (middle) Display of "von Neumann paradox": comparison of von Neumann's three-shock theory with experimental data (Bleakney, 1949) for strong (ξ = 0.2) and weak (ξ = 0.9) cases; (bottom) Comparison of the shock wave angles (β_s, β_1 given by the von Neumann theory with their experimental data at the triple point. (Sakurai et al., 1989)..... 11
Figure 11: Triple point reference frame and the shock polar (Kobayashi et al., 1995)..... 12
Figure 12: Supersonic flow over a concave corner (Skews, 2001) 13
Figure 13: Transformation of an oblique shock into a normal shock (Skews, 2001)..... 13
Figure 14: Basic schlieren system (Kodak, 1960)..... 14
Figure 15: Different sensitivity single mirror schlieren system (Kodak, 1960)..... 15
Figure 16: Different type of double mirror schlieren system (Kodak, 1960)..... 16
Figure 17: Schematic diagram of the blue shock tube with dimensions in mm (Skews et al., 2006)..... 18
Figure 18: The full size configuration of the blue shock tube (with castors)..... 19

Figure 19: Another view of the blue shock tube (without castors)..... 19
Figure 20: Another configuration of the blue shock tube..... 20
Figure 21: Another view of the second configuration of the blue shock tube..... 20
Figure 22: The control panel 21
Figure 23: Data Acquisition system, Yokogawa DL1540 digital oscilloscope (left) and Time Delay Unit (middle), Signal Conditioner (right). 22
Figure 24: Configurations of the four pressure transducer on the shock tube (Skews et al., 2006)..... 23
Figure 25: Positions of the four pressure transducers related to the test section in mm (Skews et al., 2006) (modified)..... 23
Figure 26: Two-mirror schlieren optical system used for single-frame and multi-frame photography (Kodak, 1960)..... 24
Figure 27: Typical contact shadowgraph setup (modified from Kodak, 1960)..... 25
Figure 28: L2437 15 watts xenon flash lamp with power supply 26
Figure 29: L6604 60 watts xenon flash lamp with power supply and capacitor 26
Figure 30: General Electric 650 watts continuous lamp in the housing and variable power supply 27
Figure 31: The first knife edge at the light source station 27
Figure 32: The second knife edge with its stand at the camera station 28
Figure 33: Different types of lenses used 29
Figure 34: 12.5 inch diameter parabolic mirror on its stand 29
Figure 35: 4 inch diameter parabolic mirror..... 30
Figure 36: Density contours for 15° ramp angle as the triple point enters test section. 36
Figure 37: Shock wave entering the test sections for the 15° ramp. 36
Figure 38: Shock wave at the centre of the test sections for the 15° ramp. 37
Figure 39: Shock wave leaving the test section for the 15 degree ramp. 37
Figure 40: Density contours for 10° ramp angle as the triple point enters test section. 38
Figure 41: Shock wave entering the test section for the 10° ramp. 38
Figure 42: Shock wave at the centre of the test section for the 10° ramp. 39
Figure 43: Shock wave leaving the test section for the 10° ramp. 39
Figure 44: Density Contours for 20° ramp angle as triple point enters test section. 40
Figure 45: Shock wave entering the test section for the 20° ramp. 40
Figure 46: Shock wave at the centre of the test section of the 20° ramp..... 41
Figure 47: Shock wave leaving the test section of the 20° ramp..... 41
Figure 48: Schlieren photograph B221825A..... 43
Figure 49: Schlieren photograph B221900B 44
Figure 50: Schlieren photograph F221900B 44

Figure 51: Schlieren photograph G221900A 44
Figure 52: Schlieren photograph G321800A 45
Figure 53: Schlieren photograph K222000A 45
Figure 54: Schlieren photograph M221900B 45
Figure 55: Schlieren photograph M221960A 46
Figure 56: Schlieren photograph N221970B 46
Figure 57: Schlieren photograph P221980C 46
Figure 58: Schlieren photograph R222000C 47
Figure 59: Schlieren photograph S222080A 47
Figure 60: Schlieren photograph T221980A 47
Figure 61: Schlieren photograph T221980B 48
Figure 62: Schlieren photograph V31750A 48
Figure 63: Schlieren photograph V181950A 48
Figure 64: Schlieren photograph V182250A 49
Figure 65: Contact shadowgraph photograph W22198E 49
Figure 66: Photograph V221960K (unprocessed) 50
Figure 67: Photograph V221960K (processed) 50
Figure 68: Photograph A221620B (unprocessed) 50
Figure 69: Photograph A221620B (processed) 51
Figure 70: Photograph A181620A (unprocessed) 51
Figure 71: Photograph A181620A (processed) 51
Figure 72: Photograph A181620H (unprocessed) 52
Figure 73: Photograph A181620H (processed) 52
Figure 74: Photograph A31600A (unprocessed) 52
Figure 75: Photograph A31600A (processed) 53
Figure 76: Photograph A31620H (unprocessed) 53
Figure 77: Photograph A31620H (processed) 53
Figure 78: Photograph C221620A (unprocessed) 54
Figure 79: Photograph C221620A (processed) 54
Figure 80: Photograph C221620B (unprocessed) 54
Figure 81: Photograph C221620B (processed) 55
Figure 82: Photograph C221620C (unprocessed) 55
Figure 83: Photograph C221620C (processed) 55
Figure 84: Photograph C221620D (unprocessed) 56
Figure 85: Photograph C221620D (processed) 56
Figure 86: Photograph C221620E (unprocessed) 56
Figure 87: Photograph C221620E (processed) 57

Figure 88: Microsoft® Paint drawing for shock wave measurements for three frame image. 58
Figure 89: Rough sketch of the measurements between five triple points 59
Figure 90: Detailed sketch of flow in a reference frame fixed in the first triple point 61
Figure 91: Mach number variations for burst pressure of 1.8 bar 65
Figure 92: Deflection angles variations for burst pressure of 1.8 bar 65
Figure 93: Mach number variations for burst pressure of 2.2 bar 67
Figure 94: Deflection angles variations for burst pressure of 2.2 bar 67
Figure 95: Mach number variations for burst pressure of 3 bar 69
Figure 96: Deflection angles variations for burst pressure of 3 bar 69
Figure 97: Mach number variations for all burst pressure 72
Figure 98: Mach number variations for burst pressure of 1.8 bar 72
Figure 99: Mach number variations for burst pressure of 2.2 bar 73
Figure 100: Mach number variations for burst pressure of 3 bar 73
Figure 101: Pressure traces for photograph V221960K 74
Figure 102: Pressure traces for photograph A221620B 75
Figure 103: Pressure traces for photograph A181620A 75
Figure 104: Pressure traces for photograph A181620H 76
Figure 105: Pressure traces for photograph A31600A 76
Figure 106: Pressure traces for photograph A31620H 77
Figure 107: Density contour for 10° ramp with intersection shown. 78
Figure 108: Density contour of 15° ramp with intersection shown. 79
Figure 109: Density contour of 20° ramp with intersection shown. 79
Figure 110: Triple point at the furthest dowstream bottom test section (flipped horizontally). 81
Figure 111: Modified schlieren photograph P221980C 83
Figure 112: Schematic drawing of photograph P221980C 84
Figure 113: Schlieren photograph N221970B with measurement 85
Figure 114: Original and processed image to highlight expansion waves of photograph O221970D (Skews et al., 2008) 86
Figure 115: Original and processed image to highlight shock waves of photograph L221900A (Skews et al., 2008) 86
Figure 116: Photograph V221960K (modified) 87
Figure 117: Average Mach Number Variations 90
Figure 118: Average deflection angles variations 91
Figure 119: Pressure ratio across the shock wave for test V221960K 93

List of Tables

Table 1: Different types of lenses and their approximated focal length 28
Table 2: Different types of diaphragm and their properties 31
Table 3: Oblique shock calculations for burst pressure of 1.8 bar 64
Table 4: Oblique shock calculations for burst pressure of 2.2 bar 66
Table 5: Oblique shock calculations for burst pressure of 3 bar 68
Table 6: Secondary oblique shock calculations 71
Table 7: Average for good results 90
Table 8: Average for secondary calculations 92

List of Symbols

a	Speed of sound
d	Distance
i	Incident shock wave
M	Mach number
m	Mach stem
R	Specific Rankine gas constant
r	Reflected shock wave
T	Temperature (in Kelvin)
t	Time
V	Flow velocity
α	Triple point trajectory angle
β	Angle between the incident and reflected shock waves
γ	Ratio of specific heats
θ	Deflection angle of flow between shock waves
ξ	Inverse pressure ratio of the incident shock wave

Subscripts

1	Region in front of the incident shock wave and the Mach stem
2	Region between the incident and reflected shock waves
3	Region behind the reflected shock wave

1 Introduction

Over the last 60 years or so, many researchers have extensively investigated shock wave reflection phenomena both theoretically and experimentally. Much of this was started by the distinguished philosopher Ernst Mach. He published the first known paper on the phenomenon of planar shock-wave reflections over straight wedges over 129 years ago in 1878 (Ben-Dor, 2006). He presented two types of shock reflections, namely the regular reflection (RR) and the Mach reflection (MR) that was named after him in the 1940s.

In 1943, a great mathematician, John von Neumann, published a paper on the oblique reflection of shock waves. He developed the theory for a compressible substance with an arbitrary equation of state (Sakurai et al., 1989). He considered both air and some water-like substances in his theory. He used the assumption that air is an ideal gas, and was able to deduce specific algebraic equations that solved the problems for both the regular reflection (RR) and Mach reflection (MR). This theory is known as the two shock theory for RR and three-shock theory for MR. These theories, however, agree with strong shock reflection experiments, but there are great discrepancies with the weak shock reflections. This was the beginning of the so called von Neumann paradox, which was named by Birkhoff in 1950. A type of irregular reflection was named after him as von Neumann Reflection (vNR), which is shown in figure 1 below:

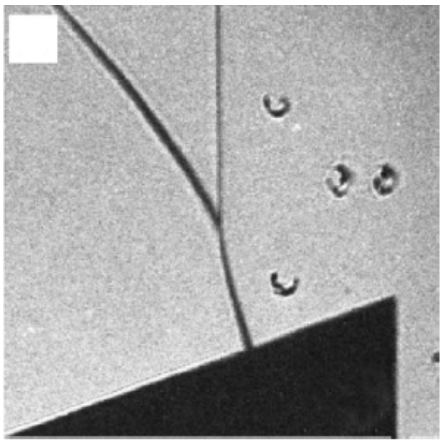


Figure 1: Schlieren photograph of a von Neumann reflection for weak shock (M_i = 1.10 and θ_w = 20°) (Kobayashi et al., 2004)

A regular reflection does not have a Mach stem, thus it only has an incident shock wave and a reflected shock wave. This means a regular reflection is a two wave pattern, where the trajectory of the intersection of the two waves is on the wedge surface. A Mach reflection has a Mach stem which extends from the wedge surface towards the intersection of the incident and reflected shock waves. This is a three wave pattern, and the intersection is known as the triple point. The von Neumann reflection is also a three wave pattern; the only difference is that the Mach stem merges smoothly into the incident shock wave, i.e. the shock wave slope from the incident and Mach stem shocks is continuous.

The von Neumann paradox is a major unsolved problem in supersonic gas dynamics (Kobayashi et al., 2004). Many researchers tried to resolve the problem both theoretically and experimentally. Many of them examined the assumptions relating to von Neumann's theory, such as the following:

- Real gas effects,
- Boundary layer effect,
- Boundary condition on the slipstream, and
- Non-uniformity of the flow field.

However, until recently there has been no definitive explanation for why von Neumann's theory accurately describes the strong shock reflection but a great discrepancy occurs when the theory is applied to weak shock reflection. This may be because the von Neumann paradox is not only caused by one specific factor above. There may even be more factors such as described below.

In 1947, a German scientist G. Guderley was the first to suggest a theoretically consistent solution instead of the non-physical branch in the von Neumann theory (Vasilev et al., 2007). His theory uses approximation of potential (isentropic) flow for weak shock waves. He concluded the existence of a supersonic patch behind the triple point. He also suggested a four-wave theory, which was later proven by Vasilev et al. (1999) with his high resolution numerical scheme and a new front-tracking technique. However, the isentropic solution could not eliminate the contradiction in the von Neumann's theory since it did not include a tangential discontinuity. This type of irregular reflection was named as Guderley reflection (GR) by Skews (2006) and is shown below:

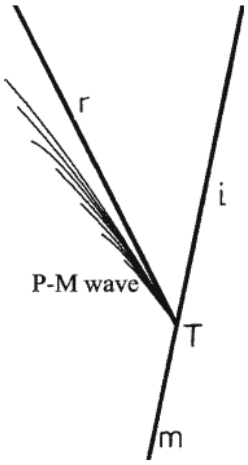


Figure 2: Schematic diagram of a Guderley reflection (GR) (Skews, 2006)

The Guderley reflection has similar features to the von Neumann reflection. The difference is that the Guderley reflection is a four wave pattern, which means there is another wave behind the reflected shock wave also intersecting the triple point. It should be noted that the intersection point must no longer be called a triple point; rather a four-wave intersection point would be more precise.

In 1949, experiments conducted by Bleakney showed large discrepancies for weak shock reflection when using the von Neumann's three-shock theory (Sakurai et al., 1989). In 1956, Jahn obtained interferograms that showed a subsonic compression which follows the reflected wave (Skews, 1971). Sakurai (1964) suggested the divergence of the slipstream may be one of the possible causes of the von Neumann paradox (Kobayashi et al., 1995). Then in 1971, Skews was the earliest to examine the effect of the slipstream divergence and the pressure difference on both sides of the slipstream.

In 1987, Ben-Dor proved that the von Neumann's theory agrees well with his experiments for strong shock wave ($M_i > 1.46$) (Kobayashi et al., 1995). However, Colella and Henderson further proved that the von Neumann theory is invalid for weak shock reflections in 1990. In 1992, a revised three-shock theory by Olim and Dewey showed agreement of the experimental and theoretical results for weak shock reflection. Their theory assumed a linear relationship between the pressure behind the reflected shock and the triple point trajectory angle. However, this assumption has no physical meaning (Kobayashi et al., 1995).

In 1997, Sandeman used both the three-shock and four-shock theory in his simulations for weak shock reflections. He suggested these two theories are not suitable for weak shock reflection mainly due to the low resolution of his simulations. In 1999, Vasilev and Kraiko

showed Guderley's four-wave theory with their high resolution simulations. They also proved that the flow behind the reflected shock is subsonic and small supersonic patches formed behind the triple point, and expansion fans exist. They were able to use the four-wave theory to completely resolve the von Neumann Paradox numerically (Vasilev et al., 2007).

Hunter and Brio (2000), using the unsteady transonic small-disturbance equations, further proved the existence of the supersonic region behind the triple point. They suggested this supersonic region is very small at about 0.05 – 1% of the size of the Mach stem. Their numerical solution has essentially the same structure as the one proposed by Guderley (1962) for weak shock reflection in steady transonic flows. Figure 3 below illustrates their solution, the dotted-dashed line is a sonic line, and the dotted lines are minus characteristics while the dashed lines are plus characteristics:

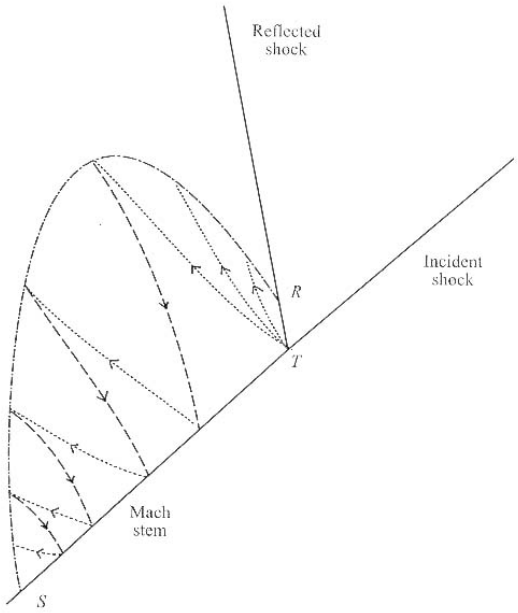


Figure 3: Schematic diagram of the structure of weak shock reflection (Hunter et al., 2000)

Also in 2000, Zakharian used the full Euler equations to prove that a supersonic region and expansion fans exist near the triple point. This region is about 0.5% of the size of the Mach stem. Figure 4 below shows the size of the supersonic region in dotted lines:

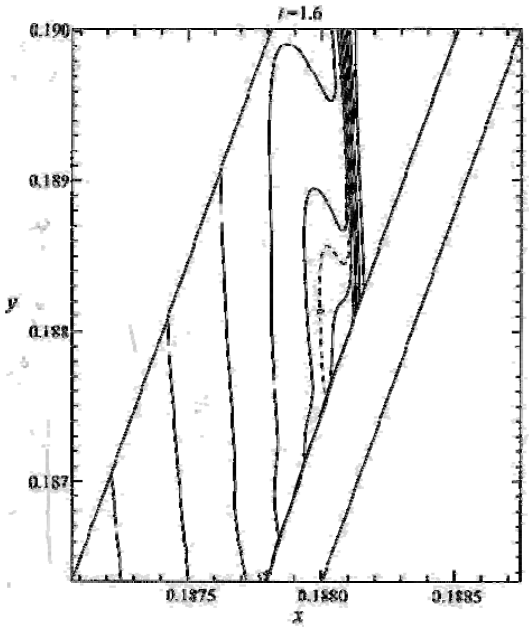


Figure 4: The size of the supersonic region (Zakharian et al., 2000)

In 2002, Hunter and Tesdall, with higher resolution simulations, showed a sequence of supersonic patches, triple points and expansion fans formed by the reflected shock and compression waves between the sonic line and the Mach stem. This also implies that, for an inviscid flow, an infinite number of triple points form for a weak shock wave reflection. The following figure shows their findings:

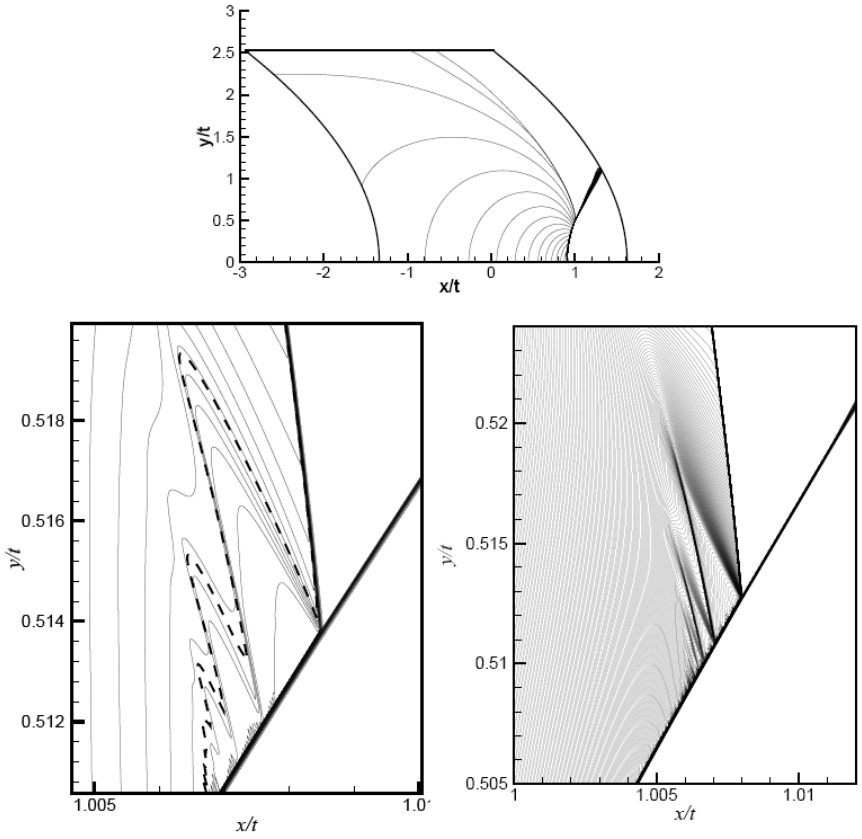


Figure 5: The structure near the triple point with a sequence of shocks, expansion fans, triple point and supersonic patches behind the reflection wave. The dashed line is the sonic line. (Hunter et al., 2002)

Until now, the von Neumann paradox had been extensively studied using theoretical simulations conducted by the above researchers. However, not much emphasis was placed on experimental findings using conventional shock tubes since they could not resolve a more complex flow at the triple point, presumably due to the very small size of this triple point region. The physical existence of these complex flows thus remained in question, particularly since all the simulations were for inviscid flows. In 2006, Skews and Ashworth finally put the von Neumann paradox to rest by their unique experiments with a large shock tube (9.5m long, 1.1m high and 0.1m wide). They discovered a sequence of shocklets and compression waves near the triple point from their shadowgraph photographs. However, due to the poor quality of the photographs, the conclusion based on these post-processed photographs seems doubtful (Vasilev et al., 2007). Therefore, further investigation with high quality photography is necessary to prove the existence of shocklets and compression waves near the triple point.

At the recent International Symposium on Shock Waves in Germany, Vasilev presented data indicating a new type of Mach reflection provisionally known as the ?R (Vasilev et al., 2007).

This new type of reflection is closely related to the Guderley reflection (GR). The only difference being that the supersonic patch behind the reflected shock is terminated at the slipstream of the triple point. It was also concluded the vNR (von Neumann reflection) concept by Colella in 1989 as a resolution of the von Neumann paradox is not correct. The following picture shows the difference between vNR, GR and ?R:

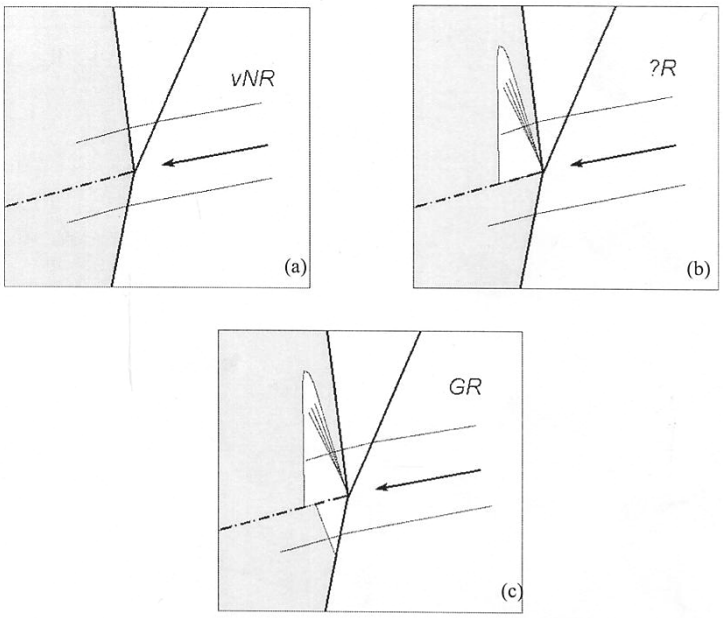


Figure 6: Schematic illustration of the three types of reflection: vNR, ?R and GR. Light gray regions are subsonic. (Vasilev et al., 2007)

This work seeks to detail more in-depth analysis of weak shock reflection, as well as improve the understanding of the von Neumann paradox through some experimental schlieren photographs taken in the laboratory.

2 Background and Motivation

2.1 Types of Shock Wave Reflections

Over the years, many researchers have discovered many different types of shock wave reflections. The best wave configurations known to the author were developed by Ben-Dor (2006). The following figure shows the evolution-tree type presentation of the various types of shock wave reflections:

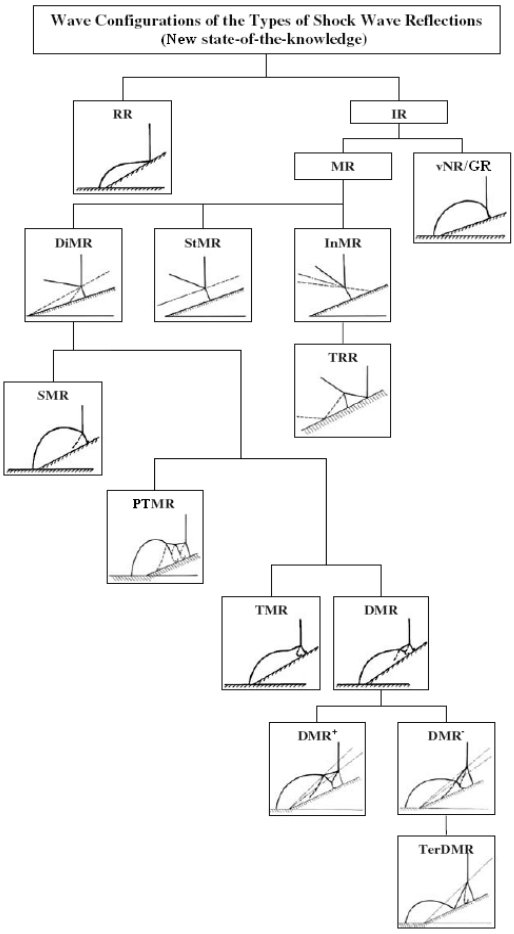


Figure 7: Modified evolution-tree type presentation of the wave configurations of various types of shock wave reflection (Ben-Dor, 2006)

The abbreviations in figure 1 are as follows:

- Regular reflection – RR
- Irregular reflection – IR
- Mach reflection – MR
- von Neumann reflection – vNR
- Guderley reflection – GR
- Direct-Mach reflection – DiMR
- Stationary-Mach reflection – StMR
- Inverse-Mach reflection – InMR
- Transitioned regular reflection – TRR
- Single-Mach reflection – SMR
- Pseudo-transitional-Mach reflection – PTMR
- Transitional-Mach reflection – TMR
- Double-Mach reflection – DMR
- Positive double-Mach reflection – DMR^{+}
- Negative double-Mach reflection – DMR^{-}
- Terminal double-Mach reflection – TerDMR

The type of reflection that will be investigated within the report is the well known von Neumann reflection (vNR). The von Neumann reflection is one of the irregular reflections (IR). Unlike the sharp change in orientation of the Mach stem with respect to the incident shock wave at the intersection point (also known as the triple point) of a Mach reflection, the von Neumann reflection has a Mach stem that merges smoothly into the incident shock shown in figure 8 and 9 below.

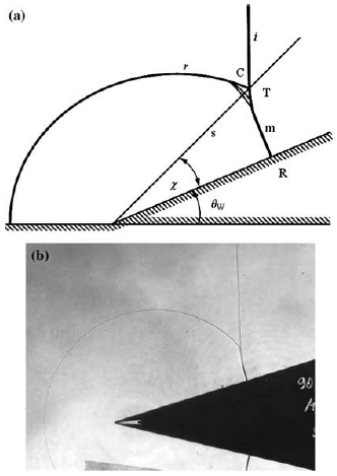


Figure 8: von Neumann reflection, (a) schematic illustration, (b) schlieren photograph. (Ben-Dor, 2006)

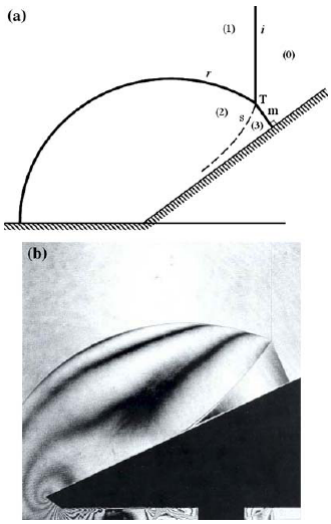


Figure 9: Single Mach reflection, (a) schematic illustration (b) interferometric photograph. (Ben-Dor, 2006)

The lines in the triple point region in the schematic diagram of the von Neumann reflection are a combination of compression waves forming the reflected wave. This is the model proposed by Colella and Henderson (1989) to resolve the paradox, and was the generally accepted model until the recent proof of the existence of Guderley reflection. This will be discussed further later.

2.2 The von Neumann Paradox

The first systematic study of the reflection of shock waves at rigid surfaces was carried out by von Neumann in 1943 (Sakurai et al., 1989). von Neumann developed a theory for a compressible substance with an arbitrary equation of state that was mainly focused on perfect gas (air in this case). He was able to deduce specific algebraic equations to solve the problem for regular reflection (RR) and Mach reflection (MR) with the assumption of air being a perfect gas. This results in the failure of the equation when the situation is a weak shock reflection (Mach no. less than 1.46) with other assumptions as well. However, the theory does produce satisfactory results as compared to strong shock wave reflection (Mach no. greater than 1.46) (Ben-Dor, 1987). Some of these experiments were conducted by Bleakney (1949) and Henderson et al. (1980). Some of their results showing the discrepancies between experimental data and von Neumann's theory are shown below:

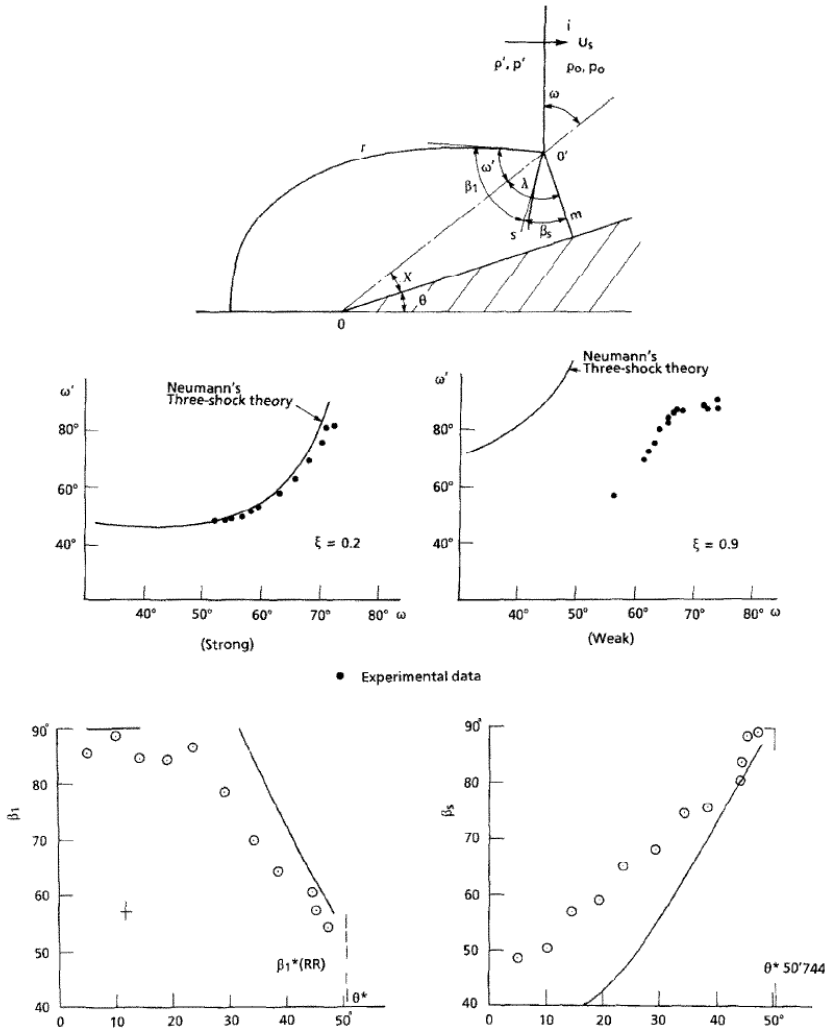


Figure 10: (top) Incident shock wave, i, passing over a concave corner; (middle) Display of "von Neumann paradox": comparison of von Neumann's three-shock theory with experimental data (Bleakney, 1949) for strong (ξ = 0.2) and weak (ξ = 0.9) cases; (bottom) Comparison of the shock wave angles (β_s, β_1 given by the von Neumann theory with their experimental data at the triple point. (Sakurai et al., 1989)

Possible reasons for the failure of the von Neumann theory for weak shock reflection could include the effects of viscosity, unsteadiness, nonlinearity and non-uniformities in the flow. However, experimental results shown by Bleakney and Henderson proved that viscosity is not the dominant factor. Viscosity is only dominant when the flow is near the corner (Walenta, 1983). This conclusion is also supported by a transformation of the Navier-Stokes equations as given by Sakurai (1985).

One of the assumptions of the von Neumann theory is that the flow is pseudo-stationary. This assumption is not often mentioned (Sakurai et al., 1989). In the experiment of the incident

shock over the concave corner, the weak Mach reflections are unsteady. However, if there is a uniform region of flow near the triple point, in the case of a strong Mach reflection, the local flow can be reduced to the stationary state by an elementary Galilean transformation along the trajectory of the triple point. This implies that the theoretical and experimental results would agree with each other. For the weak shock reflection case, however, the reflected and Mach waves are both curved. Thus the flow in the triple point region cannot be uniform. This implies that the von Neumann theory cannot strictly be applied to weak shock wave reflections. Furthermore, the fact that the flow behind the reflected shock is subsonic must also be taken into consideration.

Figure 11 shows an example of a reflection of a weak shock with an initial incident Mach no. of 1.41 and an angle between the incident shock and the triple point trajectory of 58.3° (Kobayashi et al., 1995). The shock polar illustrated in figure 11 shows no intersection between the I-polar and the R-polar, whereas the experiment shows that the Mach reflection is possible. This also implies the von Neumann theory is inadequate to describe weak shock reflection. Furthermore, the shock has a finite thickness, thus the triple point is not a mathematical point, but occupies a finite volume of space. This follows the fact that the slipstream is no longer a mathematical surface, which was assumed in the von Neumann theory.

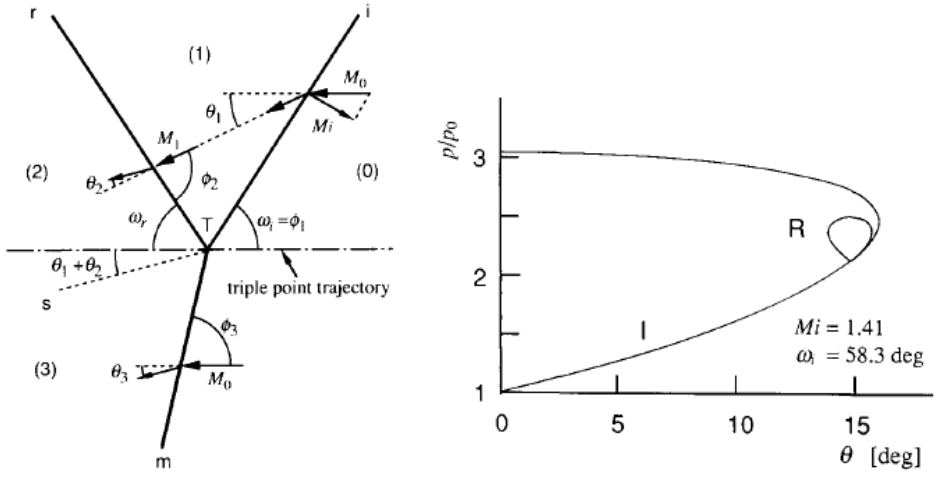


Figure 11: Triple point reference frame and the shock polar (Kobayashi et al., 1995)

2.3 Oblique Shock Theory

The following section has been adapted from Skews (2001). An oblique shock wave occurs when a supersonic compressible flow is turned into itself by a rigid corner. Since the flow is supersonic, there is no indication of the presence of the corner to the upstream flow. This causes the flow to change direction suddenly through the shock according to the angle of the corner. As a result, the static temperatures and pressures increase while the Mach number decreases. This can be illustrated by figures 12 and 13 below:

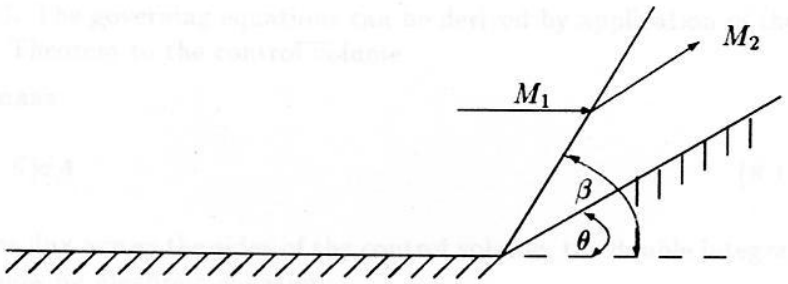


Figure 12: Supersonic flow over a concave corner (Skews, 2001)

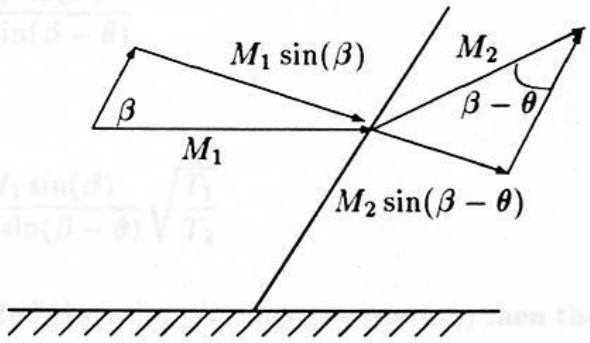


Figure 13: Transformation of an oblique shock into a normal shock (Skews, 2001)

The relationships between the pressures and Mach numbers across an oblique shock can be determined by the conservation of mass, conservation of linear momentum, conservation of energy and continuity equations (Skews, 2001). The final equations are shown below:

$$\frac{P_1}{P_2} = \left[\frac{1 + \gamma M_2^2 \sin^2(\beta - \theta)}{1 + \gamma M_1^2 \sin^2(\beta)} \right] \quad \textbf{1}$$

$$M_2 \sin(\beta - \theta) = \left[\frac{\left(\frac{2}{\gamma - 1} \right) + M_1^2 \sin^2(\beta)}{\frac{2\gamma}{(\gamma - 1)} M_1^2 \sin^2(\beta) - 1} \right]^{\frac{1}{2}} \quad \textbf{2}$$

$$\tan(\theta) = 2\cot(\beta) \left[\frac{M_1^2 \sin^2(\beta) - 1}{M_1^2 (\gamma + \cos(2\beta)) + 2} \right] \quad \textbf{3}$$

2.4 Schlieren Optical System

The schlieren method depends upon the refraction of the narrowly defined edge (typically a knife edge) of a light beam by gradients in the refractive index of the gas through which the beam of light passes. This optical principle is generally credited to Toepler (1906) and was modified extensively by Schardin (1934). The name "schlieren" means "optical in-homogeneity" (Kodak, 1960). In a typical system, a knife with a very thin and straight edge is used to adjust the light beam so that refraction in one direction adds to the total illumination, and refraction in the other direction subtracts from it. An example of the basic schlieren system is shown below:

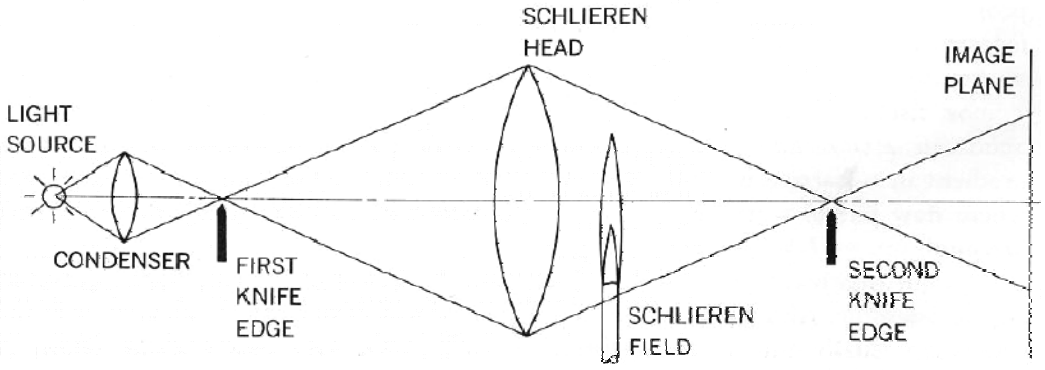


Figure 14: Basic schlieren system (Kodak, 1960)

A diverging light source is first focused into a point source by a condenser lens. The first knife edge is then placed at the focal point of the condenser lens, where the light becomes a smallest possible point (dependent on the filament of the light source). The functions of the first knife edge are as follows:

- To restrict the light beam so that the resultant beam has a sharply defined edge,
- To restrict the amount of light passing through the schlieren field (test section in most cases), and
- To increase the sensitivity of the schlieren optical system.

The light beam is then passed through the schlieren head, which focuses it through the schlieren field onto the second knife edge. By adjusting the position of this second knife edge (which is parallel to the first knife edge), it acts as a gate to intercept a large part of the luminous flux. The main function of the second knife edge is to vary the sensitivity of the picture on the image plane. However, as the sensitivity increases by cutting more light, the details of the picture decrease. It is suggested that the second knife edge should cut off around half of the light beam.

If there are no gradients in the refractive index within the schlieren field, the amount of light reaching the film is fixed by the amount of light being cut off by the two knife edges. However, if a gradient normal to the plane of the knife edges exists, the beam will be refracted so that it either makes the specific area of the image bright or dimmer. Thus, a schlieren field involving a pattern of densities is reproduced in various tones on the film. Here are some more examples of schlieren optical system:

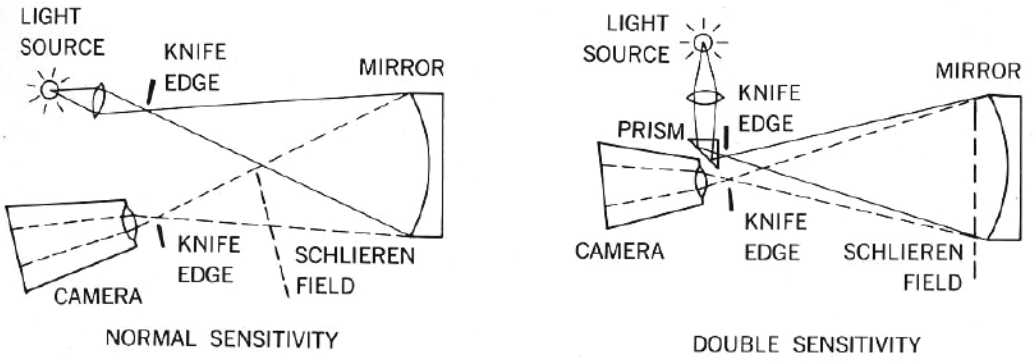


Figure 15: Different sensitivity single mirror schlieren system (Kodak, 1960)

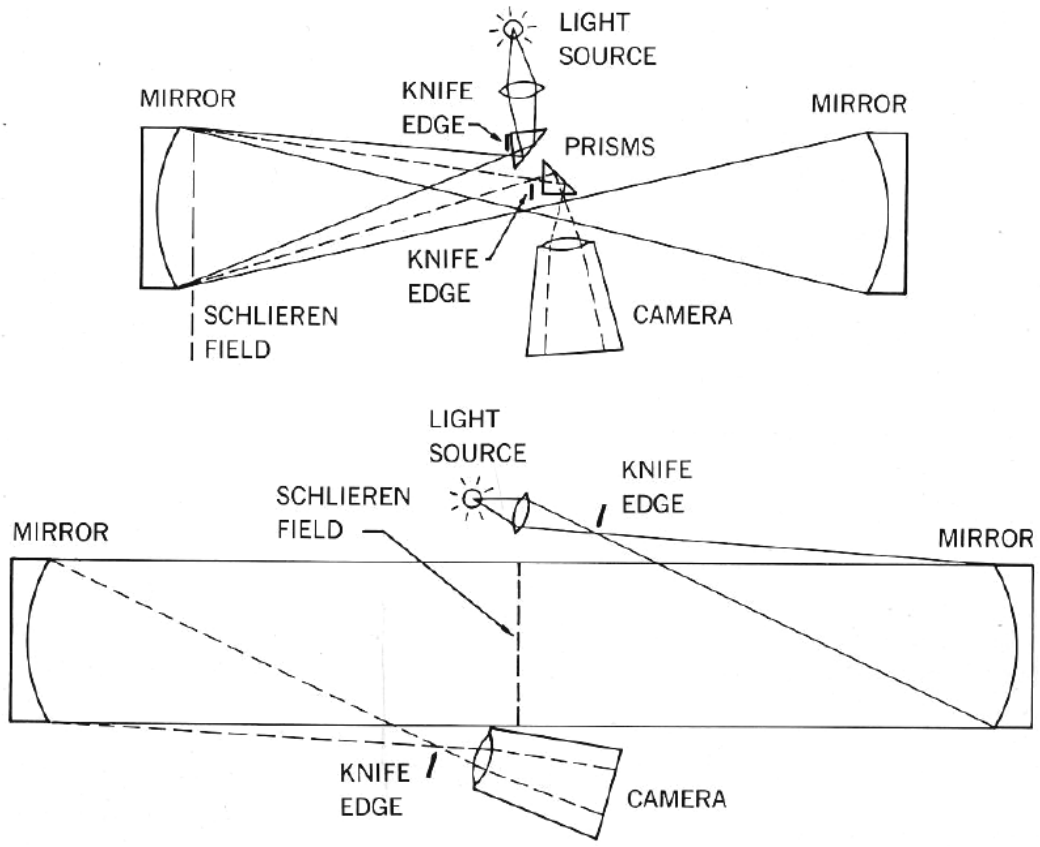


Figure 16: Different type of double mirror schlieren system (Kodak, 1960)

3 Objectives

The objectives of the project are to further understand irregular shock reflection by means of the following analysis:

- To obtain schlieren single-frame photographs for three different Mach numbers by using the large shock tube developed by Skews and Ashworth (the "Blue Shock Tube") in the Mechanical Engineering Laboratory, and to extend the experimental domain covered by them.

- To obtain schlieren photographs using the million-frame per second camera for three different Mach numbers, in order to obtain quantitative flow parameters.

- To calculate the different Mach numbers in the regions around the triple point by the use of oblique shock equations for the million-frame per second photographs.

- To obtain computational fluid dynamics (CFD) data for the modification of the ramp angles for the Blue Shock Tube.

- To design the ramp insert for the Blue Shock Tube.

4 Apparatus

4.1 The Blue Shock Tube

The blue shock tube is the largest shock tube within the Mechanical Engineering Laboratory. The overall dimensions of the shock tube are approximately 9.5m long, 1.1m high and 0.1m wide. It consists of five different parts as shown in figure 17, namely the compression chamber (A), the plunger section (B), the divergent section (C), the rectangular expansion chamber (D) and the rectangular test section (E). The two rectangular sections were originally built in the 1970's, and were abandoned due to diaphragm rupture problems because of the size of the shock tube. In 2005, Ashworth used the two rectangular sections with the addition of a new divergent section which enabled him to use the shock tube for his research. The shock tube's compression chamber was designed to withstand a pressure of 6 bar. However, most of the tests were done under 5 bar. The plunger section consists of a simple stainless steel needle, which is armed by a spring when compressed by a simple catch. A wire is connected to the catch. When the wire is pulled, it releases the catch, and the needle punctures the swollen diaphragm. This causes a shock to travel down the divergent section and a triple point is generated at the top of the divergent section due to the change of angle. The triple point then travels towards the test section, where the pictures are taken. Some illustrations of the Blue shock tube, including the schematic diagram, are shown in figure 17 to figure 21 below:

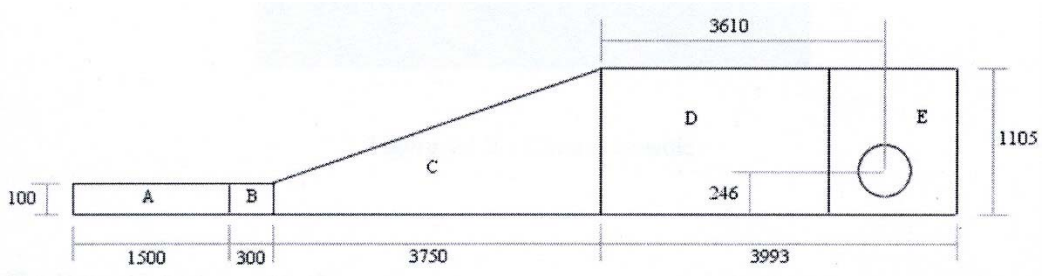


Figure 17: Schematic diagram of the blue shock tube with dimensions in mm (Skews et al., 2006)



Figure 18: The full size configuration of the blue shock tube (with castors)



Figure 19: Another view of the blue shock tube (without castors)

The design of the test section is unique due to the rotational mechanism that enables the two glass windows to rotate around to cover different sections within the test section. Also by rotating the entire rectangular section, it is also possible to cover the area upstream. Similarly, by removing the rectangular expansion chamber and replacing it with the test section, virtually anywhere after the divergent section can be covered by these two windows. This was the second configuration used by the author as shown below:



Figure 20: Another configuration of the blue shock tube



Figure 21: Another view of the second configuration of the blue shock tube

The shock tube originally rested on the floor on rectangular channels. It was decided to install castor wheels onto all sections to enable the mobility of the shock tube, thus allowing the configuration to be changed easily and quickly.

4.2 Control Panel

The control panel can be either mounted on the expansion chamber (with the full shock tube configuration) or on the test section (with the expansion chamber being left out) for convenience. The control panel is shown below:



Figure 22: The control panel

The control panel consists of the following:

- An inlet hose connects to a 6 bar air supply.
- A global-type '317' variable inlet valve to control the pressure to the system.
- An air filter used to filter any contaminants from the pressure line.
- A pressure gauge, with the maximum reading of 1000 kPa and a minimum of 20 kPa, that indicates the pressure within the compression chamber.
- A ball control valve, to control air into the pressure gauge.
- Another ball control valve, to vent the compression chamber after tests or in case of emergency.
- An outlet hose that connects to the compression chamber.
- A thermometer.
- The wire connected to the spring of the plunger.

4.3 Data Acquisition and Instrumentation

The data acquisition system consists of the following:

- Two PCB Piezotronics ICP® fast response high speed piezo-electric pressure transducers (Model 113A21). Serial number: 14052, calibration constant: 3.0423 mV/kPa (channel 1, upstream); Serial number: 14050, calibration constant: 3.2548 mV/kPa (channel 2, downstream).
- PCB Piezotronics ICP® sensor signal conditioner (Model 482A22) with four channels. Serial number: 1706
- Yokogawa DL1540 digital oscilloscope (Model 701510). Serial number: 25WY0367
- Centre for Instrumentation Research, Cape Technickon, Time delay unit with 50 to 99999 μs and 0 – 2.5V output.

A picture of the data acquisition setup is shown below:



Figure 23: Data Acquisition system, Yokogawa DL1540 digital oscilloscope (left) and Time Delay Unit (middle), Signal Conditioner (right).

When the shock wave triggers the pressure transducers, signals are sent directly to the signal conditioner for signal amplifications. The amplified signal is then sent to the digital oscilloscope. The output of the oscilloscope is then sent to the time delay unit. Then a 2.5V rising edge trigger signal will be sent to the light source to trigger a pulse of light after the set time delay, and at the same time, a voltage is also sent back to the oscilloscope to ensure the

light source has been triggered. The following schematics were taken from Skews et al. (2006) for the locations of the four pressure transducers, where only channel 1 and 2 were used:

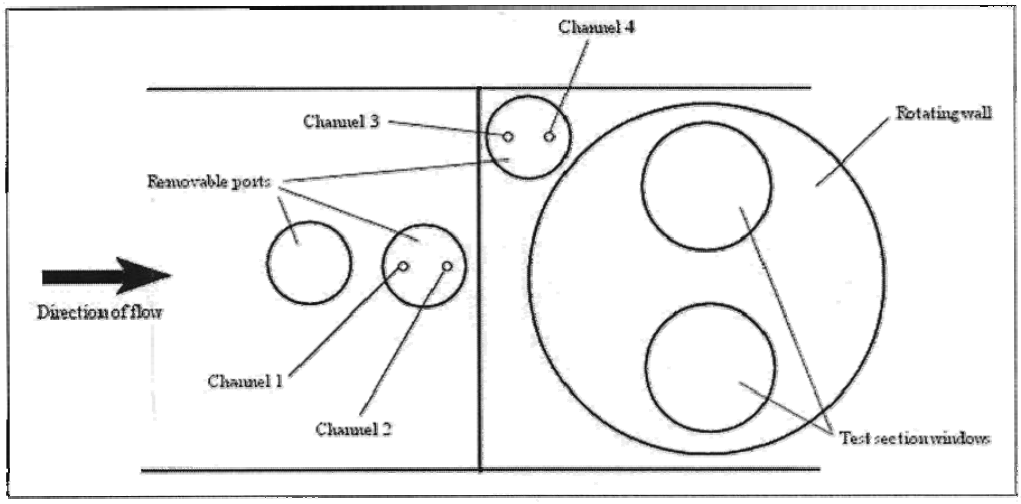


Figure 24: Configurations of the four pressure transducer on the shock tube (Skews et al., 2006)

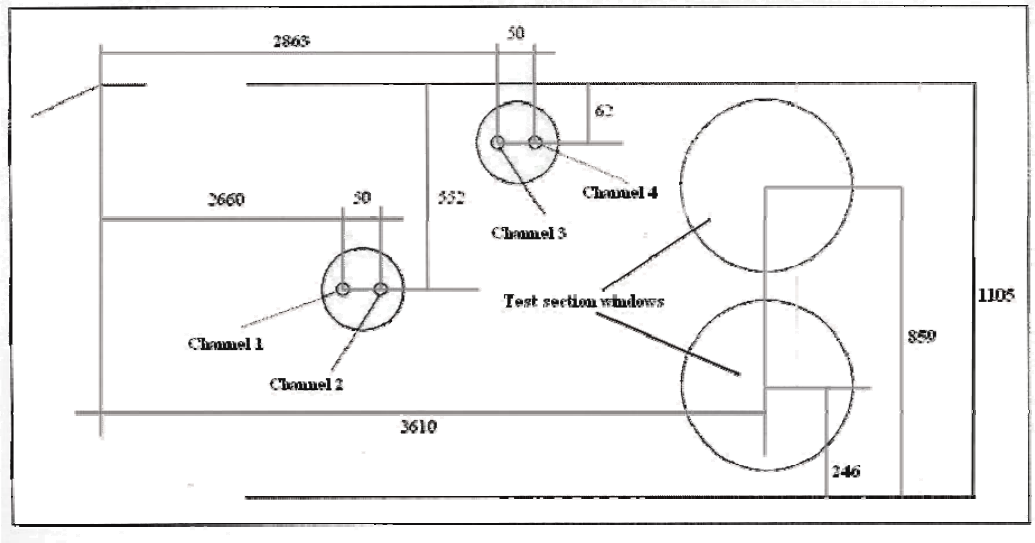


Figure 25: Positions of the four pressure transducers related to the test section in mm (Skews et al., 2006) (modified)

4.4 Optical System

4.4.1 Schlieren System

A simple two-mirror schlieren system was used for both the single-frame pictures and the multi-frame pictures. A schematic picture of the schlieren system is shown below:

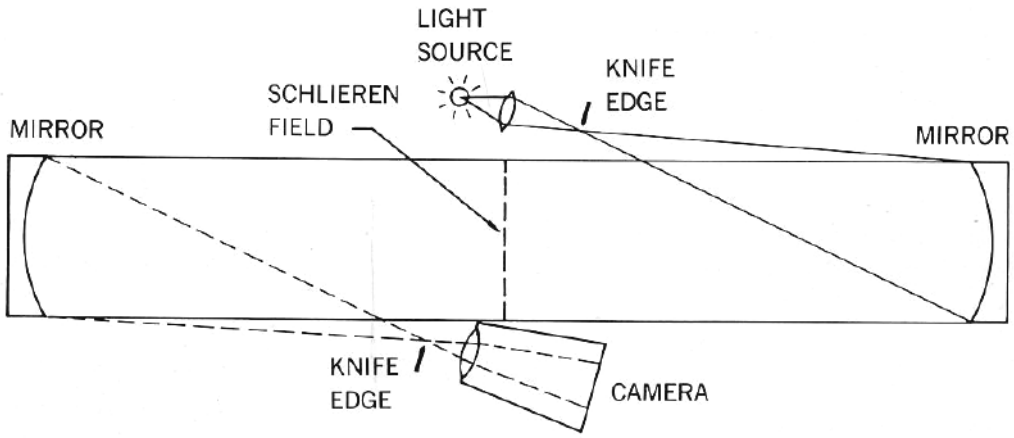


Figure 26: Two-mirror schlieren optical system used for single-frame and multi-frame photography (Kodak, 1960)

The system consists of a light source; either the xenon flash lamps or a continuous projector lamp were used depending on the image to be taken. The xenon flash lamps were used, with a Fujifilm FinePix S3 Pro SLR digital camera, for the single-frame photography. The continuous lamp was used, with a Cooke million-frame per second camera, for single-frame, multi-exposure photography. Two condenser lenses were used, one after the light source and the other before the camera. The lenses focussed the light either to the first knife edge as a point source or to the cameras as a smaller image to fit the camera's sensor. The first knife edge is a double sided knife edge made by two razor blades. This is to control the amount of light going into the optical system. It is positioned at the focal point of the first condenser lens and also at the focal point of the first parabolic mirror. The second knife edge is a single knife edge also made by a razor blade. This knife edge is used to control the sensitivity of the optical system. It is positioned at the focal point of the second parabolic mirror.

4.4.2 Contact Shadowgraph System

A shadowgraph system is very similar to schlieren system. The only difference is that there is no second knife edge in shadowgraph. In the case of a contact shadowgraph, the camera is positioned directly after the test section. Figure 27 shows a typical setup for a contact shadowgraph system:

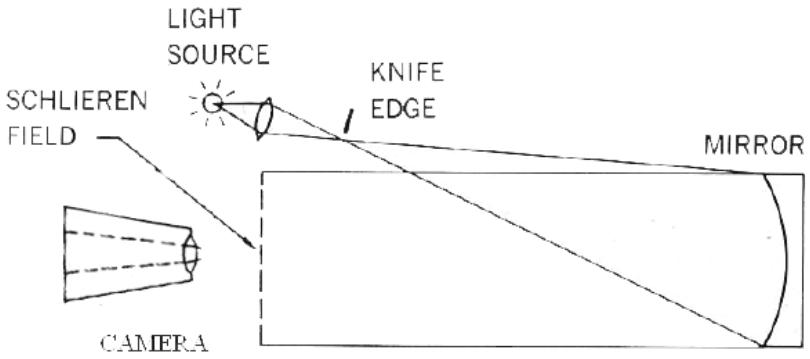


Figure 27: Typical contact shadowgraph setup (modified from Kodak, 1960)

4.4.3 Light Sources

There were two types of light sources used for the optical system. The first one was a xenon flash lamp and the second, a continuous projector lamp. Furthermore, two types of xenon flash lamps were used. They are both products of Hamamatsu Photonics made in Japan. The first one (model L2437), has a 15W input, 0.15 J per flash output and a short filament arc length of 1.5mm. The exposure time of each pulse of light is 1.9µs. Due to the light source not being bright enough when a high sensitivity schlieren system was used, a second light source was bought specifically for this purpose. The second light source (model L6604), has a 60W input, one J per flash output and a short filament arc length of 3mm. However, the exposure time of each pulse of light is 2.9µs. Although the new light source is much brighter than the old light source, the duration of the pulse makes the shock wave in the photograph appear 50% thicker. This makes the region of the triple point somewhat unclear when the camera is focused on the smaller region of the test section. The two light sources are shown below in figure 28 and figure 29:

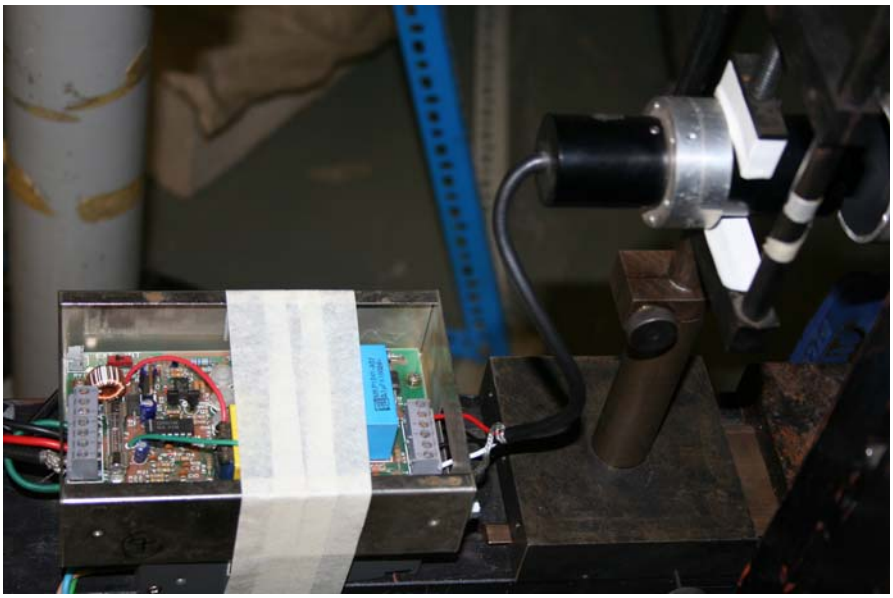


Figure 28: L2437 15 watts xenon flash lamp with power supply



Figure 29: L6604 60 watts xenon flash lamp with power supply and capacitor

The continuous light source was built by Mr. John Goulding from an old overhead projector. It consists of a power supply with variable voltage, a fan to keep the light bulb from overheating during operation, and a General Electric 650W Halogen light bulb. The light bulb generates an extremely bright white light, which is needed for the million-frame per second camera. A picture of this light source with its housing is shown in figure 30 below:



Figure 30: General Electric 650 watts continuous lamp in the housing and variable power supply

4.4.4 The Knife Edge

There are two knife edges used for the schlieren system. The first one, which is located at the light source station, is made of two razor blades. The distance between the two blades is adjustable to change the amount of light allowed into the system. Typically, the distance between them is less than 1mm. The orientation of the knife edges can also be rotated between horizontal, vertical or an inclined position (approximately 15 degrees to the vertical for the current tests). Although the angle is not very accurate, it is very close to parallel to the reflected shock angle. This ensures sensitivity of the schlieren optics to gradients in the direction normal to the reflected shock. The first knife edges are shown below:

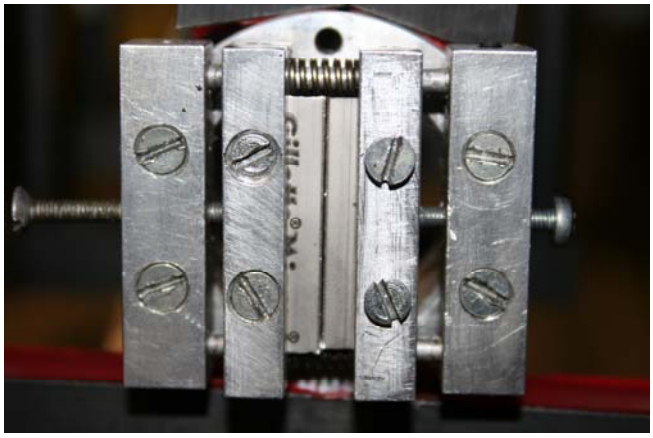


Figure 31: The first knife edge at the light source station

The second knife edge has only a single razor blade. This knife edge is mounted on a special stand different to the first knife edge and it is located at the camera station. This is because the second knife edge needs very precise adjustment, since it controls the sensitivity of the schlieren system. The stand is capable of linear movement along the three major axes: longitudinal (parallel to light beam), lateral (across the light beam) and vertical. These are controlled by screws. The knife edge can also change its orientation between horizontal and vertical. However, the second knife has to be parallel to the first knife edge. The second knife edge with the special stand is shown below:

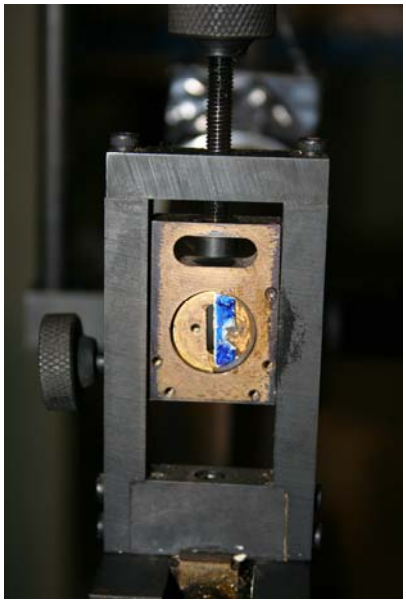


Figure 32: The second knife edge with its stand at the camera station

4.4.5 The Lenses

There are different types of lenses used for different configurations of the schlieren system. However, the specifications of these lenses were unknown to the author. Therefore the focal lengths of these lenses were determined approximately by the author. Table 1 lists the different type of lenses used and a picture of them is also shown below:

Table 1: Different types of lenses and their approximated focal length

Lens	Diameter (mm)	Focal Length (mm)	Thickness (mm)
1	43	60	9
2	51	60	11
3	50	140	10
4	65	220	12
5	77	340	5
6	77	600	16



Figure 33: Different types of lenses used

4.4.6 Parabolic Mirrors

There were two sets of parabolic mirrors used for the experiments. They are both high quality telescopic mirrors. The bigger set is 12.5 inch (312mm) in diameter, and the smaller set is 4 inch (100mm) in diameter. The focal length of the 12.5 inch is 1.90m and the 4 inch is approximately 0.93m. These are shown below:



Figure 34: 12.5 inch diameter parabolic mirror on its stand



Figure 35: 4 inch diameter parabolic mirror

4.4.7 Single-frame Camera

The single frame camera used for the schlieren photography was a Fujifilm FinePix S3 Pro SLR digital camera. It has a 12.34 million effective pixels Super CCD SR II sensor photo detectors. The size of the sensor is 23.0 by 15.5 mm. Its shutter speed can vary between 30 seconds to 1/4000 of a second, with the capability of bulb (manual shutter control). Its light sensitivity varies from ISO 100 to ISO 1600. These setting are analogous with the traditional film speed ISO number

4.4.8 Multiple-frame Camera System

The million-frame per second camera used was made by The Cooke Corporation. The camera has its own data acquisition system. This includes the following:

- The million-frame per second camera with its power supply.
- A computer with the suitable software to capture the pictures from the camera.
- A monitor that reads the real time photograph of the camera for adjustments.

Some of the specifications of the camera are listed below:

- Serial number: 335 CG 0073
- Time delay: 0 – 999 μs
- Exposure time: 0 – 999 μs
- Cycle: 0 – 9 times

4.5 Diaphragm

Different thicknesses of mylar sheeting were used as diaphragm material, in various combinations, to achieve different burst pressures. The diaphragms were inserted between the compression chamber and the plunger section. They were held normally by two rubber gaskets and vacuum grease. However, due to the high cost of vacuum grease and the large volume of experiments done, normal grease was used equally effectively. The diaphragms used are listed in the table below, which also specifies the corresponding natural burst pressure:

Table 2: Different types of diaphragm and their properties

Diaphragm Thickness (μm)	Maximum Natural Burst Pressure (KPa)
50	260
73	330
100	380
125	500

The diaphragm was found to work best within 50 kPa below the maximum natural burst pressure. Using burst pressures below this were found to cause non-uniform bursting of the diaphragm, resulting in non-uniform shock waves.

5 Experimental Procedure

5.1 Testing Procedure

The following step-by-step procedure was used for each test of the Blue Shock Tube:

1) Closed the exit of the shock tube.
2) Closed the supply valve to the control panel.
3) Opened main pressure line valve and inspected all pipes for leakage.
4) Tested the emergency vent (valve after the pressure gauge from the supply line) for any blockage.
5) Lights in the room are turned off to adjust the schlieren optical system.
6) Lights were then turned on after the schlieren system was setup or adjusted.
7) Logged ambient atmospheric pressure and temperature.
8) Inserted the correct combination of required diaphragm between the compression chamber and the plunger section.
9) Armed the burst needle using its spring
10) Closed the compression chamber, bolted it to the plunger section.
11) Turned off main lights and turn on the light bulb at the control panel.
12) The trigger system was set to the required time delay and armed.
13) Turned on the camera in standby mode.
14) Turned on light source electronics in readiness for external trigger.
15) Closed emergency vent on the control panel.
16) Inlet valve was opened slowly until the compression chamber was pressurised to halfway of the required pressure.
17) Sounded warning whistle.
18) Inlet valve was either maintained or opened further until the desired pressure.
19) Once the desired pressure was reached, the inlet valve was adjusted to maintain the pressure.
20) Turned off light bulb.
21) Camera shutter was then opened (single-frame case)

22) The wire connected to the spring was then pulled to fire the shock tube.
23) Closed the camera shutter once the shock wave had passed through the test section (single-frame).
24) The inlet valve was fully closed, and the emergency valve was opened.
25) The lights in the room were turned on.
26) The data in the oscilloscope was saved onto a floppy disc.
27) In the case of the multi-frame, the image on the million frame camera's screen was saved into the computer.
28) Turned off light source.
29) Cleaned the inside of the shock tube by high pressure air.
30) The compression chamber was then opened, and new diaphragm was ready to be loaded.
31) Repeated step 5 to 31 for each test.
32) Closed all valves and turned off all power supplies when experiments were finished.

5.2 Precautions

The following precautions must be kept in mind during the operation of the Blue Shock tube:

- All the data acquisition systems are switched on at least five minutes before the first test to allow sufficient time for them to settle to equilibrium state.
- Inspect the inside of the shock tube for any foreign objects.
- Do not stand close to the exit of the shock tube during operation.
- Hearing protection must be used by everyone within the laboratory during a test.
- A whistle must be blown to alert people around the laboratory, and sufficient time must be given between the warning and firing the shock tube to allow people to block their ears.
- Extra care must be taken while cleaning the glass windows, the parabolic mirror and the lenses. Use special cleaning equipment only.
- Never leave the compression chamber closed when not working in the laboratory.
- Never leave the main pressure supply valve open when not operating with the shock tube.
- Always vent the compression chamber after every test to avoid pressure build up.
- Always disarm the spring in the plunger section while inserting diaphragm.
- Ensure doors to the laboratory are closed, but must not be locked, during a test.

- Do not leave the camera shutter open for too long to avoid dust getting into the sensor. Always put the lens cap on when not operating with the shock tube.
- Check periodically that the bolts between each section of the shock tube, and those supporting it, are tightened once in a while.
- Make sure the test section windows are not free to rotate with the rotational mechanism.
- Check periodically all pipes for leakage.
- Never leave light source on for too long to prevent overheating of the power supply.

6 Results

6.1 Computational Investigation

Computational fluid dynamics (CFD) simulations were done to investigate the optimal insert angle to change the existing divergent section ramp angle. These simulations were computed using an in-house Euler solver developed in 1995 by a MSc student, Dr Luke Felthun, and the program is commonly referred to as "Luke's Code". This code runs in the C++ environment and it is capable of giving accurate results in a much shorter time for shock wave analysis as compared to the well-known Fluent™. Initially, a series of low resolution simulations were computed using ramp angles ranging from 8 degrees to 25 degrees. The conditions of the simulations are as follows:

- Initial Mach number: 1.32
- Estimated Mach number at test section: ~ 1.10
- Burst pressure: 220 kPa
- Atmospheric pressure: 83 kPa

Three angles were chosen for further analysis, namely the existing 15 degrees, and the proposed 10 degrees and 20 degrees. Three sets of results from these refined simulations, each at the time where the triple point is closest to the furthest downstream window position possible (with X and Y in meters), are shown in figure 36 to 47 below (indicated as two circles):

Due to the large variation in wave strength between the incident wave and reflected wave and with the computer resources available, the reflected wave cannot be accurately resolved, since it is nearly sonic. However, a reasonable indication is obtained for the position of the triple point.

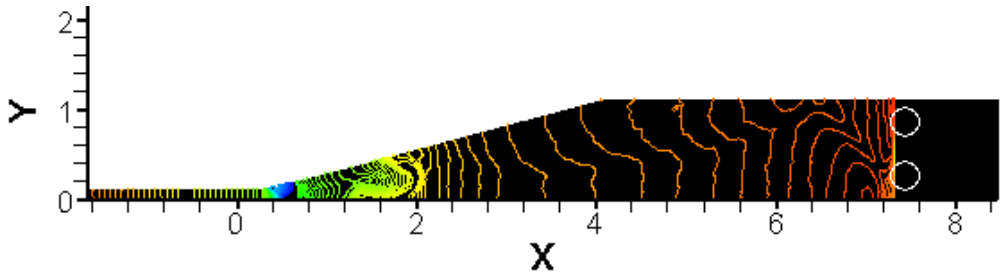


Figure 36: Density contours for 15° ramp angle as the triple point enters test section.

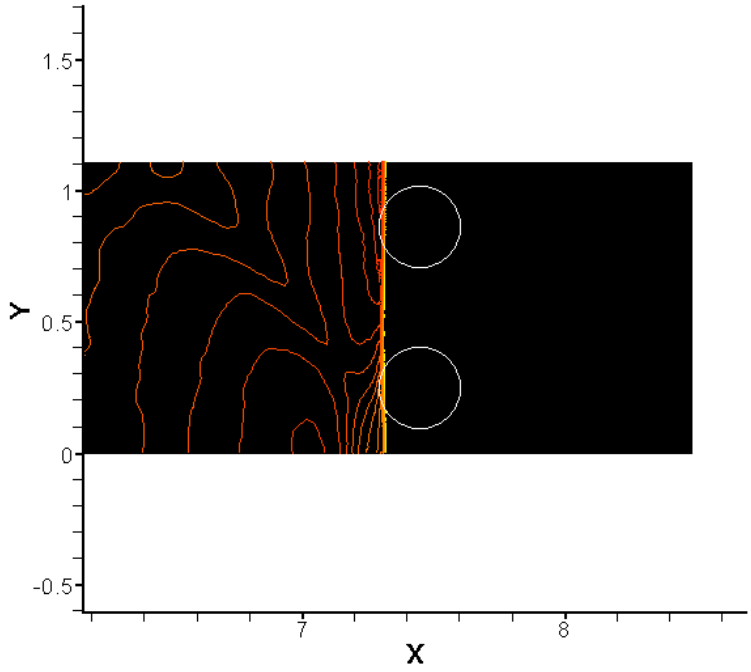


Figure 37: Shock wave entering the test sections for the 15° ramp.

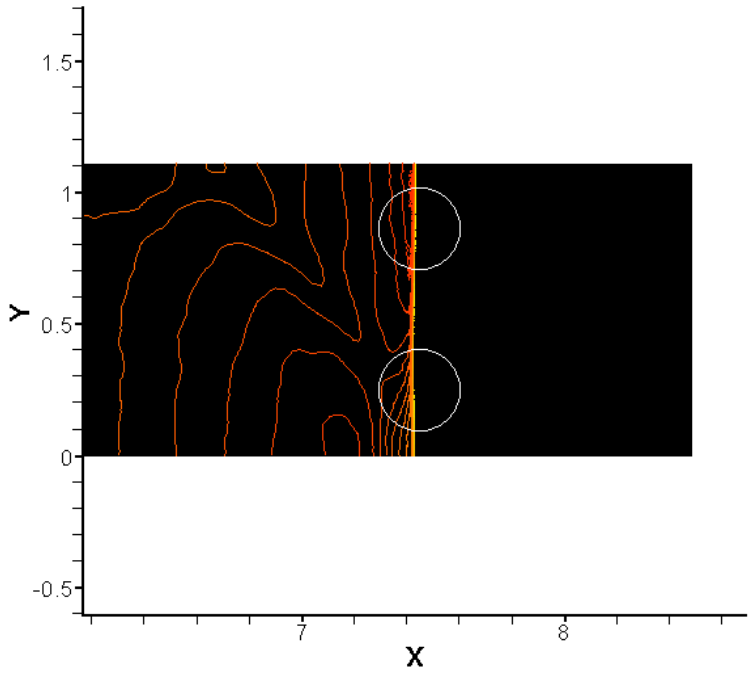


Figure 38: Shock wave at the centre of the test sections for the 15° ramp.

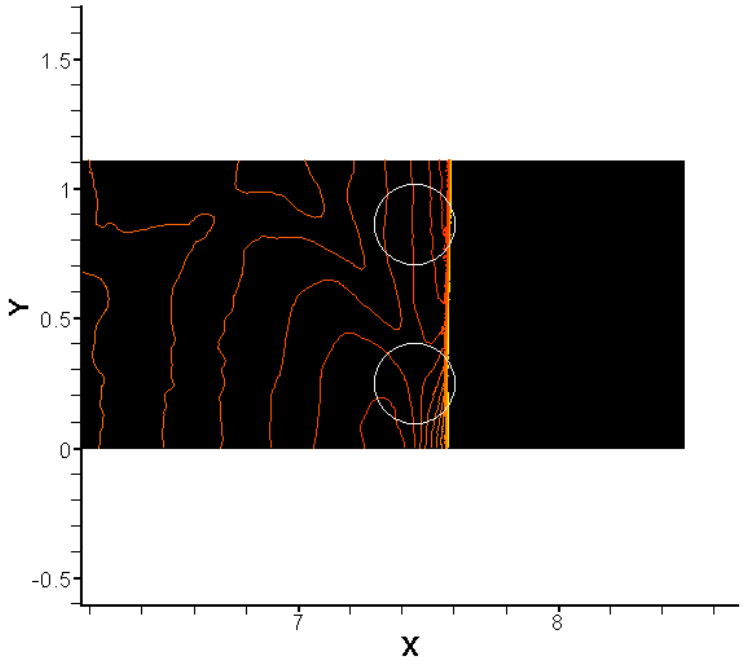


Figure 39: Shock wave leaving the test section for the 15 degree ramp.

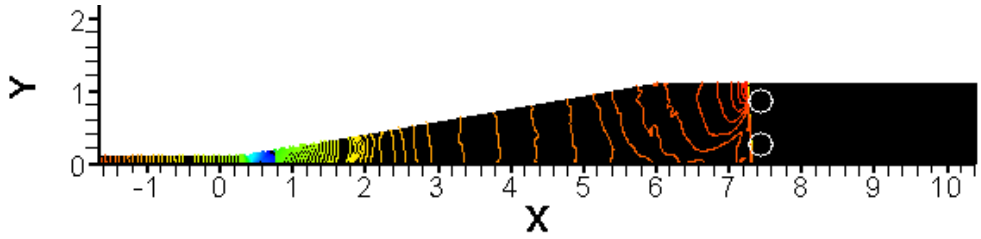


Figure 40: Density contours for 10° ramp angle as the triple point enters test section.

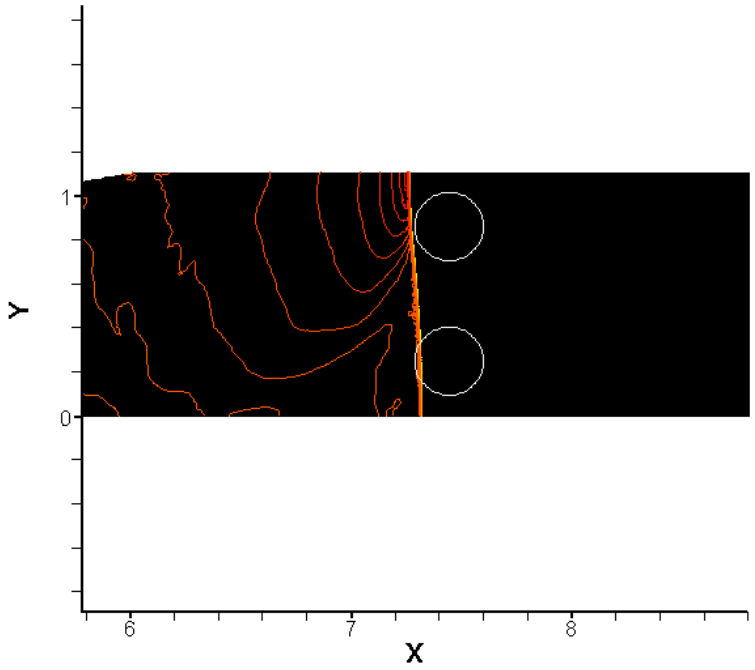


Figure 41: Shock wave entering the test section for the 10° ramp.

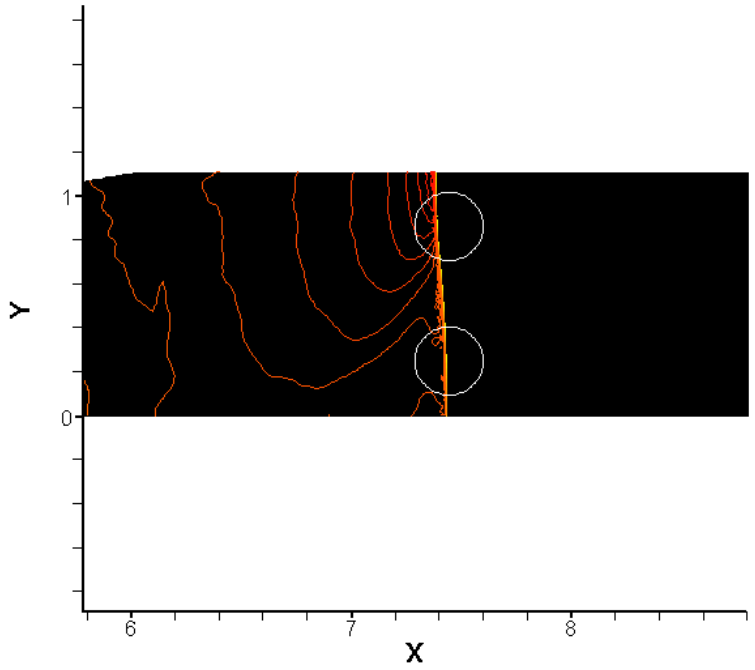


Figure 42: Shock wave at the centre of the test section for the 10° ramp.

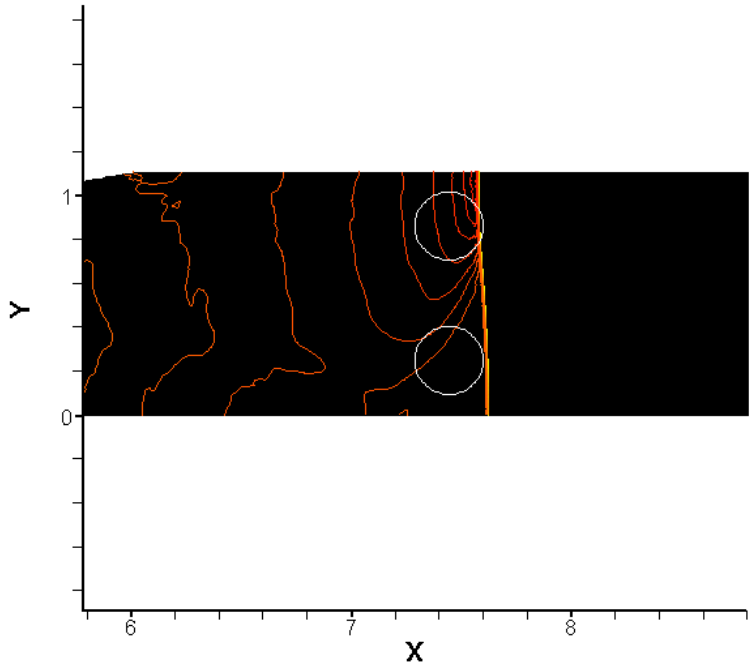


Figure 43: Shock wave leaving the test section for the 10° ramp.

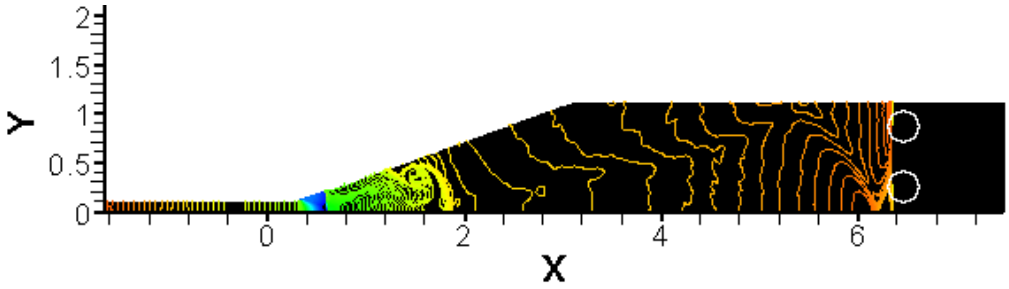


Figure 44: Density Contours for 20° ramp angle as triple point enters test section.

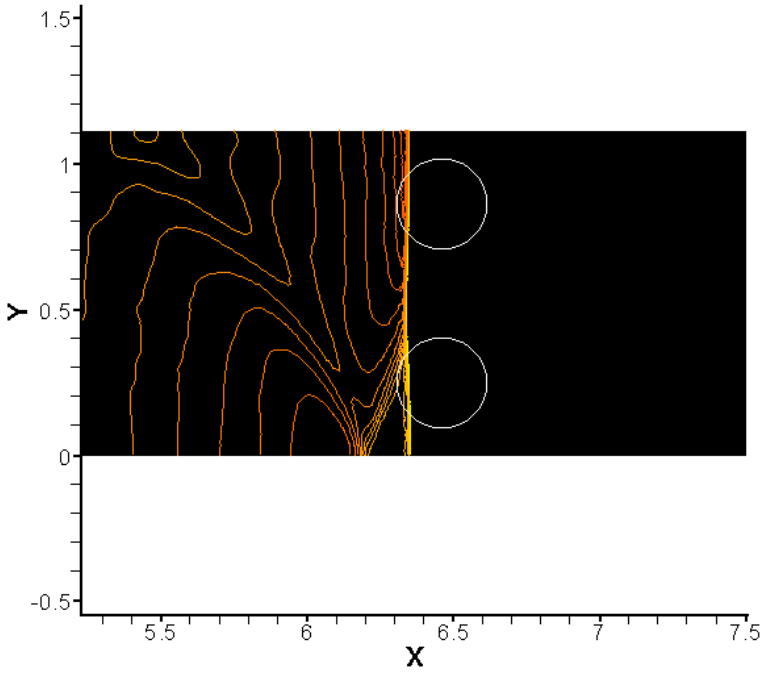


Figure 45: Shock wave entering the test section for the 20° ramp.

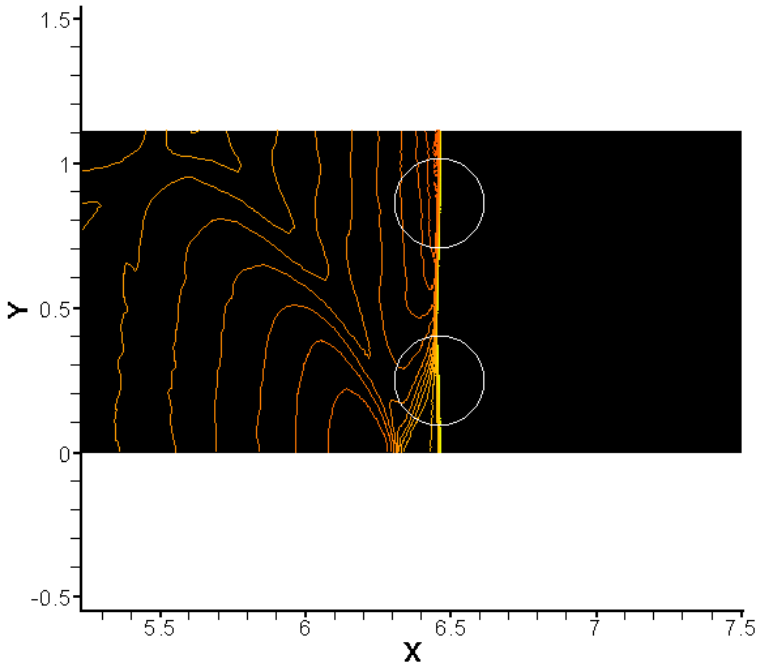


Figure 46: Shock wave at the centre of the test section of the 20° ramp.

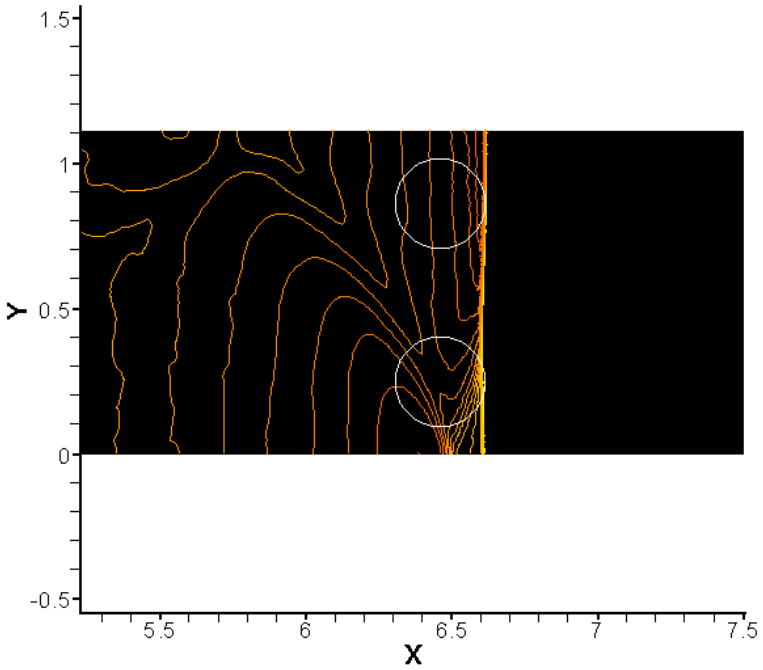


Figure 47: Shock wave leaving the test section of the 20° ramp.

The furthest possible downstream position of the test section was selected because if the triple point appears in the test section and has not bounced off the floor of the shock tube before that, it would be possible to visualise the triple point anywhere within the shock tube using the current apparatus. However, it would be ideal for the triple point to be fully developed at this point, the reason for which will be discussed further at a later stage.

The CFD results shows that the 20° ramp angle will generate a triple point that travel faster towards the floor of the shock tube then the other two angles. This means the test section has to be moved upstream. This leaves the triple point to not have enough time to fully develop before bouncing off the floor of the shock tube.

The 10° ramp angle will generate a triple point that is most developed as compared to the other ramp angles due to the slower speed towards the floor of the shock tube. However, the shock tube will need another two meter extension to move the test section downstream for capturing the best developed triple point. This will not be feasible due to the time constraint.

The 15° ramp angle was shown to be the optimal for the current shock tube configuration. However, the 10° and 20° ramp angles will be designed and built for further investigation.

6.2 Experimental Results

6.2.1 Single-frame Photographs

Over 400 single-frame photographs were taken at different shock tube configurations and different Mach numbers, some of which were not recorded in the log book as primary tests. It is impractical to present all of the photographs in this section of the report. Only the most informative images will be presented here. However, the remainder can be found on the DVD attached to this report as Appendix E. The overall illumination of the images varied considerably over the testing as adjustments were continually being made to the knife edges in an attempt to find the best balance of sensitivity and visibility. As will be shown the reflected wave is very weak so imaging it is demanding. Beside the small size of the supersonic patch, this has probably also contributed to these features not been identified before. The 15 watt xenon light source was used for test sets A to P and W, while set Q to V were obtained by the 60 watt xenon light source. The files were named using the following format:

For example: V182050C

- "V": indicates the test set number, i.e. set number V for this case. A total of 23 sets yielding codes "A" to "W" were conducted.
- "18": indicates the pressure in the compression chamber when the shock tube was fired, e.g. "18" means 1.8 bar.
- "2050": indicates for the time delay used (in μs), from channel 1, for the photograph taken.
- "C": indicates the number of this photograph with the same test conditions, i.e. "C" stands for the third photograph within this set.

Vertical and horizontal guides (produced by fixing thin strings across the test section windows) were used as calibration grids which are visible in the images. The purpose of these calibration grids was to focus the camera to the centre of the shock tube. This is done by attaching at least one string on each side of the windows. Then the position of the camera and lenses were adjusted to optimize the sharpness of all strings.

The unprocessed photographs are presented in figures 48 to 65 below:

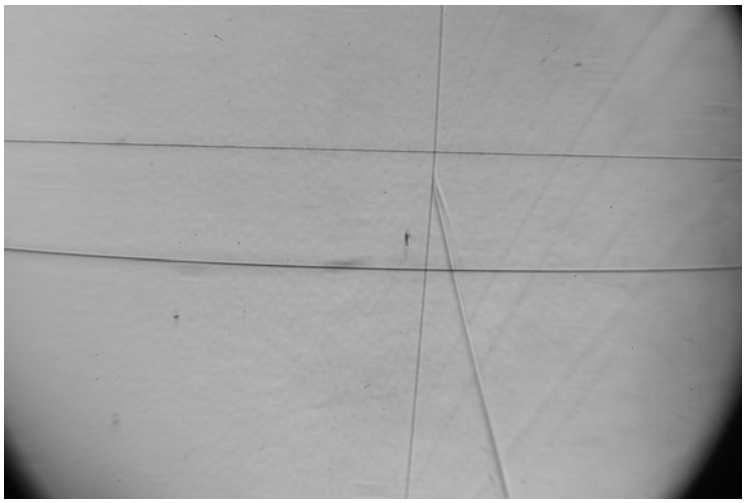


Figure 48: Schlieren photograph B221825A

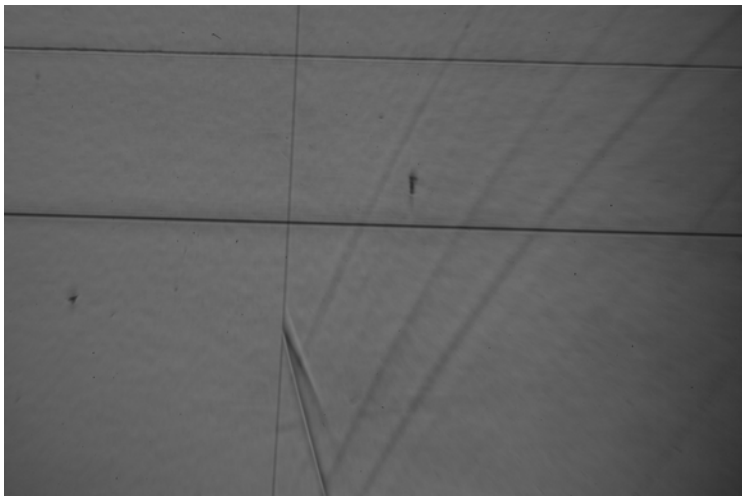


Figure 49: Schlieren photograph B221900B

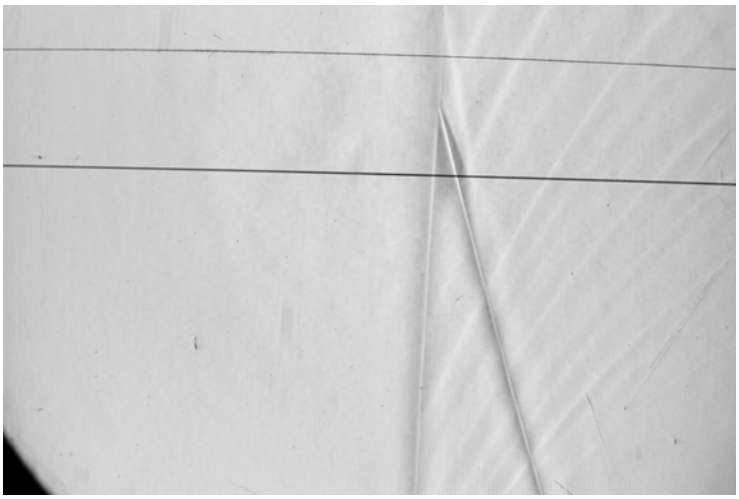


Figure 50: Schlieren photograph F221900B

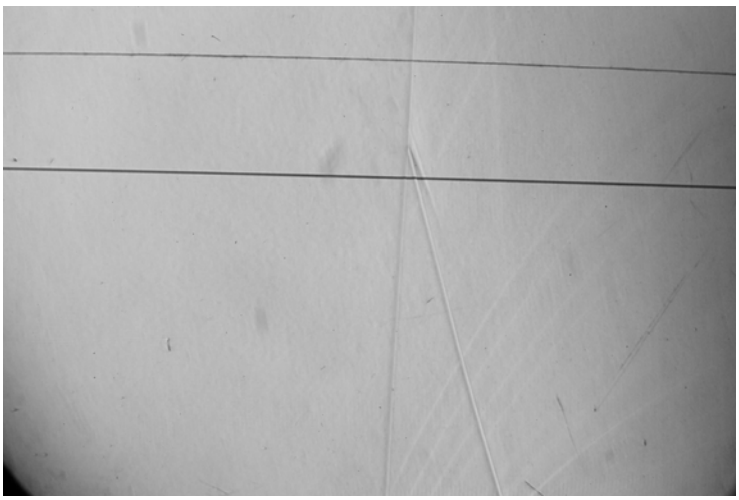


Figure 51: Schlieren photograph G221900A



Figure 52: Schlieren photograph G321800A

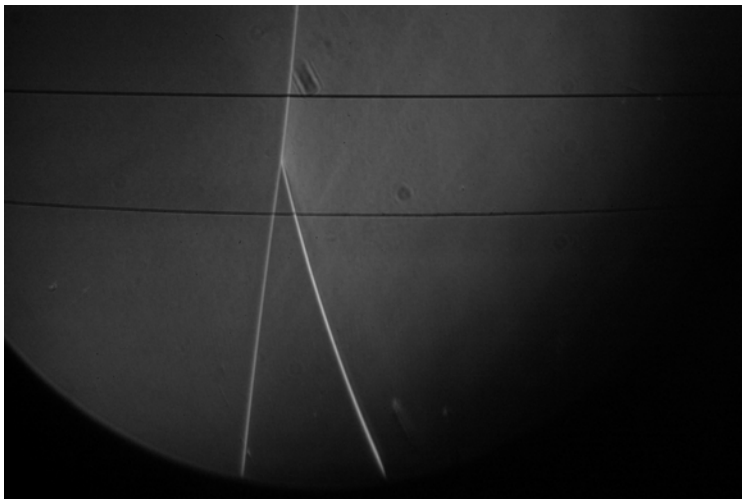


Figure 53: Schlieren photograph K222000A

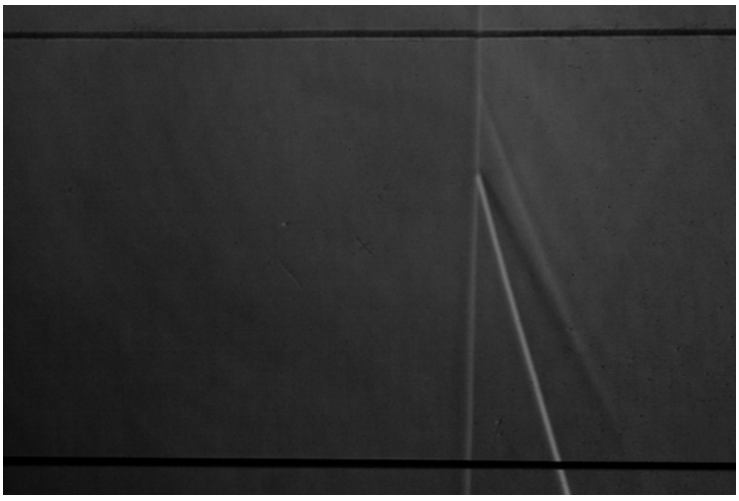


Figure 54: Schlieren photograph M221900B



Figure 55: Schlieren photograph M221960A

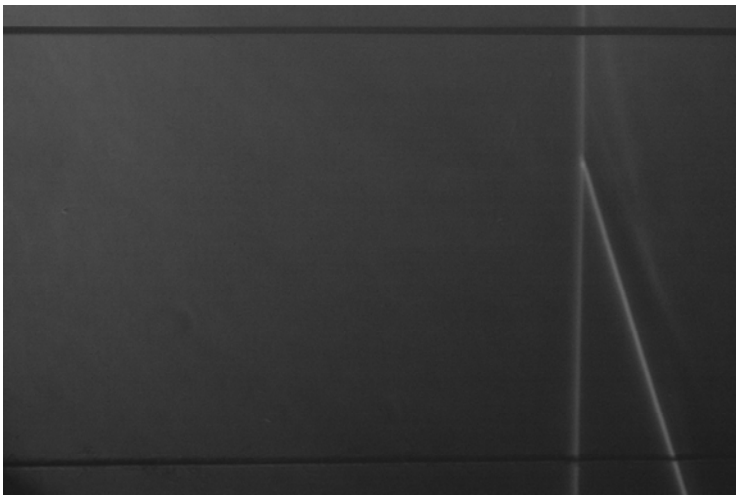


Figure 56: Schlieren photograph N221970B

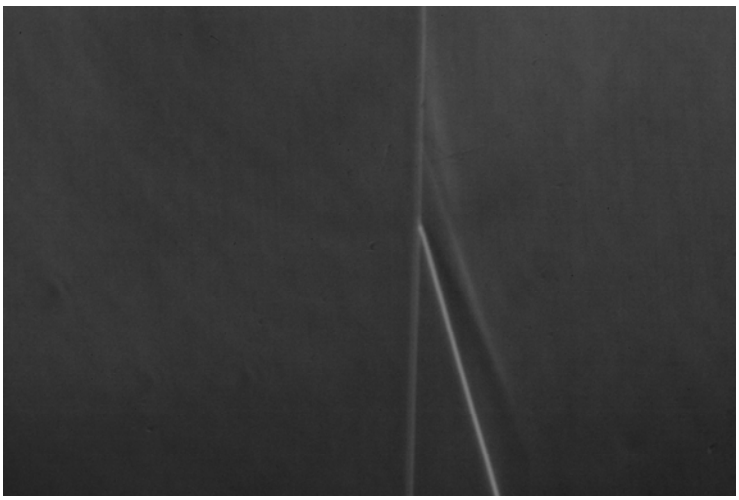


Figure 57: Schlieren photograph P221980C

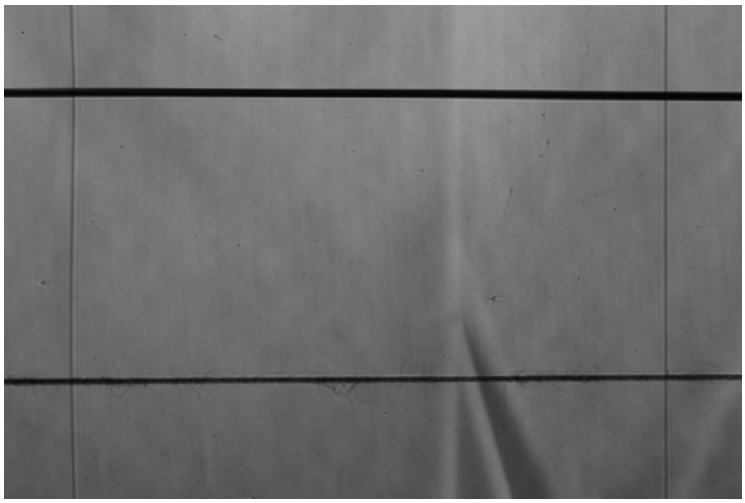


Figure 58: Schlieren photograph R222000C

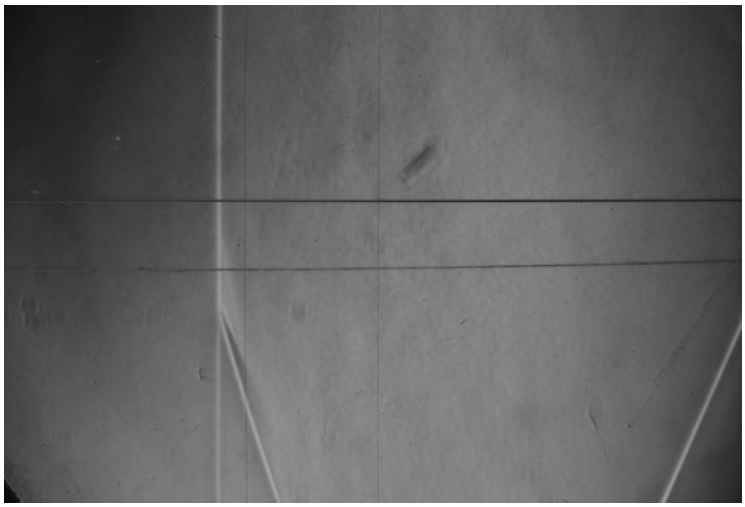


Figure 59: Schlieren photograph S222080A

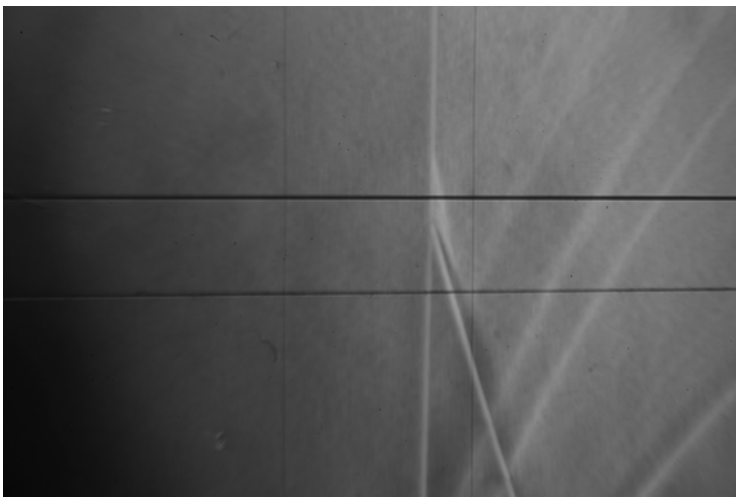


Figure 60: Schlieren photograph T221980A

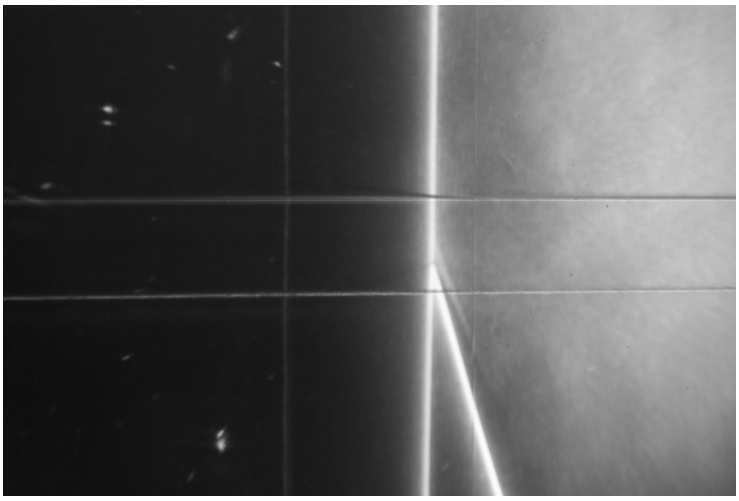


Figure 61: Schlieren photograph T221980B

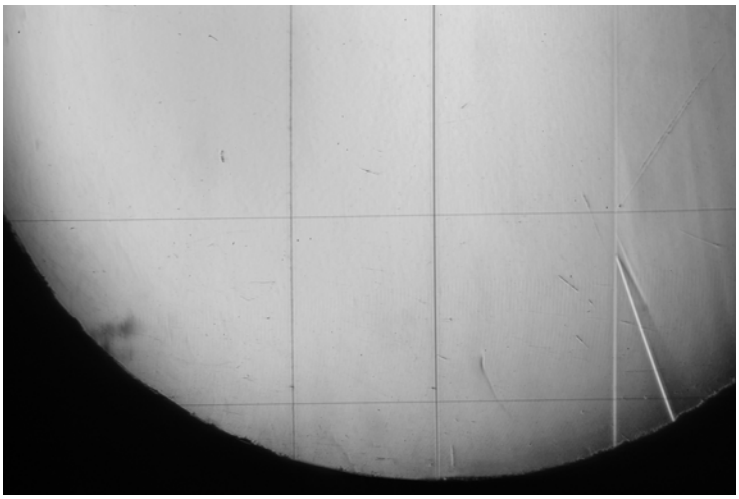


Figure 62: Schlieren photograph V31750A

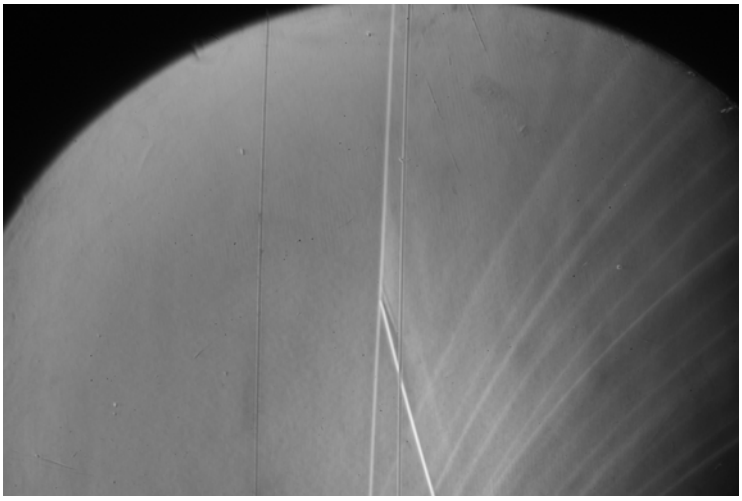


Figure 63: Schlieren photograph V181950A

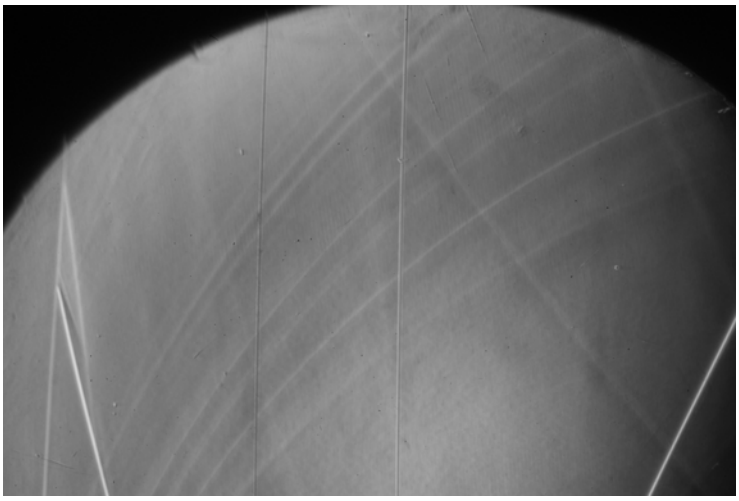


Figure 64: Schlieren photograph V182250A

An attempt was made to improve the flow visualisation by using contact shadowgraph technique, and the following figure shows one of the examples:

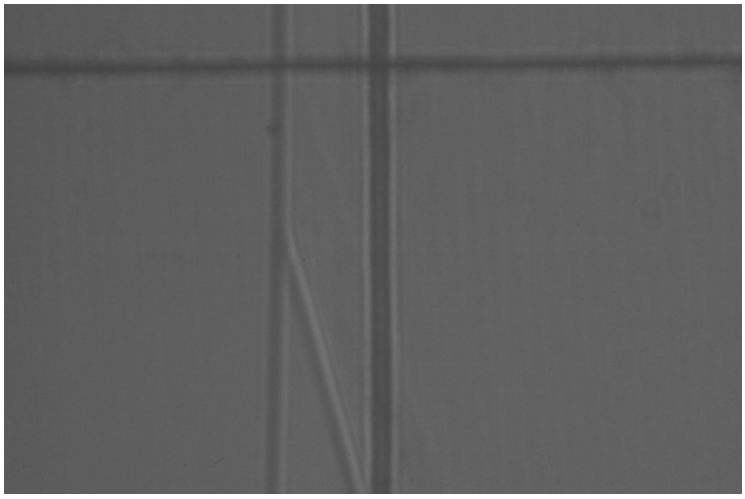


Figure 65: Contact shadowgraph photograph W22198E

6.2.2 Multiple-frame Photographs

The photographs taken by the million-frame per second camera are used to analyse the Mach number in different regions around the triple point. These photographs have either three or five overlaid pictures of the triple point at set time intervals between them. For an image to be considered suitable for analysis, the series of triple points must have fallen between the two vertical guides and above the lower guide (produced by fixing thin strings across the test section windows). This was thought to ensure a more accurate scaling factor for the speed analysis. These images were named using a similar convention to the single frame images,

except that the first digit now indicates the orientation of the knife edges; i.e. “A” for angled knife edges (approximately 15 degrees to the vertical) and “V” for vertical knife edges. A selection of these images is shown below, with the processed images used for analysis:

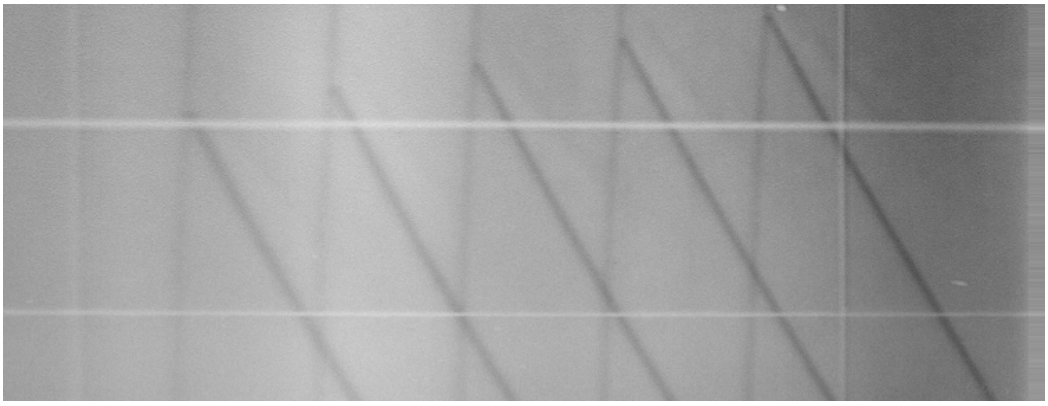


Figure 66: Photograph V221960K (unprocessed)

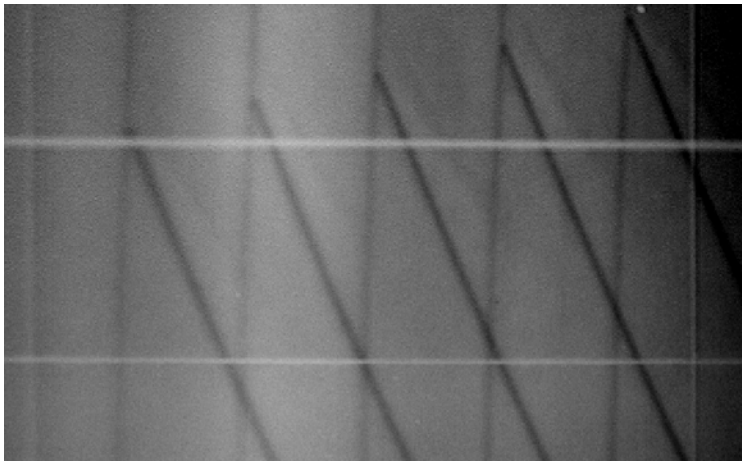


Figure 67: Photograph V221960K (processed)

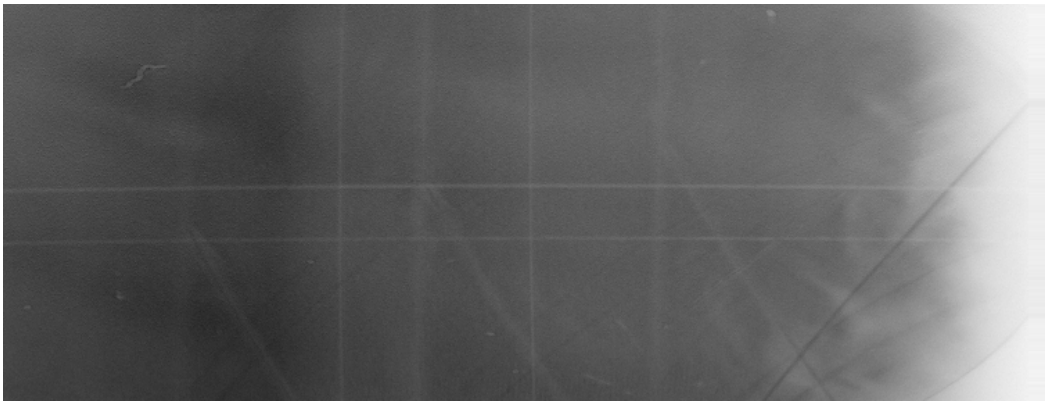


Figure 68: Photograph A221620B (unprocessed)

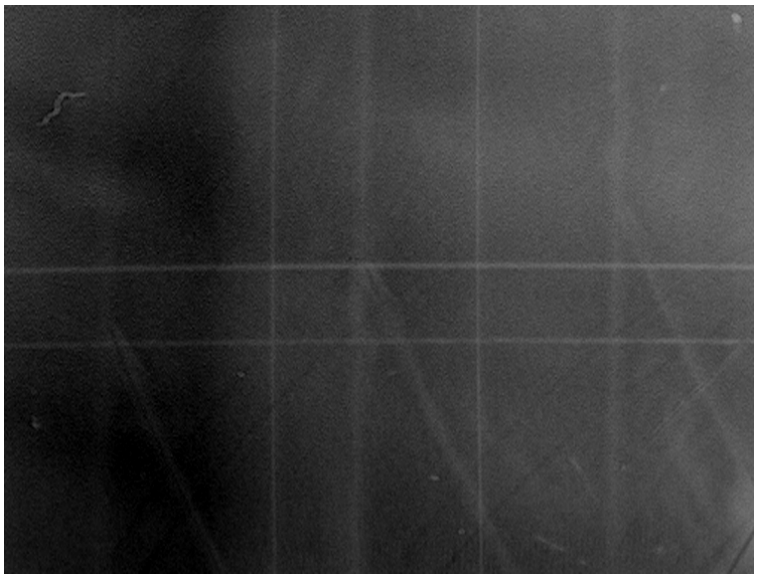


Figure 69: Photograph A221620B (processed)



Figure 70: Photograph A181620A (unprocessed)

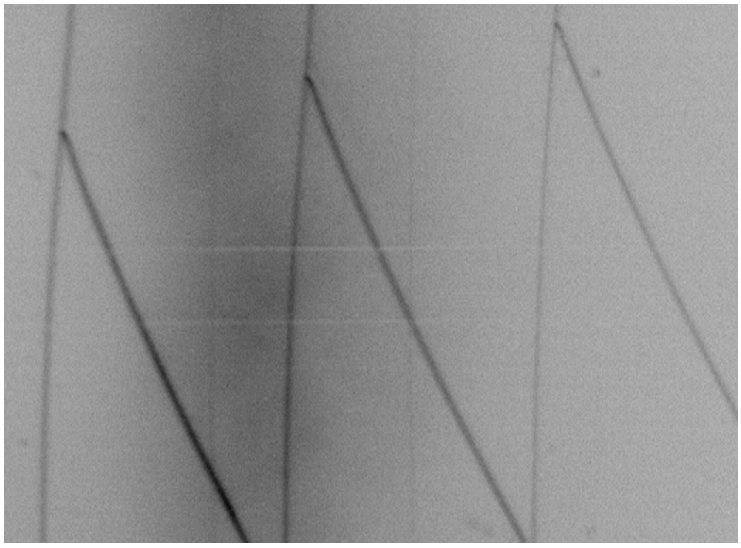


Figure 71: Photograph A181620A (processed)



Figure 72: Photograph A181620H (unprocessed)

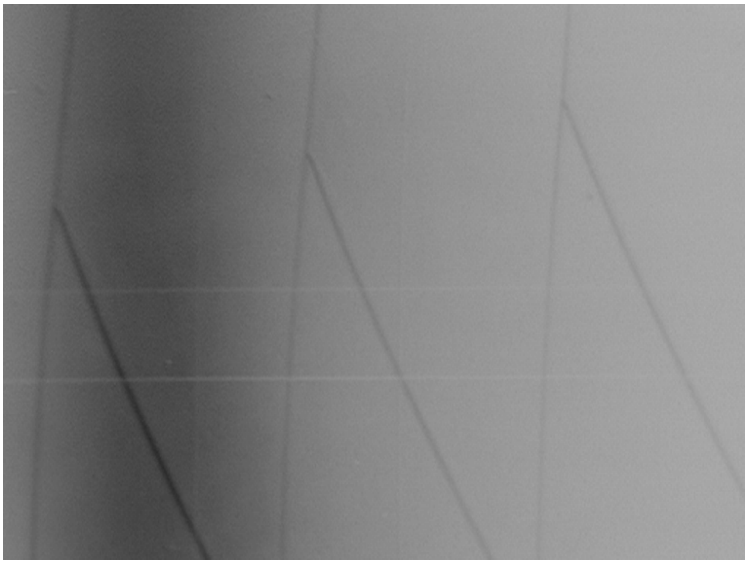


Figure 73: Photograph A181620H (processed)



Figure 74: Photograph A31600A (unprocessed)

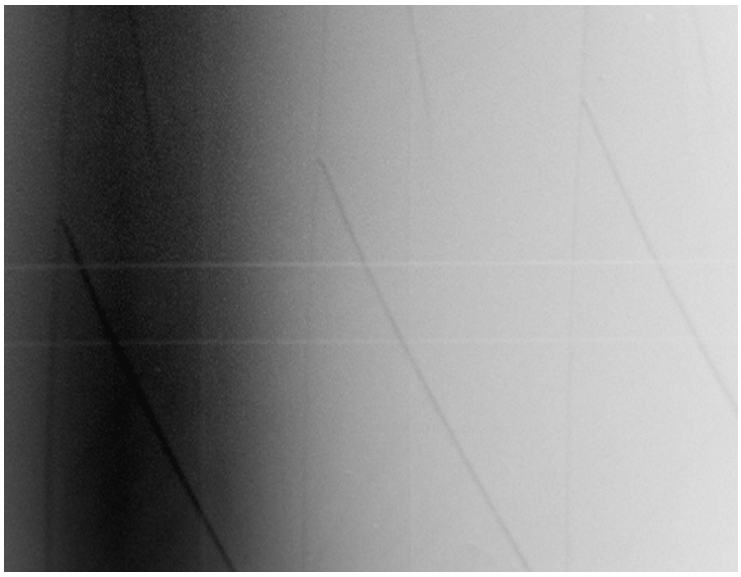


Figure 75: Photograph A31600A (processed)



Figure 76: Photograph A31620H (unprocessed)

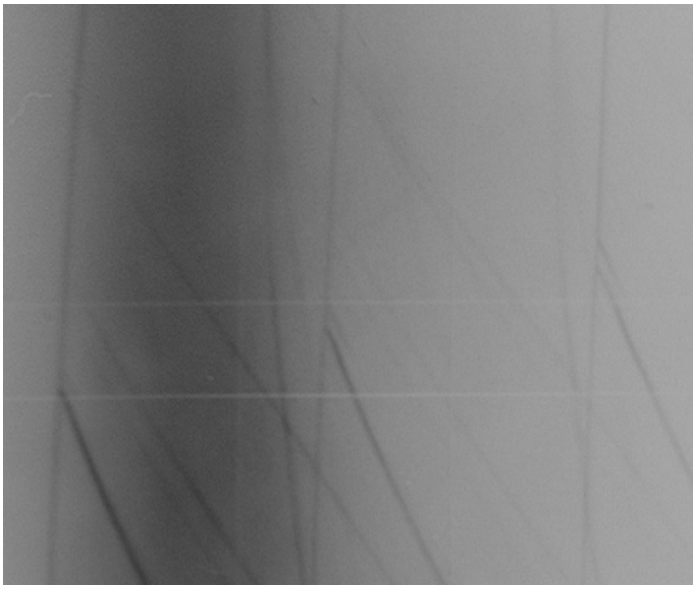


Figure 77: Photograph A31620H (processed)

A more accurate measurement system was used after the primary testing. More rigid strings (fish line) were used in a machined groove in the frame 50 mm apart. The strings were tightened to avoid any possible vibration. Some of the photos are shown below with the improved system:

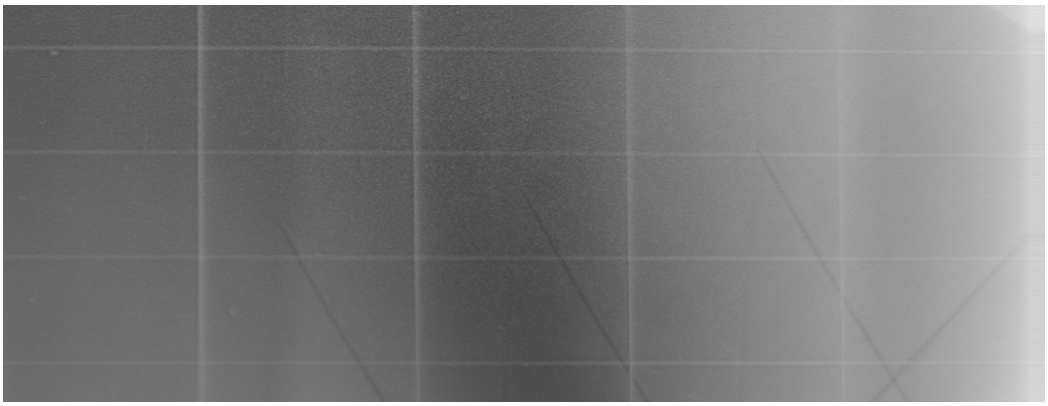


Figure 78: Photograph C221620A (unprocessed)

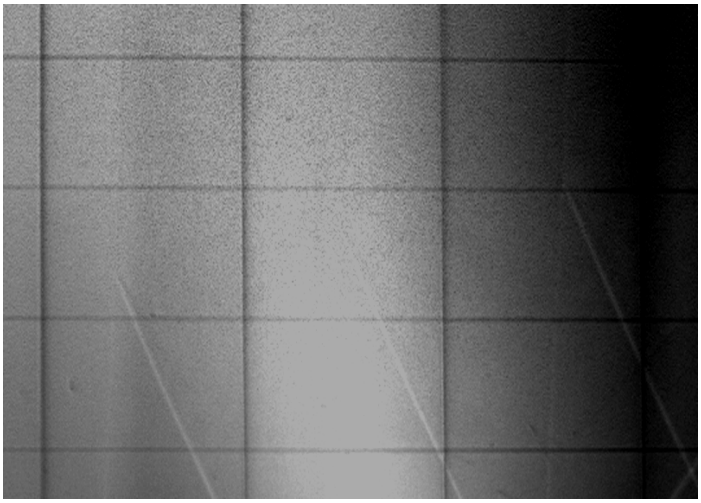


Figure 79: Photograph C221620A (processed)

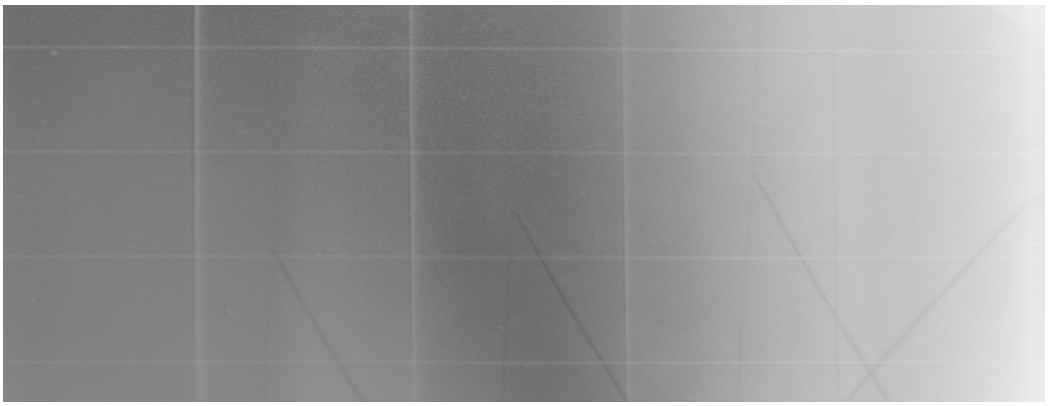


Figure 80: Photograph C221620B (unprocessed)

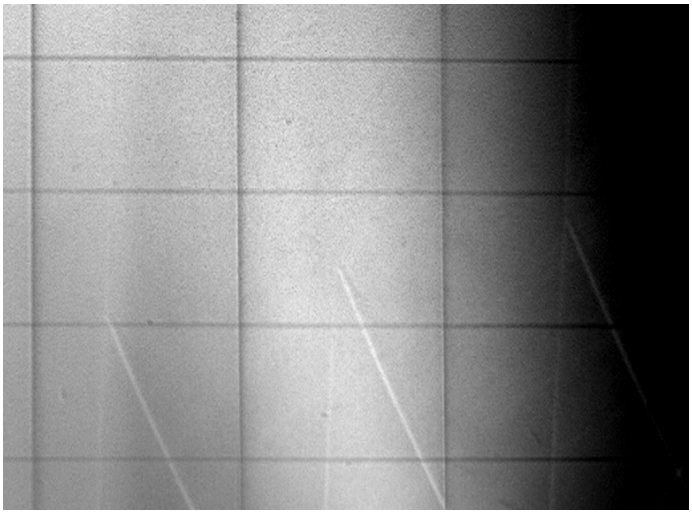


Figure 81: Photograph C221620B (processed)

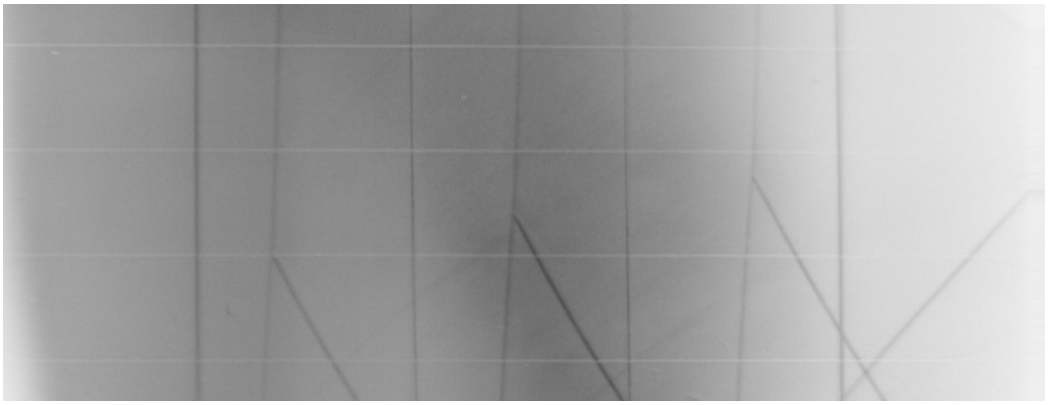


Figure 82: Photograph C221620C (unprocessed)

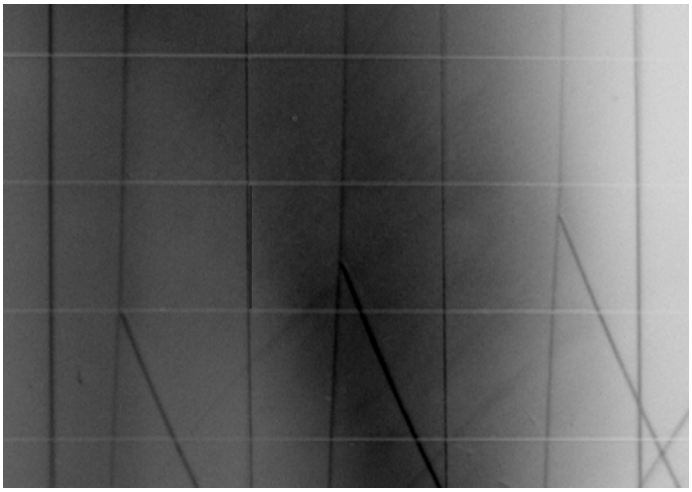


Figure 83: Photograph C221620C (processed)

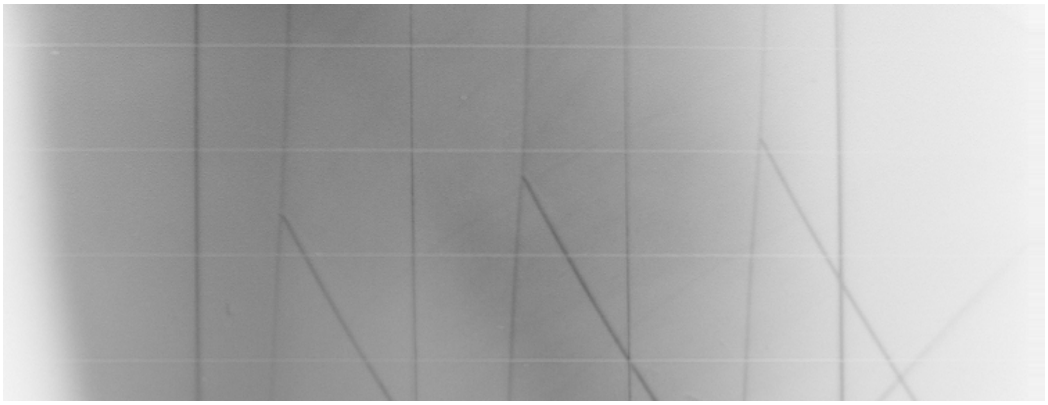


Figure 84: Photograph C221620D (unprocessed)

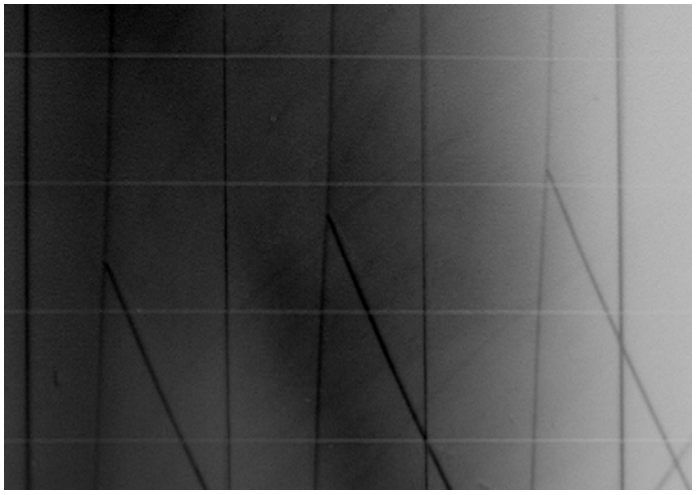


Figure 85: Photograph C221620D (processed)

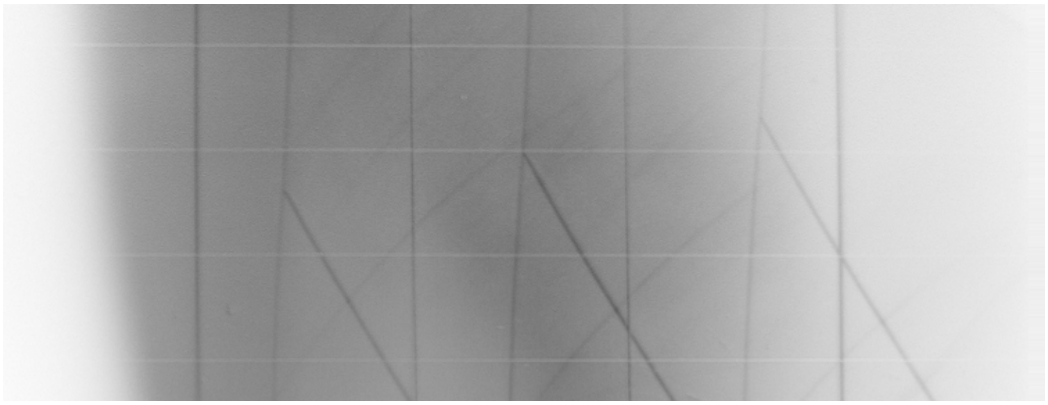


Figure 86: Photograph C221620E (unprocessed)

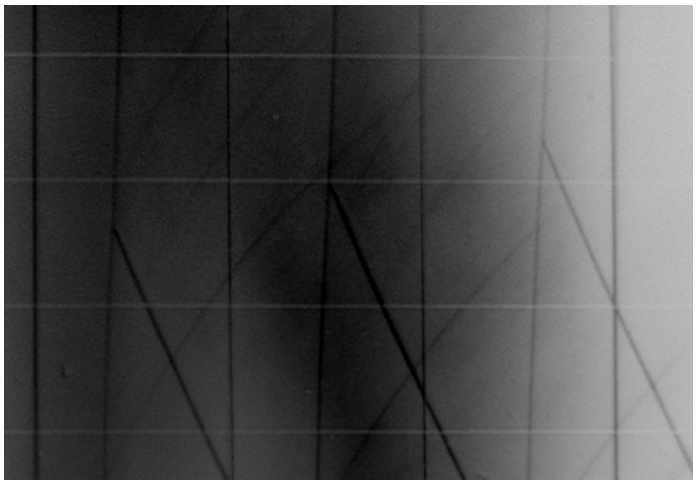


Figure 87: Photograph C221620E (processed)

6.3 Data processing

6.3.1 Assumptions

The following assumptions were made when using the oblique shock wave calculations:

- Flow field is assumed to be two dimensional, thus no three dimensional effects.
- Viscosity effects neglected as the distance between the triple point at the test section and the corner which the incident shock first encountered of the shock tube is large.
- Pseudo-steady state is assumed.
- Heat transfer does not take place.
- The Mach stem, incident and reflected shocks are to be planar.
- The triple point moves along a straight line across the image i.e. it is self-similar. This is approximately true since the incident wave will have a radius of curvature in excess of 6 m when it crosses the window.

6.3.2 Image Processing

The photographs were first processed using Adobe® Photoshop® 5 Limited Edition to enhance the picture quality and enlarged for clarity. The distances between the incident shock wave and the angles of between the incident and reflected shock wave are then measured by using Microsoft™ Paint. This program is capable of reading coordinates of every pixel along the shock waves on a specific photograph. However, some of the shock waves exhibited a small curvature. This meant it was inaccurate to use a single line to obtain the coordinates.

Also, there is always a finite thickness to the shock waves. Therefore, two lines were placed bounding each shock wave, and an average of the distance between was used to derive the coordinates of these shock waves. It was then possible to obtain the distances between points on each shock wave by subtracting different coordinates. Thus, the angles between the various shock waves could also be obtained. Microsoft® Paint drawing showing the typical construction used is shown below:



Figure 88: Microsoft® Paint drawing for shock wave measurements for three frame image

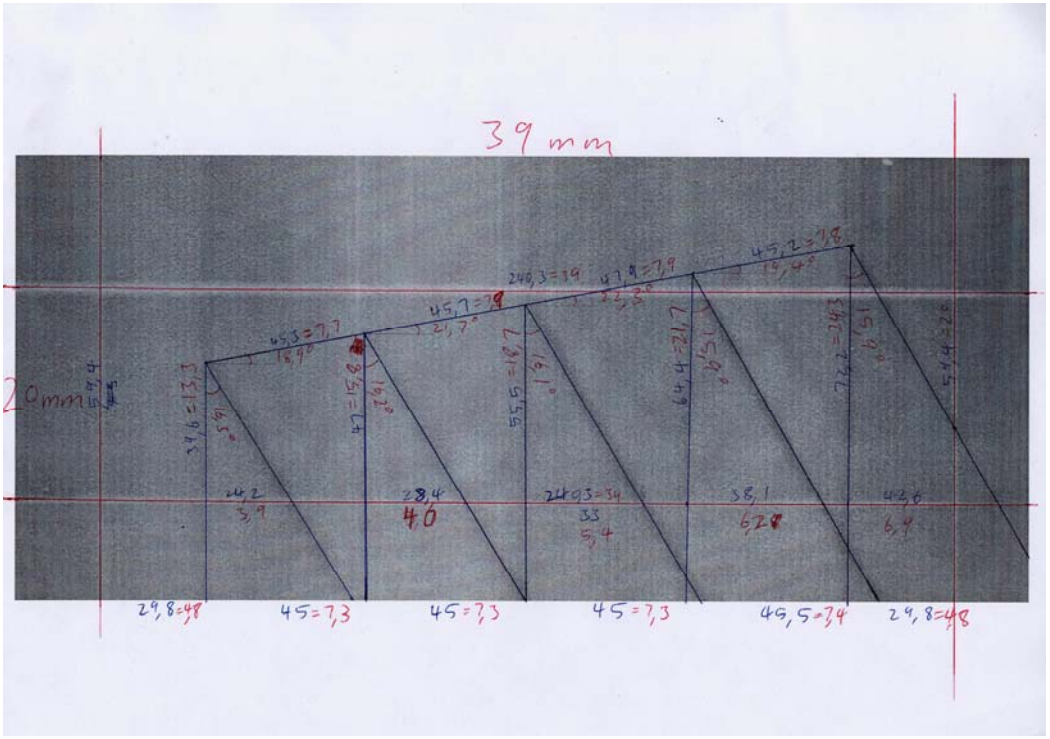


Figure 89: Rough sketch of the measurements between five triple points

6.3.3 Image Processing Procedure

The following section describes the step-by step procedure of image processing from enhancing the raw photograph to obtaining the final calculation results:

1) Opened the raw photograph in Adobe® Photoshop® 5.
2) Cropped the image to leave out blank portions.
3) Enlarged the image, 150% in width and 200% in height, to fit the screen.
4) Adjusted the brightness and contrast accordingly (usually darkened and increased contrast of the image).
5) Saved the image with a different name and opened it in Microsoft® Paint.
6) Drew straight lines bounding each shock wave as shown in Figure 88 above.
7) Zoomed into the three triple points.
8) Obtained the x (positive to the right) and y (positive downward) coordinates at the four intersections of the lines at the triple point.
9) Zoomed into the intersections of the lowest wire and the shock waves.
10) Obtained four set of x and y coordinates at each of the eight intersections.
11) Obtained the averages of the four set of x and y coordinates for all intersections (except wire intersections).

12) Obtained the maximum and minimum lengths (both x and y) of each section of the wires by drawing straight lines between the wire intersection points.
13) Obtained the average lengths of each section of the wires.
14) Insert all lengths (including the known distances between wires) and coordinates into a Matlab® program, code written by Mr. Randall Paton (Appendix B), to correct any photographic distortions.
15) Obtained the true coordinates of the triple points and the shock waves intersection with the lowest wire.
16) Calculated the distances and angles between all shock waves by subtracting their coordinates.
17) Entered the distances and angles into the EES® program to obtain the final results shown in the Oblique Shock Calculations section below.

6.3.4 Sample Calculations

The analysis of the triple point regions are done by using the oblique shock wave theory (Skews 2001). It is possible to obtain the speed and the wave diffraction angles between the regions (1), (2) and (3) given in figure 90 below:

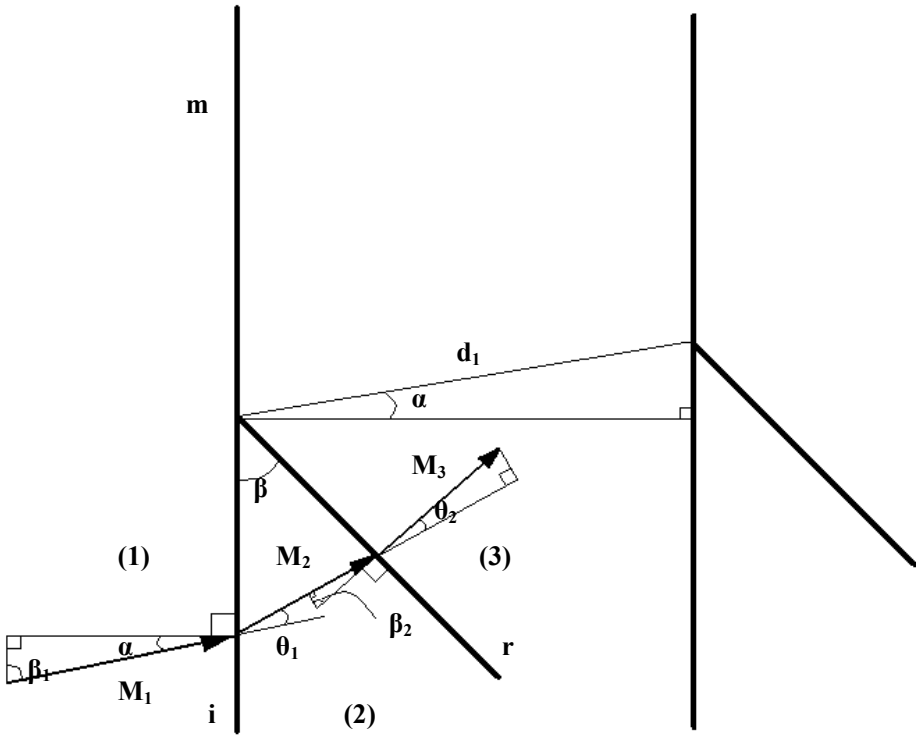


Figure 90: Detailed sketch of flow in a reference frame fixed in the first triple point

The sample selected is test number A181620H, and Run 1 (using the triple point on the left hand side) is shown below:

Date:	15-08-2007
Test number:	5
Burst pressure:	1.8 bar (gauge)
Time delay:	1620 μs
Exposure time:	2 μs (per picture)
Time between exposures:	150 μs
Time between each shock wave:	152 μs
Number of exposures overlaid:	3
Photograph number:	A181620H

Traces file name:	A181620H
Ambient atmospheric pressure:	0.833 bar
Ambient atmospheric temperature:	14.4 °C
Shock tube configuration:	full length with test section at the bottom end
Parabolic mirrors:	12.5 inch in diameter
Knife edge orientation:	inclined at 15 degrees
Distances between guides in test section:	31 mm (height), 44 mm (wide)
Test remarks:	clear picture and clean traces

The equation for Mach number:

$$M_1 = \frac{V_1}{a} \qquad \textbf{4}$$

The equation for velocity:

$$V_1 = \frac{d_1}{t_1} \qquad \textbf{5}$$

Distance between incident shocks in the flow (M_1) direction:

$d_1 = 56.38mm$

Time between exposures:

$t_1 = 0.00015s$

The velocity of the triple is:

$\therefore V_1 = 375.87m/s$

The equation for speed of sound:

$$a = \sqrt{\gamma RT} \qquad \textbf{6}$$

Reference conditions:

$\gamma = 1.4$
$R = 287J/KgK$
$T = (14.4 + 273)K$

$\therefore a = 339.82m/s$
$\therefore M_1 = 1.106$

$$\beta = \tan^{-1}\frac{3.031}{56.77} + \tan^{-1}\frac{15.05}{56.77}$$

$$\beta = 17.90°$$

$$\alpha = \tan^{-1}\frac{35.48}{107.6}$$

$$\alpha = 18.24°$$

$$\beta_1 = 90° - \alpha$$

$$\therefore \beta_1 = 71.76°$$

By substituting M_1 and β_1 into equation (3), we obtain the following:

$$\tan(\theta_1) = 2\cot(\beta_1)\left[\frac{M_1^2\sin^2(\beta_1) - 1}{M_1^2(\gamma + \cos(2\beta_1)) + 2}\right] \quad \textbf{4}$$

$$\therefore \theta_1 = 1.431°$$

By substituting M_1, β_1 and θ_1 into equation (2):

$$M_2\sin(\beta_1 - \theta_1) = \left[\frac{\left(\frac{2}{\gamma - 1}\right) + M_1^2\sin^2(\beta_1)}{\frac{2\gamma}{(\gamma - 1)}M_1^2\sin^2(\beta_1) - 1}\right]^{\frac{1}{2}} \quad \textbf{5}$$

$$\therefore M_2 = 1.012$$

$$\beta_2 = 90° + \beta - \alpha - \theta_1$$

$$\therefore \beta_2 = 88.23°$$

Now substituting M_2 and β_2 into equation (3):

$$\tan(\theta_2) = 2\cot(\beta_2)\left[\frac{M_2^2\sin^2(\beta_2) - 1}{M_2^2(\gamma + \cos(2\beta_2)) + 2}\right] \quad \textbf{6}$$

$$\therefore \theta_2 = 0.034°$$

Finally, by substituting M_2, β_2 θ_2 into equation (2):

$$M_3 \sin(\beta_2 - \theta_2) = \left[\frac{\left(\frac{2}{\gamma - 1}\right) + M_2^2 \sin^2(\beta_2)}{\frac{2\gamma}{(\gamma - 1)} M_2^2 \sin^2(\beta_2) - 1} \right]^{\frac{1}{2}} \qquad 7$$

$\therefore M_3 = 0.989$

6.3.5 Oblique Shock Calculations (Primary)

The calculations were solved using a program in EES® (Engineering Equation Solver) based on the oblique shock wave equations shown in section 2.3 above. The code can be found in Appendix B. Table 3 to table 5 below are the results of these calculations ("1&3" or "1&5" means calculations obtained by the two furthest triple points apart, and the averages of these measurements are named "good average"). At this stage anomalies in the results were evident because of the very weak reflected wave.

Table 3: Oblique shock calculations for burst pressure of 1.8 bar

Test name	Run No.	β (deg)	d (mm)	t (s)	M1	M2	M3	θ1 (deg)	θ2 (deg)
A181620A	1	18.17	56.5	0.00015	1.106	1.009	0.9916	1.458	0.01883
	2	18.78	57.39	0.00015	1.124	0.9968	1.004	1.922	-0.00639
	1&3	18.17	113.7	0.0003	1.113	1.004	0.9965	1.638	0.009527
A181620B	1	18.42	57.07	0.00015	1.117	1.003	0.9978	1.742	0.006136
	2	18.78	57.73	0.00015	1.13	0.994	1.007	2.088	-0.01524
	1&3	18.42	114.6	0.0003	1.122	0.9997	1.001	1.863	-0.00174
A181620C	1	19.39	56.97	0.00015	1.115	1.001	0.9993	1.717	0.000202
	2	19.66	58.09	0.00015	1.137	0.9859	1.014	2.296	-0.01121
	1&3	19.39	115	0.0003	1.125	0.9939	1.006	1.978	-0.00436
A181620D	1	17.78	56.77	0.00015	1.114	1.001	0.9998	1.681	0.001799
	2	18.27	57.57	0.00015	1.129	0.9903	1.011	2.094	-0.02674
	1&3	17.78	114.1	0.0003	1.12	0.997	1.004	1.833	-0.01051
A181620E	1	17.73	56.35	0.00015	1.105	1.018	0.9844	1.362	0.06661
	2	18.37	58	0.00015	1.138	0.9957	1.006	2.248	-0.02323
	1&3	17.73	114.1	0.0003	1.119	1.008	0.9939	1.725	0.03329
A181620F	1	17.17	56.48	0.00015	1.108	1.012	0.9902	1.468	0.05027
	2	17.65	57.83	0.00015	1.135	0.9941	1.009	2.184	-0.03506
	1&3	17.17	114.1	0.0003	1.119	1.004	0.9984	1.773	0.015
A181620G	1	17.58	56.81	0.00015	1.115	1.013	0.9901	1.598	0.05367
	2	17.57	57.87	0.00015	1.135	0.9985	1.005	2.17	-0.01867
	1&3	17.58	114.6	0.0003	1.124	1.006	0.9967	1.849	0.02486
A181620H	1	17.9	56.38	0.00015	1.106	1.012	0.9894	1.433	0.03329
	2	18.03	57.17	0.00015	1.122	1.001	1	1.849	0.000852
	1&3	17.9	113.3	0.0003	1.112	1.008	0.9936	1.588	0.02271
Average		18.14	76.19	0.0002	1.120	1.0019	0.9995	1.815	0.007663
Good Average		18.02	114.19	0.00030	1.119	1.0026	0.9988	1.781	0.011098

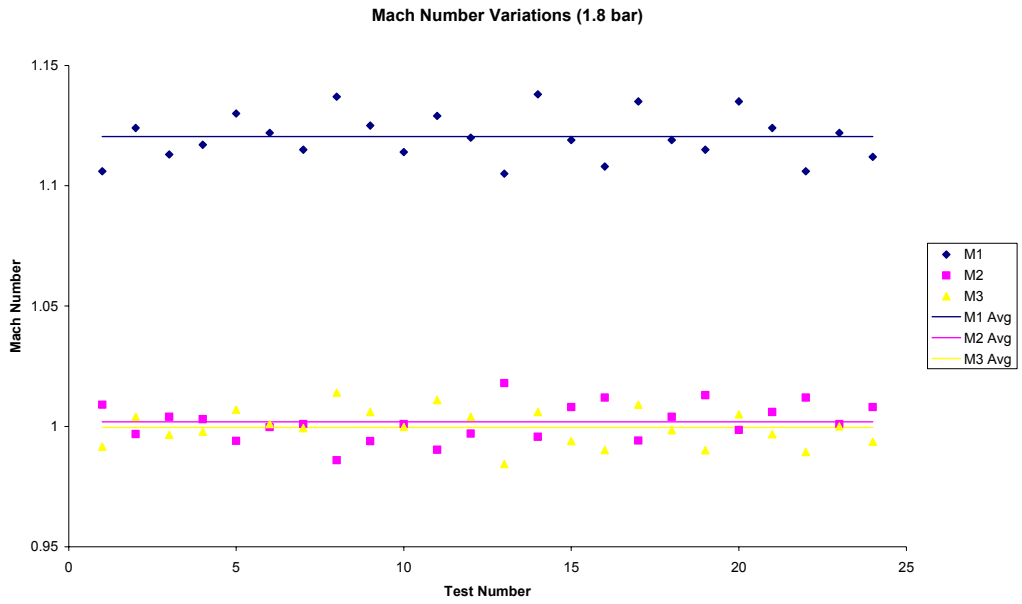


Figure 91: Mach number variations for burst pressure of 1.8 bar

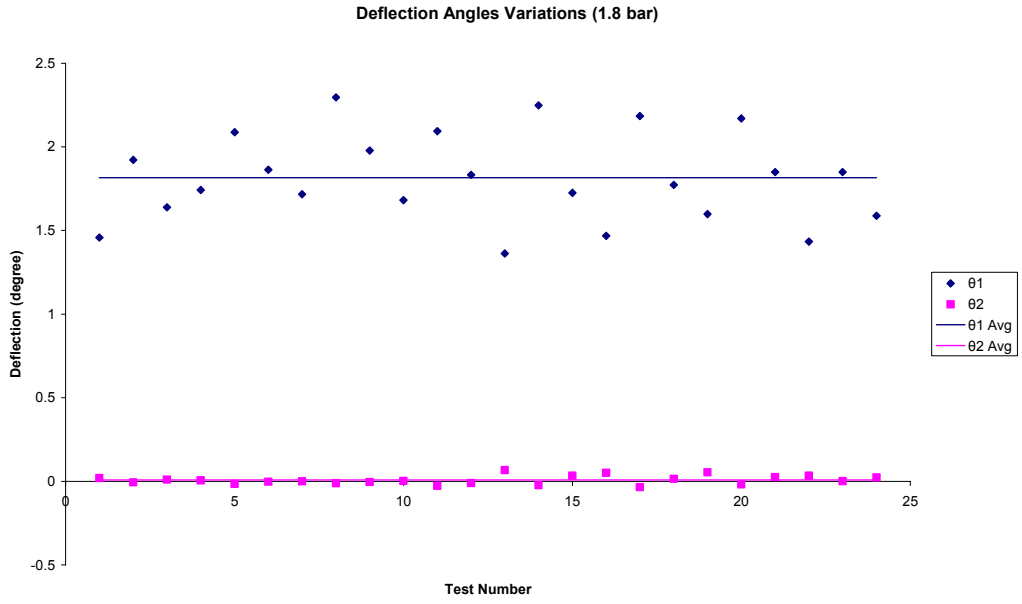


Figure 92: Deflection angles variations for burst pressure of 1.8 bar

Table 4: Oblique shock calculations for burst pressure of 2.2 bar

Test name	Run No.	β (deg)	d (mm)	t (s)	M1	M2	M3	θ1 (deg)	θ2 (deg)
V221960M	1	16.66	7.76	0.00002	1.141	1.006	1.003	2.241	0.01635
	2	16.82	7.65	0.00002	1.125	1.017	0.9905	1.781	0.1057
	3	17.13	7.82	0.00002	1.15	1.001	1.007	2.491	-0.02872
	4	17.45	8.05	0.00002	1.184	0.9806	1.03	3.446	-0.2331
	1&5	16.66	31.27	0.00008	1.15	1.001	1.009	2.481	-0.03614
V221960N	1	15.76	7.63	0.00002	1.122	1.007	1	1.811	0.02891
	2	16.52	7.96	0.00002	1.171	0.9764	1.033	3.14	-0.2518
	3	16.64	8.06	0.00002	1.186	0.9679	1.043	3.541	-0.3486
	4	15.86	7.74	0.00002	1.138	0.9965	1.012	2.256	-0.06638
	1&5	15.76	31.33	0.00008	1.152	0.9878	1.022	2.628	-0.1607
V221960K	1	16.28	7.93	0.00002	1.166	1.012	1.007	2.763	0.03148
	2	16.03	7.93	0.00002	1.166	1.012	1.009	2.763	0.02413
	3	15.6	7.73	0.00002	1.137	1.03	0.9894	1.886	0.2647
	4	15.89	7.56	0.00002	1.112	1.047	0.9698	1.135	0.4399
	1&5	16.28	31.14	0.00008	1.145	1.025	0.9921	2.128	0.2011
V221960L	1	17.36	7.78	0.00002	1.144	0.9935	1.011	2.411	-0.05804
	2	16.71	7.99	0.00002	1.175	0.9746	1.035	3.257	-0.2672
	3	16.36	7.93	0.00002	1.166	0.9799	1.03	3.016	-0.2267
	4	16.07	7.8	0.00002	1.147	0.9916	1.017	2.492	-0.1112
	1&5	17.36	31.52	0.00008	1.159	0.9843	1.022	2.815	-0.1335
A221700A	1	19.49	38.5	0.0001	1.134	0.9972	1.003	2.144	-0.00652
	2	18.8	38.27	0.0001	1.127	1.002	0.9993	1.96	0.003643
	1&3	19.49	76.77	0.0002	1.13	0.9994	1.001	2.052	-0.00153
A221700D	1	18.55	38.72	0.0001	1.14	0.9982	1.004	2.283	-0.01415
	2	18.22	37.84	0.0001	1.114	1.016	0.9866	1.565	0.05888
	1&3	18.55	76.52	0.0002	1.127	1.007	0.9948	1.908	0.02494
A221620B	1	18.93	58.27	0.00015	1.143	1	1.002	2.333	-0.00444
	2	18.36	57.79	0.00015	1.134	1.006	0.9967	2.07	0.02511
	1&3	18.93	116.1	0.0003	1.138	1.003	0.9989	2.201	0.009685
A221620J	1	18.02	57.62	0.00015	1.134	1.001	1.002	2.109	-0.0006
	2	18.08	58.51	0.00015	1.151	0.9901	1.014	2.591	-0.06786
	1&3	18.02	115.9	0.0003	1.14	0.9971	1.006	2.292	-0.02452
A221620N	1	18.81	57.37	0.00015	1.128	1.001	1	1.994	0.0014
	2	18.66	57.57	0.00015	1.132	0.9983	1.003	2.101	-0.008
	1&3	18.81	114.5	0.0003	1.126	1.003	0.9983	1.927	0.006288
A221620R	1	18.89	57.52	0.00015	1.127	1.006	0.9949	1.927	0.02006
	2	18.79	58.56	0.00015	1.148	0.9932	1.009	2.49	-0.03638
	1&3	18.89	116	0.0003	1.137	1	1.001	2.184	-0.00215
A221620U	1	18.01	56.9	0.00015	1.115	1.021	0.9825	1.524	0.101
	2	19.38	59.42	0.00015	1.165	0.9893	1.014	2.915	-0.06313
	1&3	18.01	116.2	0.0003	1.139	1.005	0.9989	2.185	0.02023
Average		17.58	41.84	0.00011	1.143	1.0006	1.0059	2.323	-0.018728
Good Average		17.89	77.93	0.00020	1.140	1.0011	1.0040	2.255	-0.008754

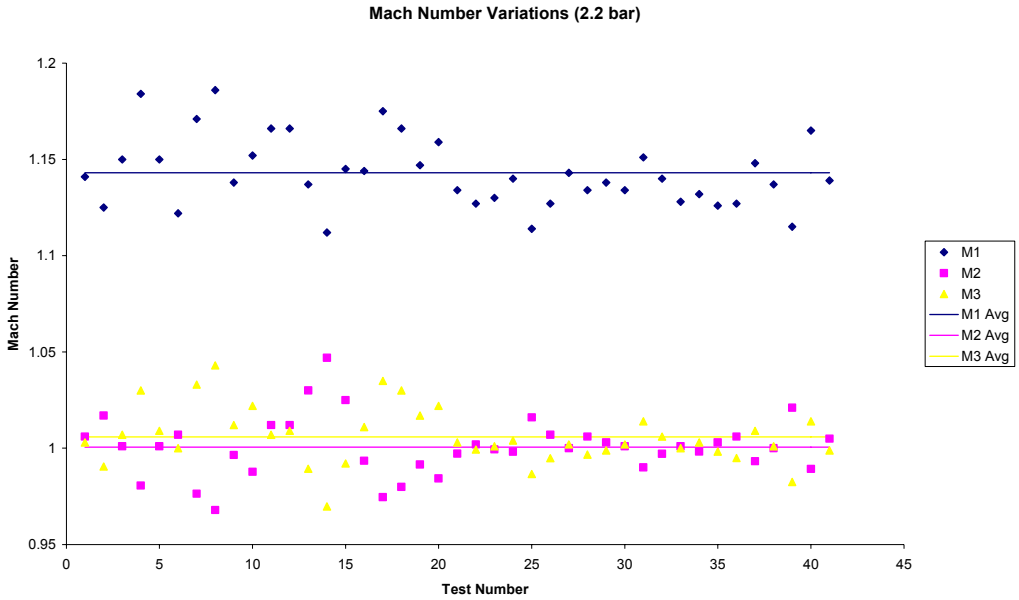


Figure 93: Mach number variations for burst pressure of 2.2 bar

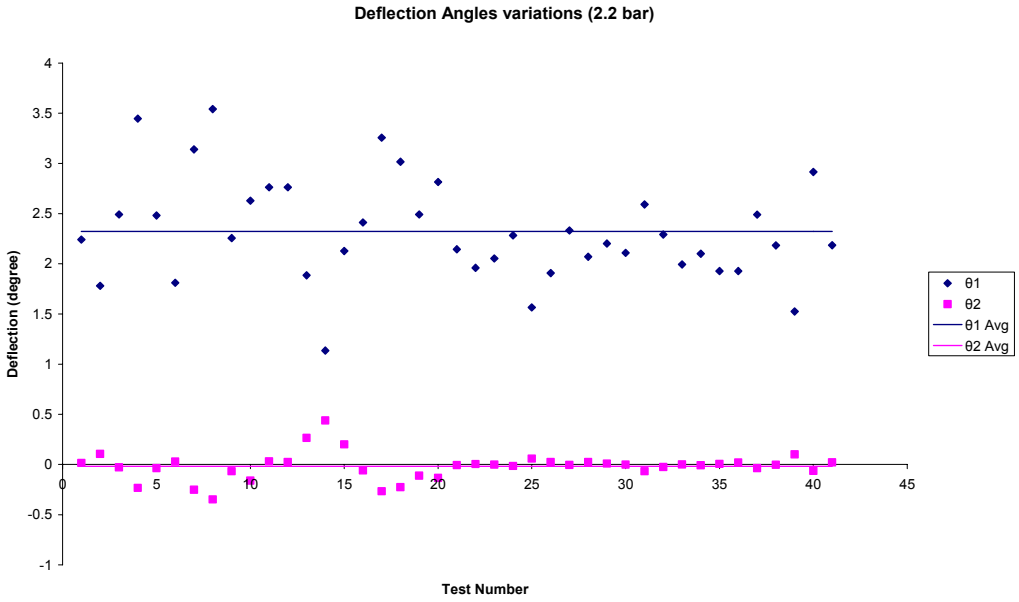


Figure 94: Deflection angles variations for burst pressure of 2.2 bar

Table 5: Oblique shock calculations for burst pressure of 3 bar

Test name	Run No.	β (deg)	d (mm)	t (s)	M1	M2	M3	θ1 (deg)	θ2 (deg)
A31600A	1	19.6	57.81	0.00015	1.132	1.004	0.9969	2.048	0.008757
	2	19.97	58.44	0.00015	1.144	0.9958	1.005	2.39	-0.01136
	1&3	19.6	116	0.0003	1.135	1.002	0.9991	2.138	0.003426
A31600B	1	19.01	56.95	0.00015	1.115	1.015	0.9864	1.586	0.03864
	2	19.26	58.37	0.00015	1.143	0.9962	1.005	2.355	-0.016
	1&3	19.01	115.2	0.0003	1.128	1.006	0.9952	1.941	0.01772
A31620H	1	25.29	57.47	0.00015	1.127	1.026	0.9776	1.73	-0.1197
	2	18.32	58.93	0.00015	1.156	1.008	0.9997	2.565	0.03268
	1&3	25.29	116.2	0.0003	1.14	1.018	0.9846	2.091	-0.07185
A31500D	1	17.85	59.36	0.00015	1.165	1.002	1.008	2.829	-0.02854
	2	18.81	61.12	0.00015	1.199	0.9821	1.028	3.825	-0.208
	1&3	17.85	120.3	0.0003	1.18	0.9927	1.018	3.272	-0.1259
A31500F	1	18.4	60.49	0.00015	1.187	0.9876	1.022	3.479	-0.1566
	2	19.52	61.24	0.00015	1.202	0.9796	1.028	3.901	-0.1923
	1&3	18.4	121.4	0.0003	1.192	0.9851	1.025	3.609	-0.1855
A31500G	1	18.9	59.78	0.00015	1.173	0.9922	1.014	3.104	-0.07916
	2	19.1	60.83	0.00015	1.194	0.9806	1.027	3.691	-0.1821
	1&3	18.9	120.5	0.0003	1.182	0.9869	1.02	3.367	-0.1274
A31500H	1	18.31	60.14	0.00015	1.18	1.001	1.011	3.205	-0.04898
	2	18.78	60.9	0.00015	1.195	0.9926	1.019	3.643	-0.1297
	1&3	18.31	120.9	0.0003	1.187	0.9972	1.015	3.396	-0.09136
A31500I	1	18.62	60.1	0.00015	1.179	0.9925	1.016	3.254	-0.0982
	2	19.51	60.72	0.00015	1.192	0.9857	1.021	3.604	-0.1336
	1&3	18.62	120.9	0.0003	1.187	0.9886	1.02	3.458	-0.1399
A31500J	1	19.16	59.42	0.00015	1.166	0.9924	1.012	2.932	-0.05901
	2	19.63	60.4	0.00015	1.185	0.9813	1.023	3.475	-0.1296
	1&3	19.16	118.5	0.0003	1.163	0.9941	1.01	2.848	-0.04668
A31500K	1	18.79	60.09	0.00015	1.179	0.9936	1.014	3.242	-0.08615
	2	19.69	61.41	0.00015	1.205	0.9794	1.028	3.987	-0.1957
	1&3	18.79	121.3	0.0003	1.19	0.9874	1.022	3.561	-0.1507
A31500L	1	19.47	60.12	0.00015	1.18	0.995	1.011	3.244	-0.06015
	2	19.78	60.97	0.00015	1.197	0.9858	1.021	3.727	-0.1354
	1&3	19.47	121.1	0.0003	1.188	0.9904	1.017	3.483	-0.1021
A31500M	1	17.83	60.13	0.00015	1.18	0.9814	1.027	3.343	-0.1941
	2	19.11	60.97	0.00015	1.197	0.9722	1.035	3.804	-0.2214
	1&3	17.83	121	0.0003	1.187	0.9773	1.032	3.546	-0.2408
A31500N	1	18.9	60.67	0.00015	1.191	0.9888	1.02	3.559	-0.1385
	2	19.34	61.64	0.00015	1.21	0.9786	1.031	4.107	-0.2342
	1&3	18.9	122.3	0.0003	1.2	0.9836	1.026	3.833	-0.1975
Average		19.26	79.85	0.00020	1.175	0.9923	1.015	3.158	-0.10864
Good Average		19.24	119.66	0.00030	1.174	0.9930	1.0141	3.119	-0.112196

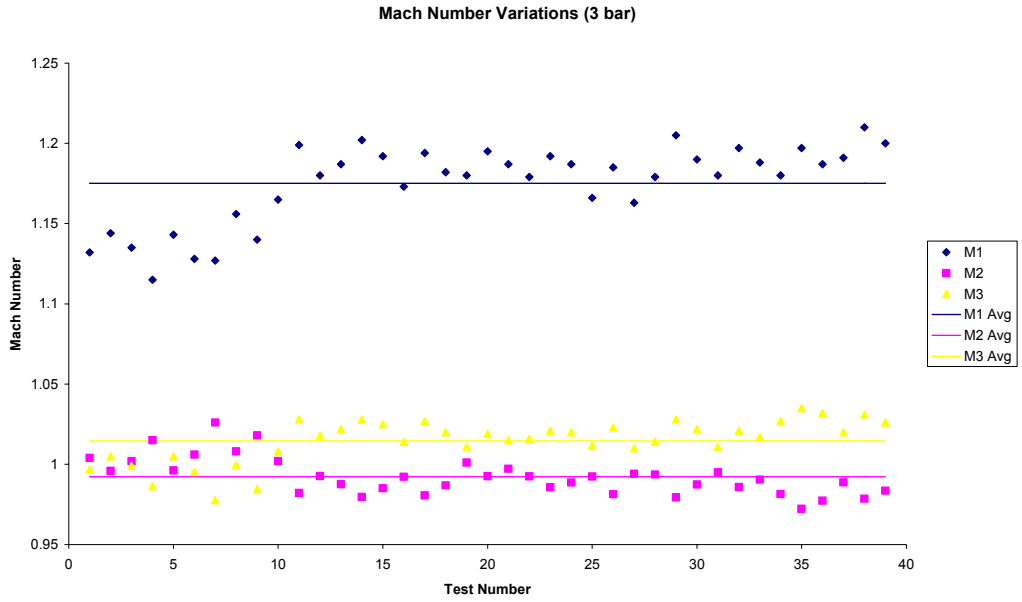


Figure 95: Mach number variations for burst pressure of 3 bar

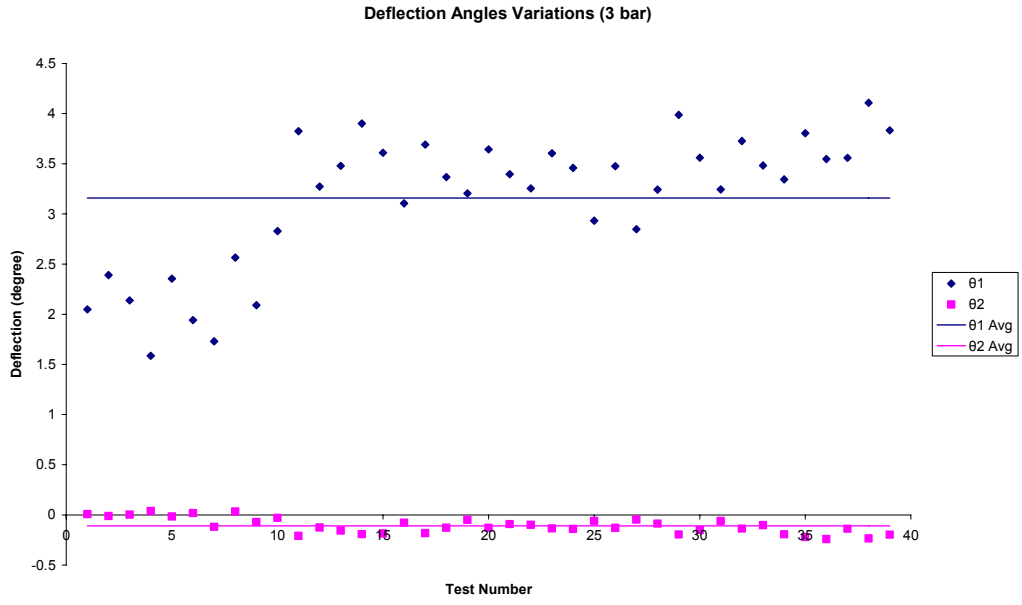


Figure 96: Deflection angles variations for burst pressure of 3 bar

Two types of anomaly are noted from table 3 to table 4. Firstly the Mach number in state 2 can be subsonic so that applying the equations gives a supersonic Mach number in region 3. Secondly even though M_2 is supersonic applying the equations results in M_3 being larger. These results are not physical and in conflict with the second law of thermodynamics. The reasons are the very weak reflected shock and measurement accuracy of angles and distances

off the photographs. It is for this reason that a second set of experiments were conducted with a much more accurate calibration of distances and angles, as indicated below.

6.3.6 Oblique Shock Calculations (Secondary)

There were inconsistencies in the primary calculations due to measurement error caused by the calibration grids were not rigid and the image distortion of the schlieren system by the objective lens. To overcome these, new strings were positioned in machined grooves 50 mm apart and a two stage spline method was used to determine the actual co-ordinates of the triple points and the nearest intersection with the grid of the associated shock waves. For the first stage of the spline method, polynomials were calculated for the variations of the horizontal co-ordinates versus the actual grid along each of the horizontal grid lines and of the vertical co-ordinates versus the actual grid along each of the vertical grid lines. The second stage of the spline method determined the variation of the coefficients of the horizontal co-ordinate polynomials with vertical position and vice versa for the vertical co-ordinate polynomial coefficients. Once these functions were derived a measured intersection point of the shock wave with the grid could be transformed into a true geometric value. These calculations were performed using Mr. Randall Paton's Matlab code. The logic of the calculation is the same as the primary code but with higher accuracy and an uncertainty analysis. This code can be found in Appendix C. The secondary calculations are shown below in table 6 and the results are plotted with uncertainty in figure 97 to figure 100.

Table 6: Secondary oblique shock calculations

Test name	β (deg)	±Δβ (deg)	M1	±ΔM1	M2	±ΔM2	M3	±ΔM3	θ1 (deg)	±Δθ1 (deg)	θ2 (deg)	±Δθ2 (deg)
A181620A1	68.558	0.854	1.147	0.001	1.024	0.04	0.987	0.016	2.171	0.312	0.188	0.414
A181620B1	69.779	0.857	1.137	0.001	1.014	0.037	0.991	0.014	2.077	0.276	0.079	0.31
A181620C1	70.379	0.844	1.127	0.001	1.014	0.035	0.989	0.012	1.845	0.255	0.063	0.246
A181620D1	69.243	1.014	1.128	0.001	1.027	0.046	0.982	0.017	1.726	0.352	0.193	0.419
A181620E1	70.073	0.979	1.129	0.001	1.016	0.041	0.99	0.015	1.871	0.304	0.091	0.346
A181620F1	69.976	1.014	1.134	0.001	1.014	0.043	0.994	0.017	2.013	0.319	0.078	0.395
A181620G1	70.469	1.072	1.121	0.001	1.017	0.045	0.988	0.016	1.681	0.327	0.098	0.346
A181620H1	69.798	0.921	1.114	0.001	1.029	0.041	0.976	0.014	1.403	0.309	0.183	0.312
A221620B1	68.584	3.558	1.122	0.001	1.04	0.187	0.975	0.07	1.411	1.522	0.385	2.182
A221620J2	68.614	3.829	1.132	0.001	1.033	0.185	0.978	0.064	1.731	1.476	0.245	1.694
A221620N1	59.396	1.805	1.203	0.001	1.141	0.168	0.926	0.047	1.43	1.447	1.89	2.181
A221620R1	70.286	1.794	1.138	0.001	1.008	0.073	0.997	0.028	2.139	0.52	0.03	0.617
A221620U1	69.038	2.036	1.146	0.001	1.018	0.092	0.991	0.037	2.214	0.718	0.124	0.942
A221700A1	68.825	2.61	1.12	0.001	1.038	0.124	0.971	0.042	1.411	0.977	0.278	1.078
A221700D1	70.003	1.852	1.125	0.001	1.02	0.078	0.987	0.029	1.74	0.58	0.121	0.653
C221620C1	68.842	1.003	1.134	0.001	1.029	0.046	0.982	0.018	1.833	0.363	0.221	0.467
C221620D1	68.786	1.928	1.127	0.001	1.034	0.091	0.977	0.033	1.616	0.714	0.267	0.887
C221620E1	70.315	1.392	1.12	0.001	1.019	0.058	0.986	0.021	1.655	0.426	0.106	0.452
V221960K1	68.679	2.854	1.099	0.01	1.054	0.139	0.959	0.047	0.782	1.135	0.45	1.273
V221960La	69.966	4.358	1.099	0.01	1.038	0.191	0.97	0.065	1.606	1.468	0.26	1.531
V221960Mc	69.726	3.692	1.099	0.01	1.041	0.165	0.968	0.057	0.949	1.294	0.305	1.385
V221960Na1	68.829	5.558	1.095	0.01	1.056	0.268	0.958	0.091	0.663	2.13	0.477	2.484
A31500D1	68.883	2.996	1.186	0.001	0.997	0.126	1.009	0.051	3.383	0.94	-0.037	1.202
A31500F1	69.695	1.964	1.173	0.001	0.993	0.081	1.013	0.034	3.087	0.598	-0.078	0.814
A31500G1	69.012	1.993	1.185	0.001	0.995	0.084	1.013	0.036	3.371	0.632	-0.069	0.883
A31500H1	69.118	1.524	1.176	0.001	0.999	0.066	1.009	0.028	3.104	0.505	-0.044	0.705
A31500I1	67.904	1.657	1.189	0.001	1.008	0.077	1.005	0.034	3.339	0.619	0.025	0.907
A31500J1	69.557	0.859	1.164	0.001	1	0.036	1.005	0.014	2.828	0.274	-0.016	0.33
A31500K1	69.561	2	1.176	0.001	0.994	0.082	1.012	0.035	3.155	0.603	-0.072	0.807
A31500L1	69.113	1.469	1.175	0.001	1	0.063	1.008	0.027	3.092	0.483	-0.038	0.657
A31500M1	68.871	1.557	1.175	0.001	1.003	0.068	1.004	0.028	3.054	0.528	-0.01	0.696
A31500N1	69.322	1.933	1.186	0.001	0.991	0.079	1.017	0.035	3.396	0.573	-0.101	0.835
A31600A1	70.629	1.135	1.13	0.001	1.009	0.045	0.995	0.017	1.952	0.324	0.031	0.341
A31600B1	69.047	1.188	1.144	0.001	1.019	0.053	0.989	0.02	2.17	0.409	0.124	0.504
A31620H1	68.98	2.104	1.145	0.001	1.02	0.095	0.994	0.04	2.174	0.732	0.147	1.064

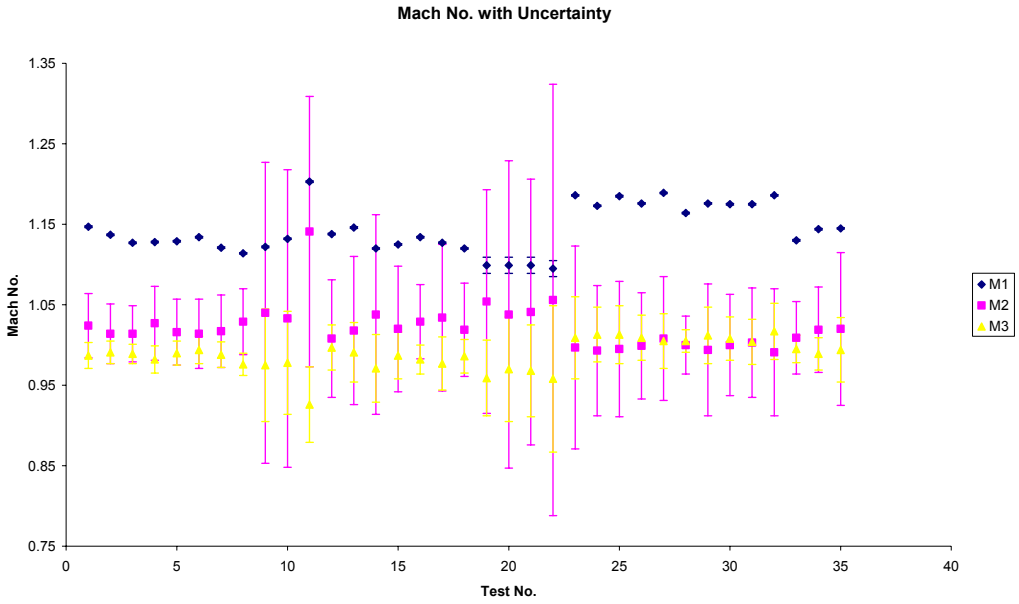


Figure 97: Mach number variations for all burst pressure

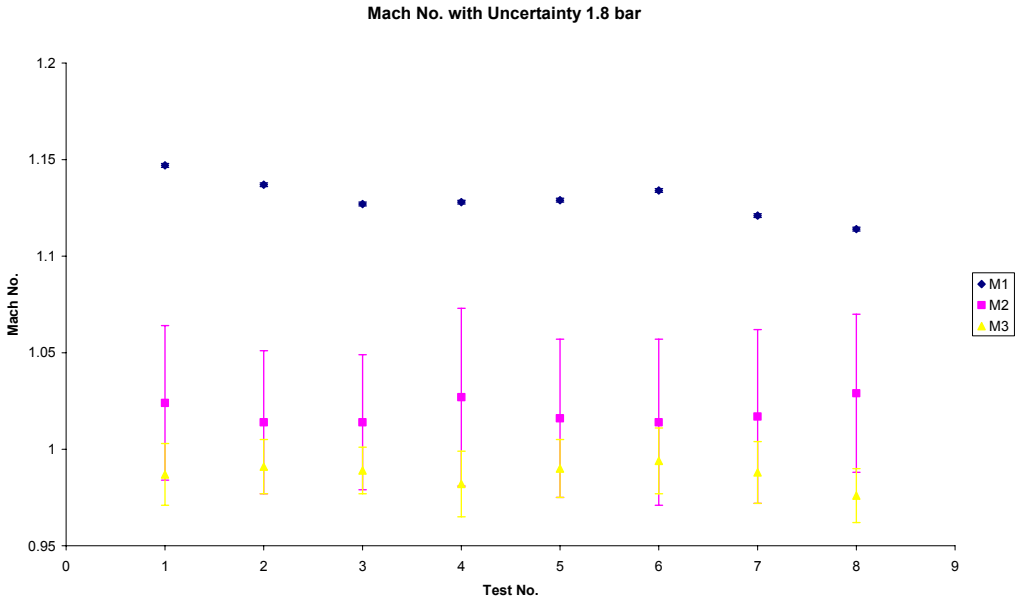


Figure 98: Mach number variations for burst pressure of 1.8 bar

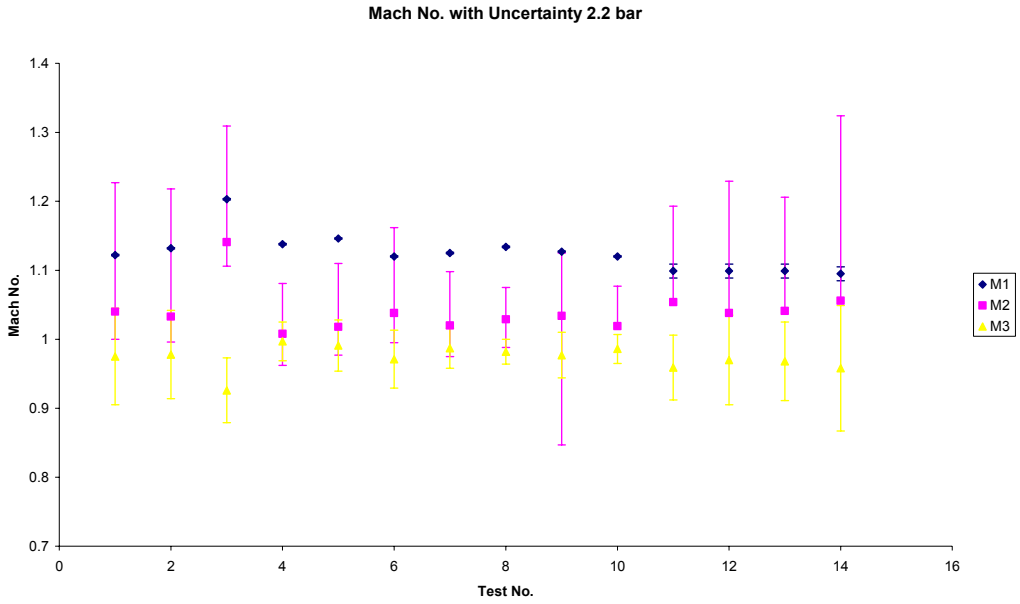


Figure 99: Mach number variations for burst pressure of 2.2 bar

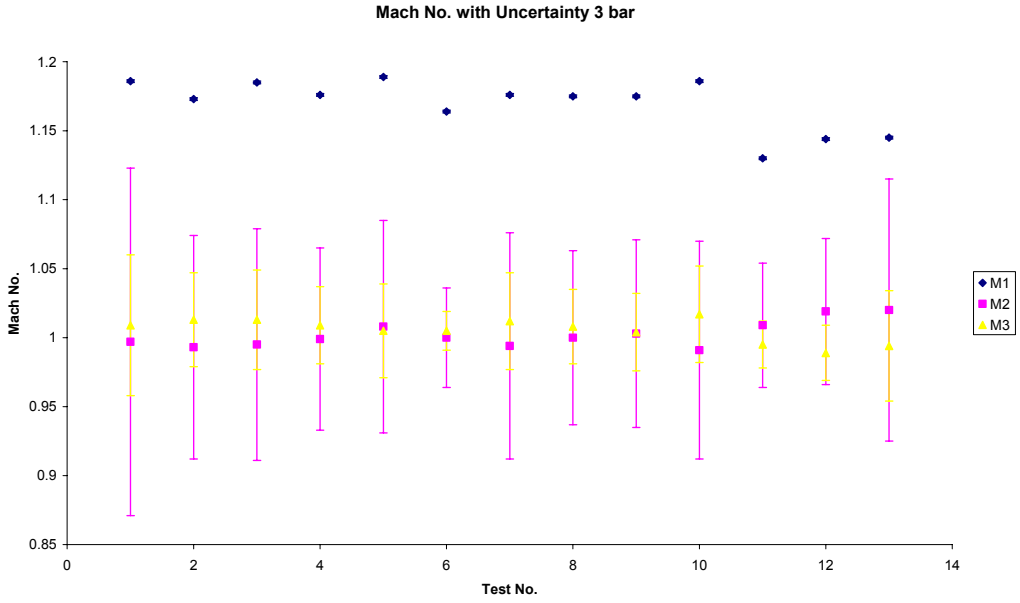


Figure 100: Mach number variations for burst pressure of 3 bar

6.4 Pressure Traces

Pressure traces are used, in this case, only to calculate the speed at which the shock front travelled between the first pressure transducer (channel 1) and the second pressure transducer (channel 2). Since the distance between these transducers was fixed at 50mm, the time between the indications of the arrival of the shock wave front at each transducer could be used to calculate the Mach number (M). A few examples of these pressure traces are shown below in figure 101 to figure 106 in Microsoft® Excel format:

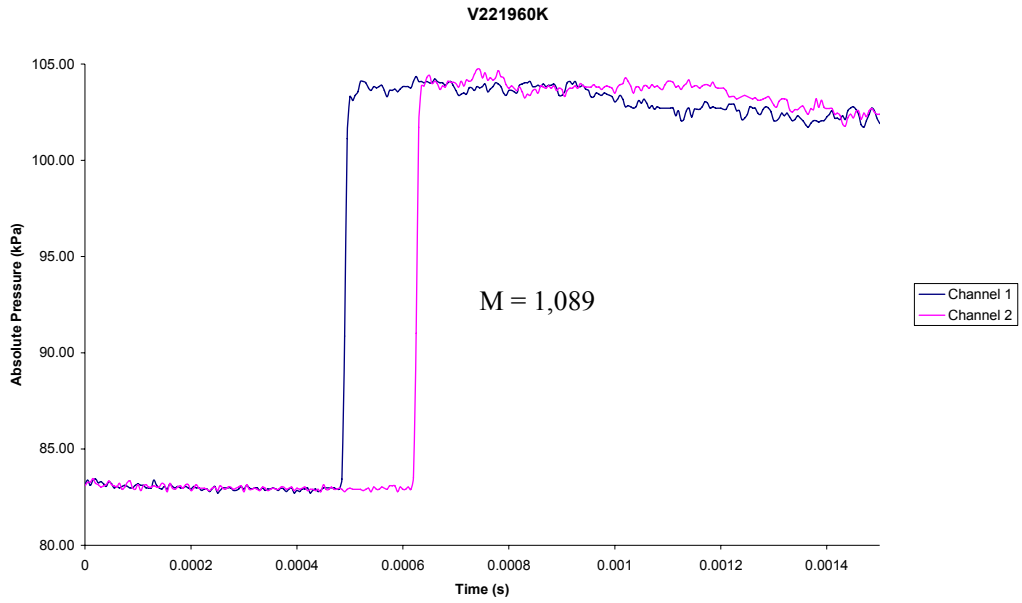


Figure 101: Pressure traces for photograph V221960K

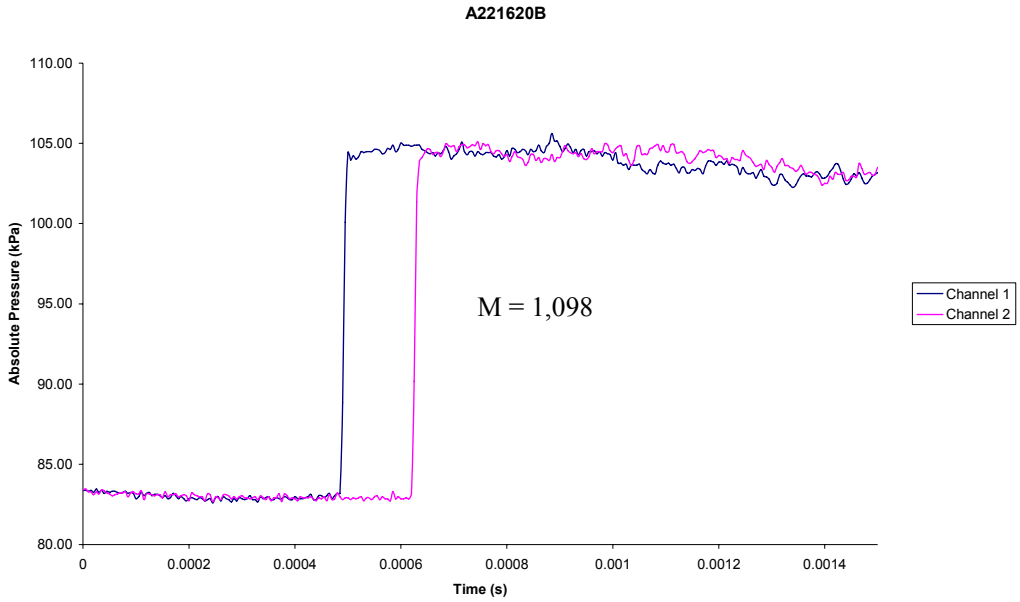


Figure 102: Pressure traces for photograph A221620B

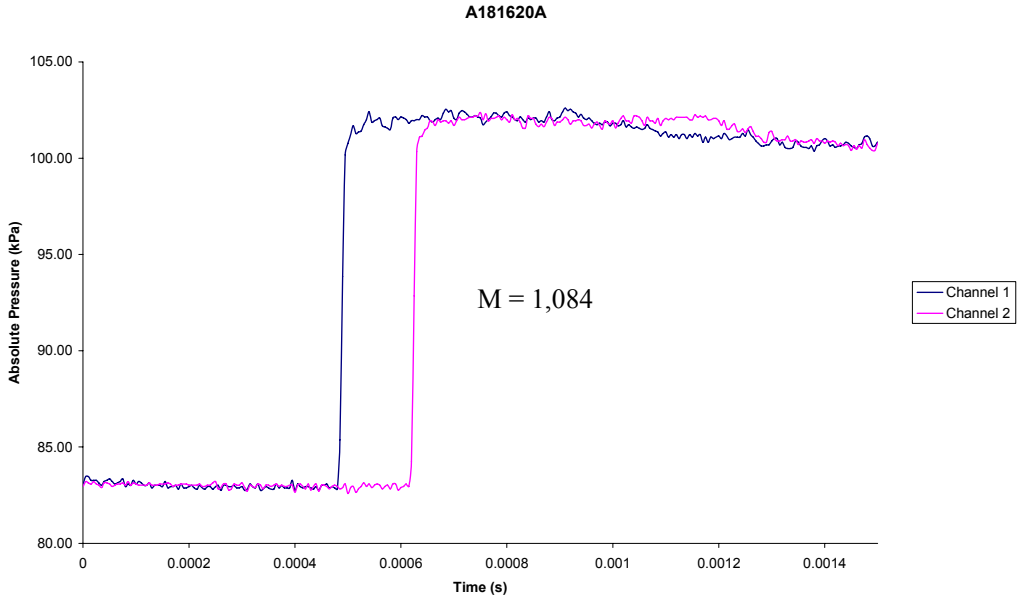


Figure 103: Pressure traces for photograph A181620A

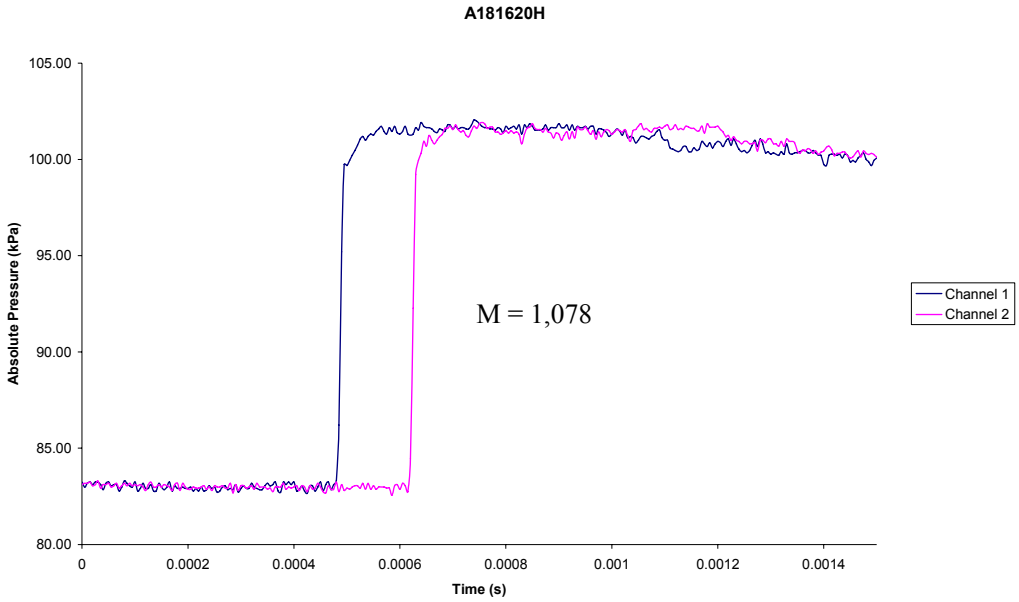


Figure 104: Pressure traces for photograph A181620H

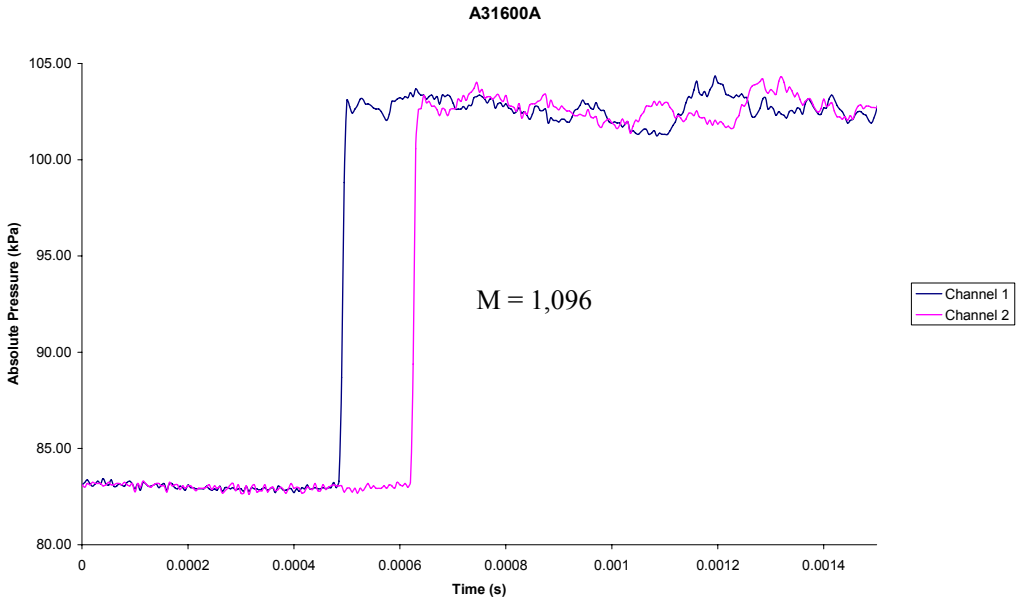


Figure 105: Pressure traces for photograph A31600A

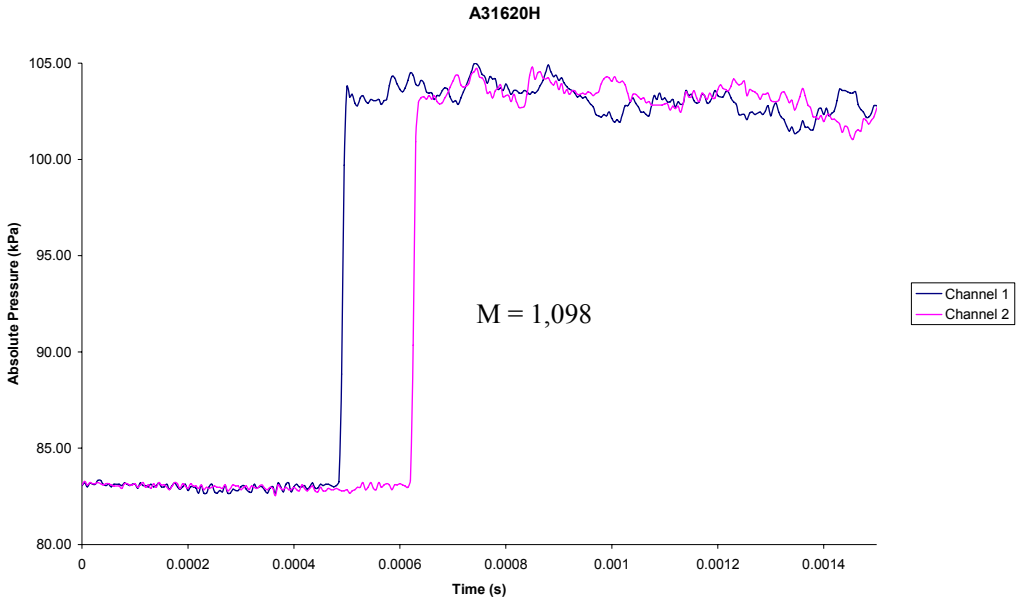


Figure 106: Pressure traces for photograph A31620H

7 Discussion

7.1 Numerical Data

The computational results were used mainly to predict if the triple point would fall into the furthest downstream test section, and window aperture, for a range of angles. If a triple point was evident at that section, without having bounced off the floor of the shock tube, it indicated the possibility of the triple point appearing anywhere upstream. The following figures detail views of figures 38, 42 and 46 from section 6.1:

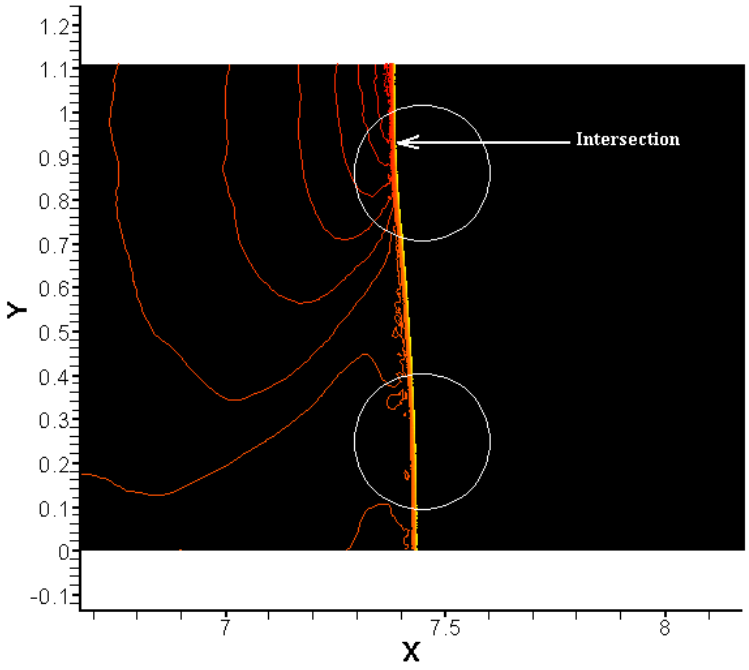


Figure 107: Density contour for 10° ramp with intersection shown.

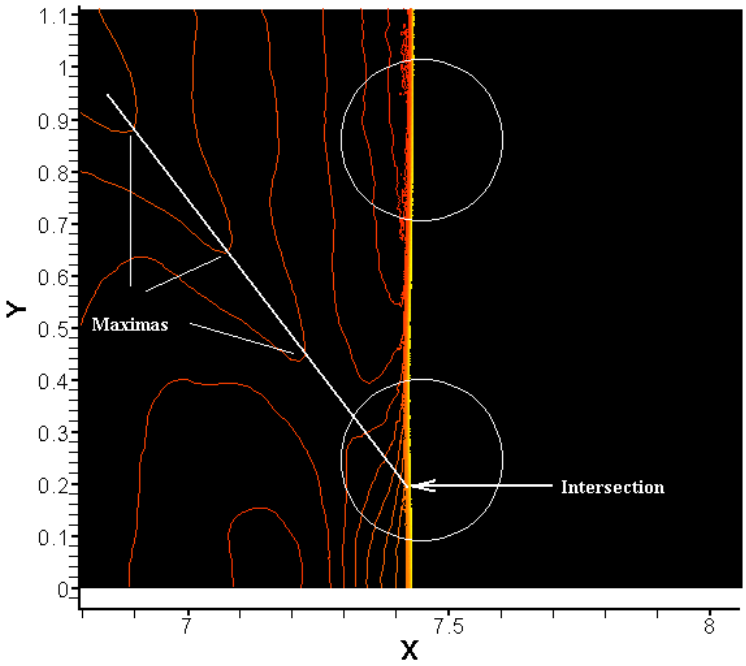


Figure 108: Density contour of 15° ramp with intersection shown.

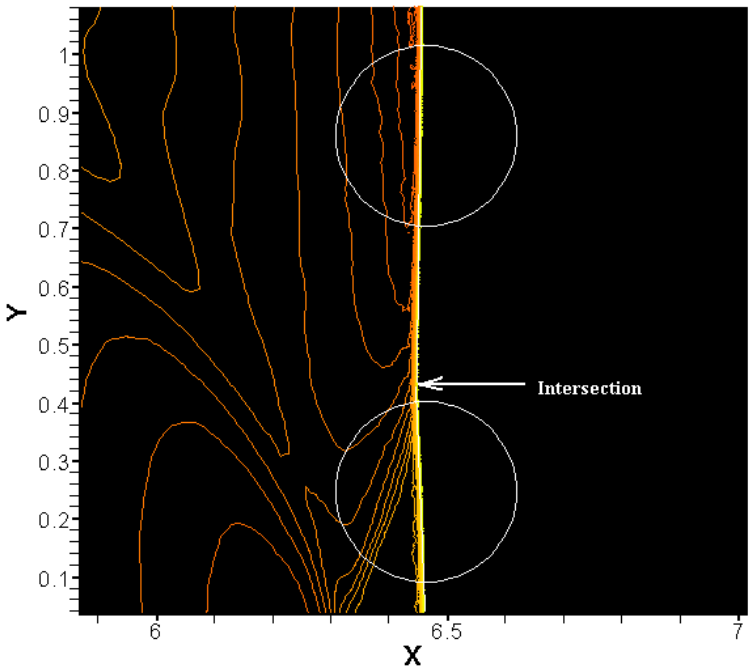


Figure 109: Density contour of 20° ramp with intersection shown.

The intersection point of the incident shock wave and the Mach stem was previously referred to as the triple point. However, due to the low resolution of the simulation, there is no reflected shock wave in any of the pictures. In addition to this problem, the reflected shock wave was shown to be very close to sonic from the oblique shock wave calculations. This makes the reflection shock wave not visible in the low resolution simulation.

There are three ways to find out the location of the intersection from the simulations. The first one is used in figure 107 above, where the intersection is simply at the end of the straight Mach stem. The second one uses a straight line to connect the maxima of the flow behind the shock wave, and the intersection is where the straight line intersects the shock wave shown in figure 108 above. The third method is very similar to the first one, where instead of using only the Mach stem, a straight line is also drawn from the incident shock wave. The intersection is where the two straight lines meet shown in figure 109 above.

The 10° ramp configuration shows the intersection point in the top furthest downstream test section. This means the shock tube has to be longer for the intersection to come down to the bottom test section. This makes the intersection point more developed, i.e. sets of expansion fans and shocklets becomes visible. However, considering the current longest configuration of the shock tube, at least an additional two meters is necessary for the triple point to reach the bottom test section. This is currently impossible due to the length of the shock tube being already 9.5 meters, and the limited room size.

The 15° ramp configuration shows the intersection point in the bottom furthest downstream test section, which correlates to the experimental photographs. This can be shown by comparing the following photograph taken at the furthest downstream bottom test section of the shock tube to the simulation shown in figure 108:

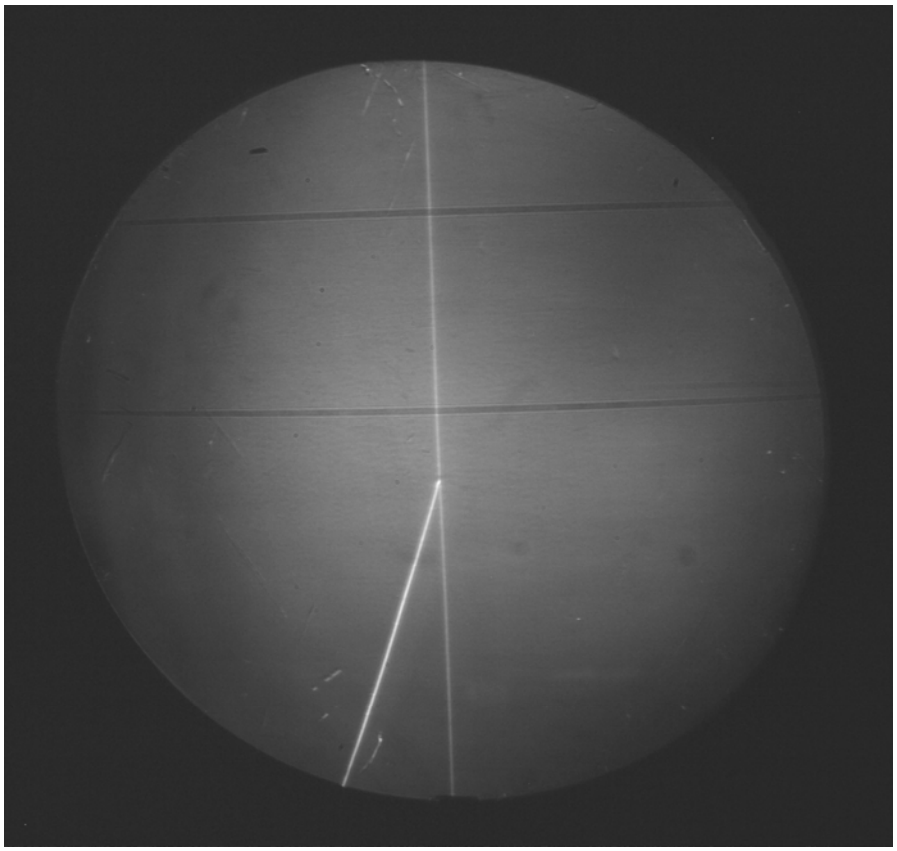


Figure 110: Triple point at the furthest dowstream bottom test section (flipped horizontally).

The 20° ramp configurations shows the intersection inbetween the two test sections at the furthest downstream position. This means the intersection can be visualised by rotating the test section accordingly. This also means the triple point can be visualised anywhere upstream of the current furthest downstream position.

The 20° ramp configuration was chosen to be the best for the application. It is because the triple point develops faster, which means more sets of expansion fans and shocklets will be visible. And this is also shown in the simulations as the reflected shock wave is more visible, thus the reflected shock wave is stronger, and the expansion fans and shocklets are also stronger. Therefore, the 20° ramp was designed for further experimental investigation. The design drawing of the 20° ramp was drawn with Solid Edge®, and these drawings can be found in Appendix C.

7.2 Experimental Data

Most of the photographs taken during the experiments used the schlieren system with the Fujifilm 12 mega-pixel camera. This was due to the high sensitivity needed to visualise the small triple point region with very small gradient changes. Both sets of parabolic mirrors were used for this application. The larger set (12.5 inch) was used for visualisation of the entire test section as primary tests, while the smaller set (4 inch) was used to focus on a smaller area of the test section that showed promising results from the primary tests.

The knife edges were initially set as vertical to obtain the Mach stem and incident shock gradient changes. The knife edges were then turned to 15 degrees inclined to the vertical to maximise the gradient changes of the reflected shock and the sets of compression waves and shocklets behind it. The images produced using this method show the compression waves and the shocklets much clearer than the vertical knife edges. This is because the Mach stem and incident shock are stronger than the compression waves and the shocklets. The Mach stem and the incident wave were visible using any knife edge orientation, but this was not the case for the compression waves and shocklets. It was thus decided to use the inclined knife edge for most of the experiments to better visualise the compression waves and shocklets which were the main focus of the project.

Three main burst pressures were used to produce different incident Mach number shock waves. The pressures used were 1.8, 2.2 and 3 bar gauge. The three corresponding Mach numbers at the test section were, on average, 1.119, 1.140 and 1.174, based on the multi-frame photographs shown in section 7.4 below. Although higher pressures were also used, the triple point in these conditions was found to travel much faster towards the test section as well as towards the floor of the shock tube. Images of the flow produced under these conditions were obtained by taking the middle rectangular section of the expansion chamber out, leaving the test section directly next to the divergent section. However, this shock tube configuration did not allow the triple point to fully develop, and thus the region around the triple point was even smaller than the ones from the full configuration of the shock tube. Therefore, it was decided to use the full shock tube configuration and use lower Mach numbers. In the limiting case, the triple point produced with a 3 bar burst pressure was just visible at the bottom of the test section. It was found that a 2.2 bar burst pressure, which produced a Mach number of 1.140 at the test section, gave the best results. Therefore, most of the tests were conducted at a burst pressure of 2.2 bar.

7.2.1 Single-frame Photographs

Over 400 single-frame photographs were taken for the investigation of the possible sequences of shocklets and expansion fans behind the triple point. Most of them show the possible sign of a compression region (darker area) behind the reflected shock and then a shocklet (brighter area) terminates the compression region. For example: figures 41, 42 and 44 in the results section. However, only a few of the photographs show signs of a possible second set of expansion fans and shocklets. For example figures 43, 48 – 50, 53 and 57 all show very promising signs of the second set. Some of which even have an expansion fans behind the second shocklets. The darkness of this photograph is due to the high sensitivity of the schlieren system, which was only attainable by using the high ISO setting on the Fujifilm camera (ISO 1600). The adjusted photograph is in figure shown below:

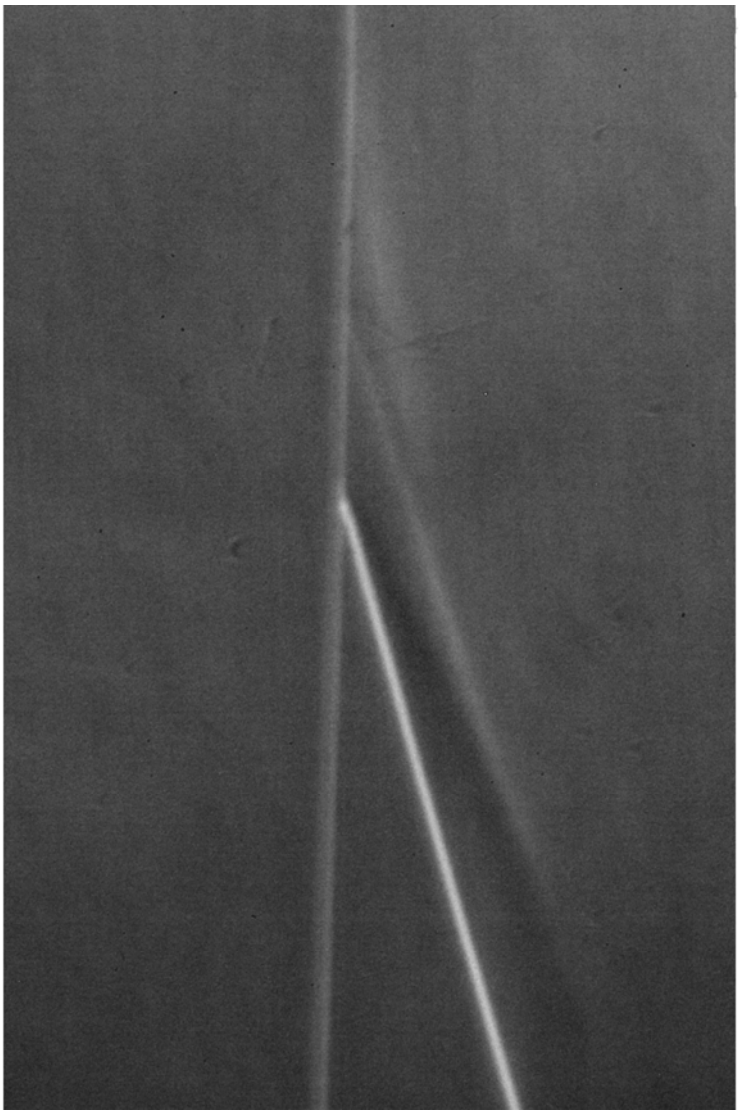


Figure 111: Modified schlieren photograph P221980C

A schematic drawing of the triple point is shown below:

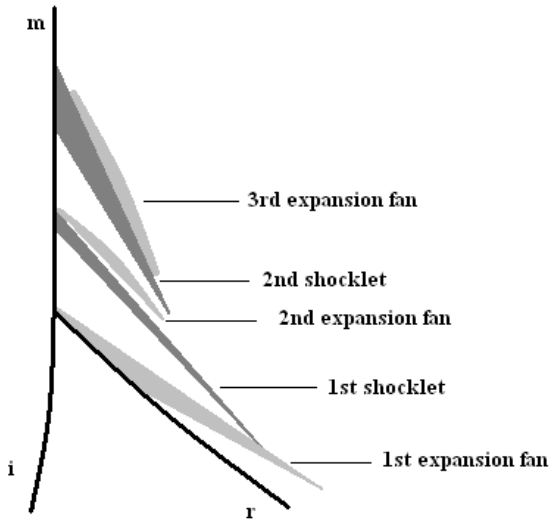


Figure 112: Schematic drawing of photograph P221980C

The first expansion fan is behind the reflected shock (r). It follows with the first shocklet which is slightly higher along the Mach stem (m). This shocklet terminates the first expansion fan and the second expansion fan forms behind this shocklet. The second shocklet is again slightly higher than the first shocklet along the Mach stem and it terminates the second expansion fan. The third expansion fan is above the second shocklet. However, as can be seen in figure 111, the third expansion fan is very weak, and thus subsequent shocklets and expansion fans are very hard to visualise, if not impossible, even using the 1.1 meter high shock tube.

The reason these sets of shocklets and expansion fans weaken so rapidly may be partly due to the viscous effect in air and that they successively decrease in strength and size as Tesdall has shown (figure 5). In theory there should be an infinite sequence of shocklets and expansion fans for an ideal inviscid flow (Tesdall et al., 2002). Furthermore, the shock wave is also very weak (incident M ≈ 1.10). Therefore, the third expansion fan has the lowest strength when compared to the first and second expansion fan.

The schematic drawing above over-emphasises the fact that the incident shock wave does have a finite curvature. In fact, the Mach stem and the reflected shock are also curved. However, in figure 111, all three shocks seem to be planar. This is due to the large scale of the shock tube. The triple point has to travel about three and a half meters from where it was

first developed to the test section. By this time, all these shocks have settled to a very large radius of curvature (but not planar).

The size of the triple point region that was photographed was calculated using the distance between the two guides in the test section. These two guides can be found on photograph N221970B in figure 49 (also shown below as figure 113). The separation was measured accurately by use of a vernier. The distance was 31 mm. The guides in photograph P221980C in figure 111 were taken away to avoid interference with the triple point. But this photograph has the identical size of the photograph N221970C. Therefore, the triple point region generated by this shock tube was just less than 31 mm high. The shock tube inner height is 1105 mm, and the centre of the test section is 246 mm from the bottom. This means, for the triple point at the centre of the test section, the Mach stem is about 859 mm long. Thus, the triple point region is only about 3.6 % of the Mach stem height in size.

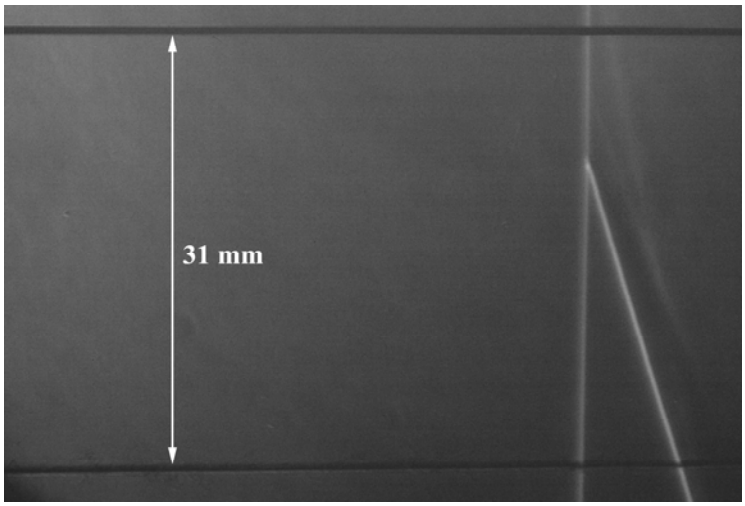


Figure 113: Schlieren photograph N221970B with measurement

Further analysis of some photographs are included in the submitted journal paper and are reproduced below. In figure 114, the darker areas in the original picture are delineated to show as white in the processed picture. The lighter areas in the original, and particularly the shocks, are shown as black in the processed picture. The white area behind the reflected shock is the first expansion wave. The black area behind the first expansion wave is the first supersonic patch and it is terminated by a shock wave behind it as the white area. In figure 115, contours are simply drawn around all lighter areas of a given intensity value so as to highlight all the shock waves. The reflected shock wave and the first shocklet are clearly visible with two dark patches behind the first shocklet. This indicates the possible second shocklet behind the first shocklet.

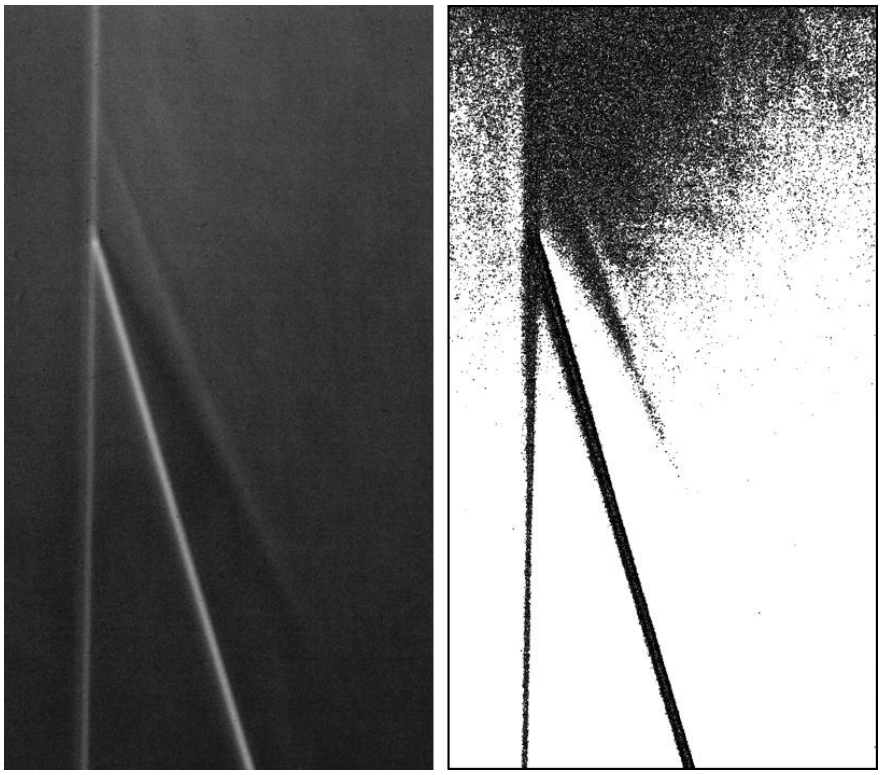


Figure 114: Original and processed image to highlight expansion waves of photograph O221970D (Skews et al., 2008)

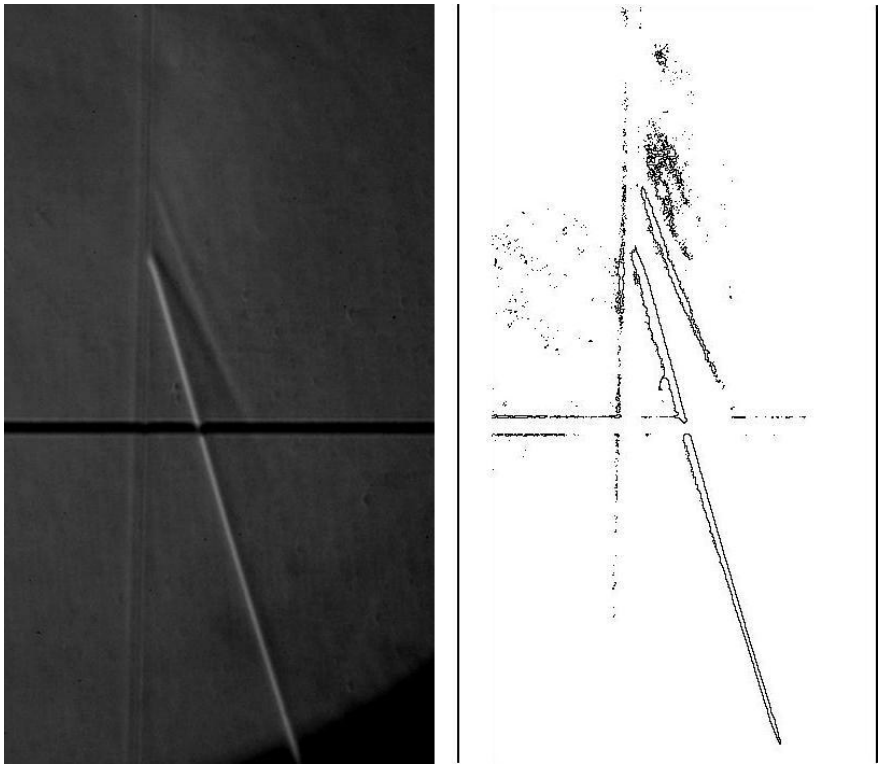


Figure 115: Original and processed image to highlight shock waves of photograph L221900A (Skews et al., 2008)

7.2.2 Multiple-frame Photographs

The multiple-frame photographs were captured by the Cooke million-frame per second camera. Although the camera offers very low resolution (about 0.08 mega-pixel quality) it is still capable of capturing the weak shock waves. And in some cases, the first shocklet was also visible. This is due to the very bright 650W lamp and the very high sensitivity schlieren system used for the million-frame per second camera. The following photograph is one of the best in all the experiments, which shows quite clearly the first shocklet as a short dark line behind the reflected shock:

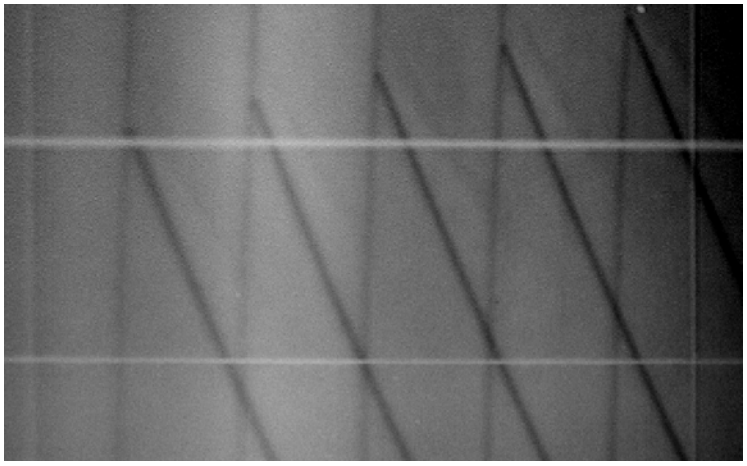


Figure 116: Photograph V221960K (modified)

The main purpose of the multiple-frame photographs was to use the distances and angles between the waves to calculate the Mach numbers in the regions between them. Many of the photographs were taken for three different burst pressure, namely 1.8, 2.2 and 3 bar (gauge), which were the same pressures as for the single-frame photograph. Higher pressures were also considered for this application, but it was decided not to conduct experiments at these pressures due to the triple point not being fully developed at higher Mach number with the shorter shock tube configuration.

The basic requirements of these photographs were quite simple; they had to be clear enough for measurements and must show the triple point near the guides in the test section. The clarity of the photograph reduces the error in the calculations when measuring between waves (this will be further discussed in section 7.4 below). Also, if the triple points were too far away from the guides, it increased the possible error in the calculations due to the scaling factor from the distance of the guides.

The photographs were first taken with five exposures, thus each photograph would have five triple points with a known delay time between them. It was first thought that the higher the number of triple points in the photograph, the more accurate the calculations would become. However, as shown in the section 7.4 below, the variations between the triple points increased as the number of exposure increased. This was due to the fact that the trajectory of the triple point from the corner where it was first developed is not linear. However, the curvature of this trajectory is very small, and thus it was deemed reasonable to assume the trajectory was linear to make the calculations simpler. This means the number of triple point does not increase the accuracy of the calculation, rather the larger distance between the triple point increases the accuracy of the calculation. Therefore, after a few sets of the five triple points photograph experiments, it was decided to use three triple points, since two triple points do not provide enough information for the calculations. It was also decided to use the biggest area possible within the test section to increase the distance between the triple points. This further reduces the effect of measurement errors as the error is the same for both the smaller region and the bigger region in the photograph.

7.3 Contact Shadowgraph Photography

Although the shadowgraph system does not provide high sensitivity as compared to the schlieren system, it was still decided to conduct experiments with the contact shadowgraph system. Unfortunately, after a set of photographs was taken, only a single photograph clearly showed the triple point region. This was due to the size of the sensor of the Fujifilm camera used. The sensor is only 23 mm by 15.5 mm in size, while the triple point region is about 30 mm long (as estimated in section 7.2.1). Also the height of the triple point in the shock tube varies considerably, mainly due to the large scale of the shock tube, the variations of the pressure supply in the laboratory and the compression rate of the compression chamber due to the inlet valve. Therefore, it is very hard to maintain identical conditions for every test, and thus very difficult to capture the triple point using the small camera sensor. However, the consistency of the shock wave is very good. This means there is always a shock wave in the photograph with no triple point. Additional to this problem, the single successful photograph shows no sign of any waves behind the triple point, whereas the photographs by the schlieren system show at least one expansion fan and one shocklet behind the triple point. This is due to the low sensitivity characteristic of contact shadowgraph system. Thus the author did not continue to conduct contact shadowgraph experiments.

7.4 Oblique Shock Wave Calculations (Primary)

The oblique shock wave calculations were done based on measuring the modified million-frame per second photographs in Microsoft® Paint as mentioned before. However, at the outset of the calculations, it was thought that using a vernier to measure from a print out of the photograph would provide satisfactory results. But it was found that due to large measurement errors (shown in table 3 to table 5), the variations of the Mach number and the deflection angles were unacceptable. Thus this method was deemed unacceptable for this application.

Microsoft® Paint allows the user to obtain coordinates of points required on the shock waves. Once the coordinates are known, by subtracting them between different points, the distances between the points are known. This then leads to the calculations of velocity of respective shock waves. This method, however, does contain some measurement errors. For example, because some of the shock waves have a finite curvature due to the shape of the shock tube, it is hard to choose two random points on the curve to approximate it as a straight line. In other words, the longer the distance between the two chosen points, the bigger the gap between the straight line and the curve. This method is shown in figure 88 with lines drawn between the shock waves.

A problem in the calculations was that all shock wave images have a finite thickness due to the finite exposure time of the light source. Although the light source exposure time was about 2μs, the shock wave is travelling fast in a small area resulting from the optical magnification. Thus the finite thickness problem of the shock wave is unavoidable. There are two ways to compensate for this; either by decreasing the exposure time of the light, or increasing the size of the photograph. The light source exposure time was unable to change in this case due to the light sensitivity of the million-frame per second camera. Therefore, the only way was to increase the size of the photograph by using the 12.5 inch parabolic mirrors. However, by increasing the size of the photograph, the lengths of the shock waves were also increased, which led to the increase in curvature of the shock waves. Therefore, the use of the full test section also increased the measurement error. Thus, intermediate size photographs were taken. This was done by using a weaker lens (i.e. lenses with less curvature, which means longer focal length) to focus the image onto the camera. This effectively zoomed into the test section, imaging a smaller area. This optical system was the best for the million-frame per second photographs, as just enough light goes into the sensor of the camera.

All results can be found in section 6.3.2 above. Table 7, figure 117 and figure 118 below shows the average of the good results (the average of 1&3 and/or 1&5 in section 6.3.2):

Table 7: Average for good results

P (bar)	β (deg)	d (mm)	t (s)	M1	M2	M3	θ1 (deg)	θ2 (deg)
1.8	18.02	114.19	0.00030	1.119	1.0026	0.9988	1.781	0.011098
2.2	17.89	77.93	0.00020	1.140	1.0011	1.0040	2.255	-0.008754
3	19.24	119.66	0.00030	1.174	0.9930	1.0141	3.119	-0.112196

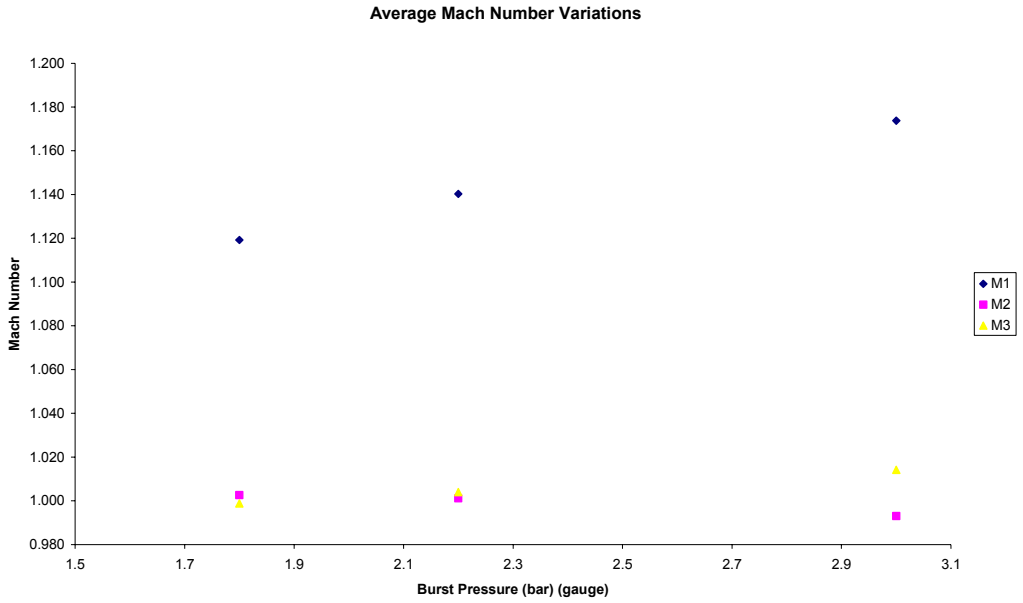


Figure 117: Average Mach Number Variations

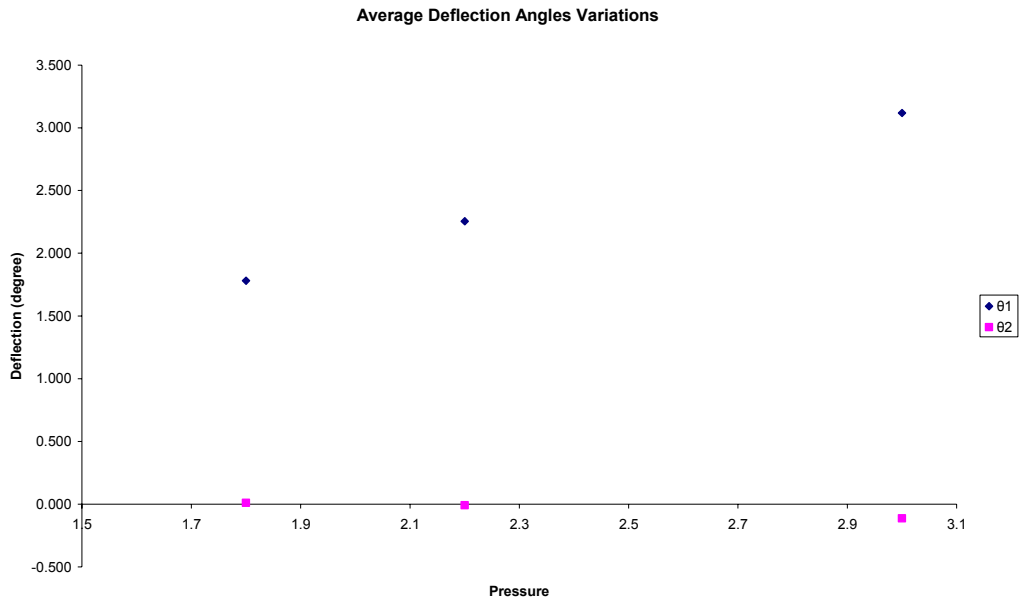


Figure 118: Average deflection angles variations

Experiments conducted with a burst pressure of 1.8 bar showed the best results because M_3 was subsonic due to the lower Mach number of M_1 as compared to other burst pressures. For a lower M_1, M_2 was slightly higher, making it just above sonic. That means M_3 would most probably be subsonic. However, for the case of a burst pressure of 3 bar, M_1 was the highest as compared to the other burst pressures, while M_2 just goes below sonic. Based on the oblique shock wave equations, M_3 would then be supersonic again, which is not physically possible. A flow cannot return to supersonic again after it has become subsonic across a shock without any additional energy being added into the flow or the area of the flow being changed. This is due to the assumption of the shock wave being plane in the oblique shock calculation. However, the physical shock wave is actually a curve with a very large radius.

However, some of the 3 bar burst pressure results did agree with the theory, for example, tests A31600A and A31600H in table 5 above. As for the burst pressure of 2.2 bar, some results such as V221960L in table 4 above did not agree with the theory but most of them agree fairly well. There was a similar trend for the deflection angle results, where θ_1 was acceptable, but some of the θ_2 values were negative. This means the flow is turning towards the reflected shock as an expansion wave, which is also physically not possible. This is due to the same problem as discovered when using the oblique shock theory to calculate Mach number.

7.5 Oblique Shock Wave Calculations (Secondary)

The secondary calculation was conducted using a more accurate measurement system as mentioned before to overcome the measurement error and the optical distortion with the new machined grids and the two stage spline method. It proven to give better results then the primary calculations with the only inconsistency in the 3 bar tests. The table below shows the averages of all the tests performed by the Matlab code:

Table 8: Average for secondary calculations

P (bar)	β (deg)	M1	M2	M3	θ1 (deg)	θ2 (deg)
1.8	69.78438	1.129625	1.019375	0.987125	1.848375	0.121625
2.2	68.5635	1.125643	1.040643	0.973214	1.512857	0.3685
3	69.20708	1.169538	1.002154	1.005615	2.931154	-0.01062

The inconsistency in the 3 bar tests are due to the assumption of the shock wave being plane in the oblique shock calculations. However, the physical shock wave is not a plane wave and has a finite curvature. M2 and M3 for all cases are very close to sonic for these weak shock reflections.

This shows, even with a more accurate measurement system and an improved calculation method, the oblique shock calculation with the assumption of plane shock wave is not appropriate for the triple point calculations particularly for stronger shocks. These problems are primarily due to the weakness of the reflected wave and thus significantly higher measurement accuracies are needed. Nanosecond light pulses maybe required together with very high quality optical components.

7.6 Pressure Traces

The pressure traces were only used to determine the time between the shock wave arrival at channel 1 and channel 2 in order to confirm M_1. However, due to the low gauge pressure obtained from the oscilloscope, it was decided to determine the pressure ratio across the shock wave to check for possible error. The pressure ratio was used to compare to the normal shock table from the text book of Skews (2001). The chosen test to be analysed below is V221960K. A pressure ratio plot is shown below:

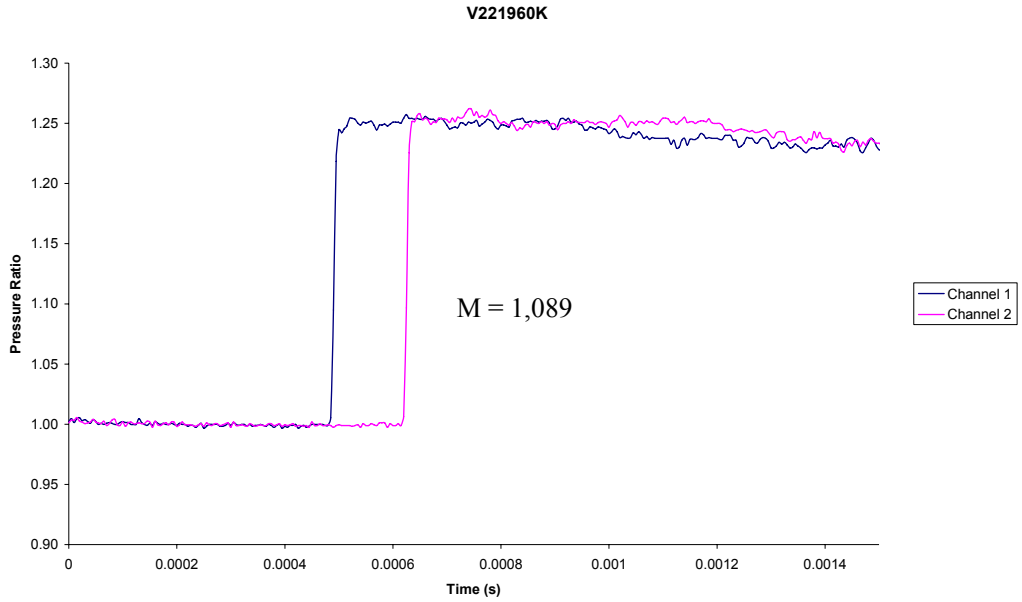


Figure 119: Pressure ratio across the shock wave for test V221960K

It was shown above that the highest pressure ratio across the shock wave was about 1.26. The next step was to obtain the Mach number across the shock wave, which was shown on the figure above as M = 1.089. By using this Mach number in the normal shock tables, and with linear interpolation, it was found that the pressure ratio should be 1.217. The difference between the theoretical and experimental results is only 3.533%, which is considered small.

The Mach number of the test, according to the pressure transducers, was 1.089. However, the two pressure transducers were measuring the pressure changes in the Mach stem region, and not at the triple point. Thus the Mach number must be divided by the cosine of the angle of the triple point trajectory with respect to the horizontal line to obtain the triple point Mach number. This angle is approximately 21.44 degrees for the test V221960K obtained by the photograph in Microsoft® Paint. Therefore, the Mach number of the triple point is 1.170. The Mach number of the triple point from the photograph was calculated to be at $M_1 = 1.145$ as shown in table 4 in the results section. Therefore, the two Mach numbers are very close to each other with about 2.183 % difference. This small difference is due to the finite distance between the test section and the pressure transducers' ports. The distance is about 900 mm from the centre of the test section to channel 2 shown in figure 24 in the apparatus section. The triple point must have weakened slightly by the time it got to the test section from 900 mm upstream. Therefore the 2.183 % difference is realistic. Although the pressure ratio does not agree with the theory, the measurement for the Mach number is considered very accurate.

8 Conclusion

The weak shock reflection phenomena has been extensively investigated to gain more understanding of the von Neumann reflection (vNR) and the Guderley reflection (GR) with the following conclusions:

8.1 CFD Investigation

- Different values of ramp angles, ranging from 8 to 25 degrees, were conducted with coarse mesh simulations.
- Three angles were chosen to be further investigated, namely 10, 15 and 20 degrees, with a refined mesh.
- The simulation results of the 15 degree ramp correlated with the experimental results.
- The 10 degree ramp was not suitable for the Blue shock tube due to the length of the test section required, and also because the triple point is not as well developed as for the other ramp angles.
- The 20 degree ramp was chosen to be the best due to the fast development of the triple point.
- The 20 degree ramp was designed by the use of Solid Edge®.

8.2 Schlieren Photographs

- Three different Mach numbers were employed for these experiments.
- Most of the schlieren photographs were satisfactory with high sensitivity.
- Most single-frame photographs show the existence of the first set of expansion fan and shocklets.
- Some of the single-frame photographs indicate the existence of a second set of expansion fan and shocklet. This gives major credence to the Tesdall (Tesdall et al., 2002) simulations.

- The existence of the third expansion fan in some of the single-frame photographs is not clearly visible, while no sign of the third shocklet is shown in any of the photographs.
- Most of the multiple-frame photographs were useful for oblique shock calculations, some of which even showed the first shocklet.

8.3 Contact Shadowgraph Photograph

- Only one photograph was obtained with the triple point due to the lack of repeatability of the contact shadowgraph.
- No sign of any waves behind the reflected shock wave resulted due to the low sensitivity.
- Contact shadowgraphy is not suitable for this application.

8.4 Oblique Shock Wave Calculations

- The oblique shock theory is best correlated in the lower burst pressure experiments (i.e. 1.8 and 2.2 bar)
- The oblique shock calculations showed no physical meaning for most of the high burst pressure experiments (i.e. 3 bar), although some of them agreed well with theory.
- The inconsistency of the 3 bar pressure calculation is due to the assumption of the shock wave being plane in the oblique shock calculations, whereas the shock waves have a finite curvature.
- In all cases exceptionally high measurement accuracy and sensitivity is required because of the weakness of the reflected wave.

8.5 Pressure Traces

- The pressure traces are satisfactory for the Mach number calculation.

9 Recommendations

9.1 CFD Investigation

- Higher resolution simulations must be done to visualise the sets of expansion fans and shocklets behind the reflected shock wave. These will require super computer facilities because of the small size of the region of interest and the need to cover the whole perturbed flow field as evidenced by Vasilev and Tesdall's work.

9.2 Photographic System

- Higher sensitivity schlieren system and a larger facility are needed for the detection of the third set (possibly other sets) of expansion fans and shocklets behind the reflected shock, if they exist.
- Circular knife edge schlieren system for multi-directional sensitivity.
- Higher resolution million-frame per second camera to further reduce the error from measurements of oblique shock calculations.

9.3 Oblique Shock Calculations

- An improved shock calculation theory is needed for weak shock reflection with a finite wave curvature.
- A better measurement system will further improve the accuracy of the shock calculations.

9.4 Blue Shock Tube

- A pressure regulator must be added to control the pressure from the supply line.
- A smaller reading gauge with more divisions should be used at lower burst pressure.

10 References

Ben-Dor G., *A reconsideration of the three-shock theory for a pseudo-steady Mach reflection*, J. Fluid Mech., vol. 181, 467-484, 1987.

Ben-Dor G., *A state-of-the-knowledge review on the pseudo-steady shock-wave reflections and their transition criteria*, Shock Waves, vol. 15, 277-294, 2006.

Bleakney W. et al., *Interaction of shock waves*, Rev. Mod. Phys., vol. 21, 584-605, 1949.

Colella P. et al., *The von Neumann paradox for diffraction of weak shock waves*, J. Fluid Mech., vol. 213, 71-94, 1989.

Guderley K. G., *The theory of transonic flow*, Pergamon Press, 144-149, 1962.

Henderson L. F. et al., *Experiments on the diffraction of weak blast waves: The von Neumann paradox*, Proc. Roy. Soc. London. A., vol. 369, 537-555, 1980.

Hunter J. K. et al., *Weak shock reflection*, J. Fluid Mech., vol. 410, 235-261, 2000.

Hunter J. K. et al., *Transonic solutions for the Mach reflection of weak shocks*, Proceedings of Symposium Transsonicum IV, Göttingen, 2002.

Kobayashi S. et al., *Examination of the von Neumann paradox for weak shock wave*, Fluid Dyn. Res., vol. 17, 13-25, 1995.

Kobayashi S. et al., *Non-self-similar characteristics of weak Mach reflection: the von Neumann paradox*, Fluid Dyn. Res., vol. 35, 275-286, 2004.

Kodak, *Schlieren photography*, Kodak Scientific and Technical Data, Eastman Kodak Company, 1960.

Felthun L. T., *Finite element analysis of compressible flows*, Thesis (M.Sc. (Eng)), University of the Witwatersrand, 1995.

Sakurai A., *On the problem of weak Mach reflection*, J. Phys. Soc. Japan, vol. 19, 1440-1450, 1964.

Sakurai A., *Modification of the Neumann condition of weak shock reflection*, 5th Mach Reflection Symp., USA, 1985.

Sakurai A. et al., *On the von Neumann paradox of weak Mach reflection*, Fluid Dyn. Res., vol. 4, 333-345, 1989.

Skews B. W., *The flow in the vicinity of a three-shock intersection*, C.A.S.I. Transactions, vol. 4, No. 2, 98-107, 1971.

Skews B. W., *Course Notes – Compressible Flow*, School of Mechanical Engineering, University of the Witwatersrand, Johannesburg, 2001.

Skews B. W. et al., *The physical nature of weak shock reflection*, J. Fluid Mech., Vol. 542, 105-114, 2006

Skews B. W. et al., *Experiments on Guderley reflection*, J. Shock Wave, 2008, Under renew.

Tesdall A. M. et al., *Self-similar solutions for weak shock reflection*, Siam. J. Appl. Math., vol. 63, 42-61, 2002.

Vasilev E. I. et al., *Numerical solutions of weak shock diffraction over a wedge under the von Neumann paradox conditions*, Comp. Maths. & Maths. Phys., vol. 39, 1335-1345, 1999.

Vasilev E. I. et al., *Analytical reconsideration of the so-called von Neumann paradox in the reflection of a shock wave over a wedge*, ISSW26, Göttingen, 2007.

Walenta Z. A., *Formation of the Mach-type reflection of shock waves*, Arch. Mech., vol. 35, 187-196, 1983.

Zakharian A. et al., *The von Neumann paradox in weak shock reflection*, J. Fluid Mech., vol. 422, 193-205, 2000.

Appendix A – CFD

The Luke's code (Felthun, 1995) given below are the conditions set in the C++ program for 15 degree ramp, $M_1 \approx 1.10$ and $P_{ATM} = 0.83$ bar within the refined simulation.

```
void Gavin(void)
{

        EulerDomain s(100000);

        //SET UP GEOMETRY

        double dr = 3.14159/180;
        double l = 1.105;
        double thi = 15.0*dr;
//      double mw = 3.0;
        double ms = 1.32;
//      double lamb = 3.5, ms=sqrt((5.0)*lamb/(6-lamb));
                                                        // lambda
        double lamb = 6*ms*ms/(ms*ms+5);

//      char name[20] = "fL30a0t135_";                  // Output file name
        char name[20] = "Gavin15deg_";
        bool visFlag = true;                            // Flow Vis output
//      bool visFlag = false;                           // No Flow Vis output

        Point p[20];

        p[1].set(-1.5*l, 0.1*l);
        p[2].set(p[1].coord[1]+1.8*l, p[1].coord[2]);
        p[3].set(p[2].coord[1]+(0.905*(l/tan(thi))), p[2].coord[2]+0.905*l);
        p[4].set(p[3].coord[1]+4.0*l, p[3].coord[2]);
        p[5].set(p[4].coord[1], 0.0);
        p[6].set(p[1].coord[1], 0.0);

        ECurve curve1(&p[6], &p[1]);        curve1.bCode[0] = 3;        //inlet boundary
        ECurve curve2(&p[1], &p[2]);        curve2.bCode[0] = 1;
        ECurve curve3(&p[2], &p[3]);        curve3.bCode[0] = 1;
        ECurve curve4(&p[3], &p[4]);        curve4.bCode[0] = 1;
        ECurve curve5(&p[4], &p[5]);        curve5.bCode[0] = 2;        //exit boundary
        ECurve curve6(&p[5], &p[6]);        curve6.bCode[0] = 1;

        s.mesh(l/6.0, 6, &curve1, &curve2, &curve3, &curve4, &curve5, &curve6);

        //SET INITIAL CONDITIONS

        s.gamma = 1.4;
        double rho = 1.22;
        double pr = 83000.0;
        double u = 0;
        double v = 0;
        double e = pr/(rho*(s.gamma-1));
        s.initialConditions(rho, u, v, e);
        s.fs.rho = rho;
        s.fs.u = u;
        s.fs.v = v;
```

```
        s.fs.e = e;

        s.outputData(name, "i");

        double deltaOut = 0.0001;
        double nextOut = deltaOut;
        int lastout = 0;
        s.hMax = l/56.0;
        s.hMin = s.hMax/8.0;

        int stepNo = 0;
        bool sFlag = false;
        double time = 0.0;
        double cfl = 0.04;
        s.constructEdges();

        double pratio = (6*lamb-1)/(6-lamb);
        double ar = sqrt((lamb*(6-lamb))/(6*lamb-1));
        double mss = sqrt(5)*(lamb-1)/sqrt(6*lamb-1);

        curve1.bCode[0] = 3;
        curve1.bCode[1] = lamb*rho;
        curve1.bCode[2] = mss*340.32/ar;
        curve1.bCode[3] = 0;
        curve1.bCode[4] = pratio*pr/(lamb*rho*(s.gamma-1))+0.5*pow(mss/ar*340.32,2);

        while (time <= 0.035 )

        {
                stepNo++;
                if (stepNo > 200) cfl = 0.2;
                if (stepNo > 400) cfl = 0.6;
                s.deltaT(cfl, ms*340.34);

                cout << "stepno = " << stepNo << " time = " << time << " " << "\n";
                cout.flush();

                if (stepNo/5 == stepNo/5.0)
                {
                        s.adaptMesh(0.015, 4, 2);
                }

                s.moveMesh();
                s.fvmcfd();
                time = time + s.dt;

/*              if ( time > 0.0024)
                {
                        curve1.bCode[0] = 2;
                }

*/              if (time >= nextOut)
                {
                        char  buffer[10];
                        lastout++;
                        itoa(lastout, buffer, 10);
                        s.outputData(name, buffer);
/*                      if (visFlag == true)
                        {
                                s.outputData2(ms, name, buffer);
                        }
*/
                        nextOut += deltaOut;
                }

        }

}
```

Appendix B – EES and Matlab Calculations

The EES program code for test number V221960K is given below:

```
M_2^2*(sin(beta_1-theta_1))^2 = (2/(gamma-
1)+M_1^2*(sin(beta_1))^2)/((2*gamma/(gamma-1)*M_1^2*(sin(beta_1))^2-1))

tan (theta_1) = 2/tan(beta_1)*(M_1^2*(sin(beta_1))^2-
1)/(2+M_1^2*(gamma+cos(2*beta_1)))

M_3^2*(sin(beta_2-theta_2))^2 = (2/(gamma-
1)+M_2^2*(sin(beta_2))^2)/((2*gamma/(gamma-1)*M_2^2*(sin(beta_2))^2-1))

tan (theta_2) = 2/tan(beta_2)*(M_2^2*(sin(beta_2))^2-
1)/(2+M_2^2*(gamma+cos(2*beta_2)))

a = (gamma*R*T_avg)^0.5

V_1 = d_1/t_1

M_1 = V_1/a

gamma = 1.4

T_avg = 14.6 +273

P = 837.7

R = 287

d_1 = d/1000

beta_1 = 90-21.44

beta_2 = 90+beta-21.44-theta_1
```

The Matlab program code is given below:

```
function X = TriplePoint

i = 1;
j = 1;
tpnumvalid = 0;

gamma = 1.4;    %Specific heat ratio for an ideal gas
R = 287.1;      %Gas constant for ideal Air [J.(kg.K)^-1]

[file,path] = uigetfile('Please specify the script with the image
data you wish to process','Image Data File');
while tpnumvalid == 0
    tpnumcell = inputdlg('How many triple points are detailed in each
image?','Number of Triple Points');
    tpnum = str2num(tpnumcell{1});
    tpnumvalid = mod(tpnum,floor(tpnum)) == 0 && tpnum > 0;
end
run(strcat(path,file));
[a,b] = size(X);

X = CoordTrans(X);

while i <= b
    TP = 1:1:tpnum;
    IWP = tpnum+1:2:3.*tpnum-1;
    RWP = tpnum+2:2:3.*tpnum;

    T = X(i).T + 273.15;      %Air temperature [K];
    t = X(i).t;     %Total time between exposure temporal centre
points [s]
    x = X(i).xtrue;     %Retrieves x co-ordinates from structure
array
    y = X(i).ytrue;     %Retrieves y co-ordinates from structure
array

    a = sqrt(gamma.*R.*T);       %Sound speed [m.s^-1]

    %Global geometric calculations
    alpha = atan((y(TP(tpnum)) - y(TP(1))./(x(TP(tpnum)) -
x(TP(1))));       %Angle of triple point trajectory

    %Uncertainty analysis structue array formatting
    Z.gamma = gamma;
    Z.R = R;
    Z.T = T;
    Z.t = t;
    Z.x = x;
    Z.y = y;
    Z.a = a;
    Z.alpha = alpha;
    Z.TP = TP;
    Z.IWP = IWP;
    Z.RWP = RWP;

    while j <= tpnum
        %Global geometric calculations
```

```
        beta1 = atan((x(TP(j)) - x(IWP(j))./(y(TP(j)) - y(IWP(j))));
%Angle between incident wave and vertical
        beta2 = atan((x(RWP(j)) - x(TP(j))./(y(TP(j)) - y(RWP(j))));
%Angle between reflected wave and vertical
        beta = beta1 + beta2;       %Angle between incident wave and
reflected wave

        %Incident flow calculations
        M1 = ((((x(TP(tpnum)) - x(TP(1))).^2 + (y(TP(tpnum)) -
y(TP(1))).^2).^(0.5))./((tpnum - 1).*t))./a;      %Incident wave Mach
number
%         delta1 = pi./2 - alpha;      %Angle between incident wave
and incident flow
        delta1 = pi./2 - alpha - beta1;      %Angle between incident
wave and incident flow
        theta1 = atan(2.*cot(delta1).*(((M1.*sin(delta1)).^2 - 1)./(2
+ (gamma + cos(2.*delta1)).*M1.^2)));  %Angle of flow deflection
across incident wave

        %Intermediate flow calculations
        M2 = ((((2./(gamma -
1))+(M1.*sin(delta1)).^2)./(((2.*gamma./(gamma -
1)).*(M1.*sin(delta1)).^2) - 1)).^(1./2))./(sin(delta1 - theta1));
%Mach number of flow after incident wave
%         delta2 = pi./2 + beta - alpha - theta1;      %Angle between
reflected wave and flow after incident wave
        delta2 = pi./2 + beta - alpha - theta1 - beta1;      %Angle
between reflected wave and flow after incident wave
        theta2 = atan(2.*cot(delta2).*(((M2.*sin(delta2)).^2 - 1)./(2
+ (gamma + cos(2.*delta2)).*M2.^2)));  %Angle of flow deflection
across reflected wave

        %Reflected wave flow calculations
        M3 = ((((2./(gamma -
1))+(M2.*sin(delta2)).^2)./(((2.*gamma./(gamma -
1)).*(M2.*sin(delta2)).^2) - 1)).^(1./2))./(sin(delta2 - theta2));
%Mach number of flow after reflected wave

        %Output data formatting
        Y(j).description = ['Triple point ' num2str(j)];
        Y(j).beta1 = 180.*beta1./pi;
        Y(j).beta2 = 180.*beta2./pi;
        Y(j).beta = 180.*beta./pi;
        Y(j).M1 = M1;
        Y(j).delta1 = 180.*delta1./pi;
        Y(j).theta1 = 180.*theta1./pi;
        Y(j).M2 = M2;
        Y(j).delta2 = 180.*delta2./pi;
        Y(j).theta2 = 180.*theta2./pi;
        Y(j).M3 =M3;

        Z.Y = Y;
        [Y(j).UncAnalysisData, Y(j).Uncertainties] =
Uncertainties(Z,j,tpnum);     %Calculates uncertainties on all values

        j = j + 1;
        clear beta M2 delta2 theta2 M3
    end
    j = 1;

    X(i).alpha = 180.*alpha./pi;
```

```
    X(i).a = a;
    X(i).Data = Y;

    i = i + 1;
    clear T t x y a alpha M1 delta1 theta1
end

function [B,Unc] = Uncertainties(B,j,tpnum)

i = 1;

d_x = 0.001;   %Uncertainty of x measurements [m]
d_y = 0.001;   %Uncertainty of y measurements [m]
d_T = 0.1;      %Uncertainty of temperature [K]
d_t = 50e-9;    %Uncertainty of delay time [s]

d_a = sqrt((B.gamma.*B.R)./(2.*B.T)).*d_T;      %Uncertainty of sound
speed [m.s^-1]
d_alpha = (sqrt(((B.y(B.TP(tpnum)) - B.y(B.TP(1))).*d_x).^2 +
((B.x(B.TP(tpnum)) - B.x(B.TP(1))).*d_y).^2))./((B.x(B.TP(tpnum)) -
B.x(B.TP(1))).^2 + (B.y(B.TP(tpnum)) - B.y(B.TP(1))).^2);
%Uncertainty of triple point trajectory angle
d_beta1 = (sqrt(((B.y(B.TP(j)) - B.y(B.IWP(j))).*d_x).^2 +
((B.x(B.TP(j)) - B.x(B.IWP(j))).*d_y).^2))./((B.x(B.TP(j)) -
B.x(B.IWP(j))).^2 + (B.y(B.TP(j)) - B.y(B.IWP(j))).^2); %Uncertainty
of angle of incident wave to vertical
d_beta2 = (sqrt(((B.y(B.TP(j)) - B.y(B.RWP(j))).*d_x).^2 +
((B.x(B.TP(j)) - B.x(B.RWP(j))).*d_y).^2))./((B.x(B.TP(j)) -
B.x(B.RWP(j))).^2 + (B.y(B.TP(j)) - B.y(B.RWP(j))).^2); %Uncertainty
of angle of reflected wave to vertical
d_beta = sqrt(d_beta1.^2 + d_beta2.^2);     %Uncertainty of angle
between incident and reflected waves
d_V1 = sqrt(((((B.x(B.TP(tpnum)) - B.x(B.TP(1))).*d_x).^2 +
((B.y(B.TP(tpnum)) -
B.y(B.TP(1))).*d_y).^2)./((sqrt((B.x(B.TP(tpnum)) - B.x(B.TP(1))).^2
+ (B.y(B.TP(tpnum)) - B.y(B.TP(1))).^2)).*B.t)) +
((((B.x(B.TP(tpnum)) - B.x(B.TP(1))).^2 + (B.y(B.TP(tpnum)) -
B.y(B.TP(1))).^2).*d_t.^2)./(B.t.^4)));    %Uncertainty of velocity
of triple point [m.s^-1]
d_M1 = sqrt((B.Y(j).M1.*B.a.*d_a).^2 + (B.a.*d_V1).^2)./(B.a.^2);
%Uncertainty of incident flow Mach number
d_delta1 = sqrt(d_alpha.^2 + d_beta1.^2);  %Uncertainty of incident
flow-incident wave angle

dtheta1_ddelta1 = (((tan(pi.*B.Y(j).delta1./180)).^2).*((B.gamma +
2).*(2.*(B.Y(j).M1.^2).*(cos(pi.*B.Y(j).delta1./180))).^2 +
(2.*B.Y(j).M1.*(cot(pi.*B.Y(j).delta1./180))).^2 +
2.*((B.Y(j).M1.^4).*(1 - B.gamma) - 2.*B.Y(j).M1.^2 +
((csc(pi.*B.Y(j).delta1./180)).^2).*((B.Y(j).M1.^2).*(B.gamma - 1) +
2)))./(((tan(pi.*B.Y(j).delta1./180)).*(2 +
((B.Y(j).M1.^2).*(B.gamma + cos(2.*pi.*B.Y(j).delta1./180))))).^2 +
(2.*(B.Y(j).M1.^2).*((sin(pi.*B.Y(j).delta1./180)).^2) - 1).^2);
%Partial differential used in calculating d_theta1
dtheta1_dM1 =
(4.*tan(pi.*B.Y(j).delta1./180).*(B.Y(j).M1.*((sin(pi.*B.Y(j).delta1.
/180)).^2).*(2 - B.Y(j).M1.^2) + cos(2.*pi.*B.Y(j).delta1./180) +
B.gamma.*B.Y(j).M1 + 1))./(((tan(pi.*B.Y(j).delta1./180)).^2).*(2 +
((B.Y(j).M1.^2).*(B.gamma + cos(2.*pi.*B.Y(j).delta1./180)))).^2 +
4.*((B.Y(j).M1.^2).*((sin(pi.*B.Y(j).delta1./180)).^2) - 1).^2);
%Partial differential used in calculating d_theta1
```

```
d_theta1 = sqrt((dtheta1_ddelta1.*d_delta1).^2 +
(dtheta1_dM1.*d_M1).^2);       %Uncertainty of angle of flow
deflection across incident wave

dM2_dM1 =
(2.*B.Y(j).M1.*((sin(pi.*B.Y(j).delta1./180)).^2).*(((2./(B.gamma -
1)).*(B.Y(j).M1.*sin(pi.*B.Y(j).delta1./180)).^2) - (B.gamma +
3)./(B.gamma - 1))).(((sin(pi.*B.Y(j).delta1./180 -
pi.*B.Y(j).theta1./180)).^2).*(((2.*B.gamma)./(B.gamma -
1)).*(B.Y(j).M1.*sin(pi.*B.Y(j).delta1./180)).^2 - 1).^2);
%Differential used in calculating d_M2
dM2_ddelta1 = (((B.Y(j).M1.*sin(pi.*B.Y(j).delta1./180 -
pi.*B.Y(j).theta1./180)).^2).*sin(2.*pi.*B.Y(j).delta1./180).*(((2.*B
.gamma)./(B.gamma - 1)).*(B.Y(j).M1.*sin(pi.*B.Y(j).delta1./180)).^2
- 1) - (2./(B.gamma - 1) +
(B.Y(j).M1.*sin(pi.*B.Y(j).delta1./180)).^2).*((B.Y(j).M1.^2).*((2.*B
.gamma)./(B.gamma - 1)).*(sin(2.*(pi.*B.Y(j).delta1./180 -
pi.*B.Y(j).theta1./180)).*(sin(pi.*B.Y(j).delta1./180)).^2 +
2.*sin(2.*pi.*B.Y(j).delta1./180).*(sin(pi.*B.Y(j).delta1./180 -
pi.*B.Y(j).theta1./180)).^2) - sin(2.*(pi.*B.Y(j).delta1./180 -
pi.*B.Y(j).theta1./180)))).(((sin(pi.*B.Y(j).delta1./180 -
pi.*B.Y(j).theta1./180)).^2).*(((2.*B.gamma)./(B.gamma -
1)).*(B.Y(j).M1.*sin(pi.*B.Y(j).delta1./180)).^2 - 1)).^2);
%Differential used in calculating d_M2
dM2_dtheta1 = 2.*cos(pi.*B.Y(j).delta1./180 -
pi.*B.Y(j).theta1./180).*((2./(B.gamma - 1) +
(B.Y(j).M1.*sin(pi.*B.Y(j).delta1./180)).^2)./(((2.*B.gamma)./(B.gamm
a - 1)).*(B.Y(j).M1.*sin(pi.*B.Y(j).delta1./180)).^2 -
1)).((sin(pi.*B.Y(j).delta1./180 - pi.*B.Y(j).theta1./180)).^3);
%Differential used in calculating d_M2
d_M2 = sqrt((dM2_dM1.*d_M1).^2 + (dM2_ddelta1.*d_delta1).^2 +
(dM2_dtheta1.*d_theta1).^2);     %Uncertainty of Mach number between
incident and reflected waves

d_delta2 = sqrt(d_beta2.^2 + d_alpha.^2 + d_theta1.^2);
%Uncertainty of intermediate flow-reflected wave angle

dtheta2_ddelta2 = (((tan(pi.*B.Y(j).delta2./180)).^2).*((B.gamma +
2).*(2.*(B.Y(j).M1.^2).*(cos(pi.*B.Y(j).delta2./180))).^2 +
(2.*B.Y(j).M1*(cot(pi.*B.Y(j).delta2./180))).^2 +
2.*((B.Y(j).M1.^4).*(1 - B.gamma) - 2.*B.Y(j).M1.^2 +
((csc(pi.*B.Y(j).delta2./180)).^2).*((B.Y(j).M1.^2).*(B.gamma - 1) +
2)))).(((tan(pi.*B.Y(j).delta2./180)).*(2 +
((B.Y(j).M1.^2).*(B.gamma + cos(2.*pi.*B.Y(j).delta2./180))))).^2 +
(2.*(B.Y(j).M1.^2).*((sin(pi.*B.Y(j).delta2./180)).^2) - 1).^2);
%Partial differential used in calculating d_theta2
dtheta2_dM2 =
(4.*tan(pi.*B.Y(j).delta2./180).*(B.Y(j).M2.*((sin(pi.*B.Y(j).delta2.
/180)).^2).*(2 - B.Y(j).M2.^2) + cos(2.*pi.*B.Y(j).delta2./180) +
B.gamma.*B.Y(j).M2 + 1)).(((tan(pi.*B.Y(j).delta2./180)).^2).*(2 +
((B.Y(j).M2.^2).*(B.gamma + cos(2.*pi.*B.Y(j).delta2./180)))).^2 +
4.*((B.Y(j).M2.^2).*((sin(pi.*B.Y(j).delta2./180)).^2) - 1).^2);
%Partial differential used in calculating d_theta2
d_theta2 = sqrt((dtheta2_ddelta2.*d_delta2).^2 +
(dtheta2_dM2.*d_M2).^2);        %Uncertainty of angle offlow
deflection across reflected wave

dM3_dM2 =
(2.*B.Y(j).M2.*((sin(pi.*B.Y(j).delta2./180)).^2).*(((2./(B.gamma -
1)).*(B.Y(j).M2.*sin(pi.*B.Y(j).delta2./180)).^2) - (B.gamma +
3)./(B.gamma - 1))).(((sin(pi.*B.Y(j).delta2./180 -
```

```
pi.*B.Y(j).theta2./180)).^2).*(((2.*B.gamma)./(B.gamma -
1)).*(B.Y(j).M2.*sin(pi.*B.Y(j).delta2./180)).^2 - 1).^2);
%Differential used in calculating d_M3
dM3_ddelta2 = (((B.Y(j).M2.*sin(pi.*B.Y(j).delta2./180 -
pi.*B.Y(j).theta2./180)).^2).*sin(2.*pi.*B.Y(j).delta2./180).*(((2.*B
.gamma)./(B.gamma - 1)).*(B.Y(j).M2.*sin(pi.*B.Y(j).delta2./180)).^2
- 1) - (2./(B.gamma - 1) +
(B.Y(j).M2.*sin(pi.*B.Y(j).delta2./180)).^2).*((B.Y(j).M2.^2).*((2.*B
.gamma)./(B.gamma - 1)).*(sin(2.*(pi.*B.Y(j).delta2./180 -
pi.*B.Y(j).theta2./180)).*(sin(pi.*B.Y(j).delta2./180)).^2 +
2.*sin(2.*pi.*B.Y(j).delta2./180).*(sin(pi.*B.Y(j).delta2./180 -
pi.*B.Y(j).theta2./180)).^2) - sin(2.*(pi.*B.Y(j).delta2./180 -
pi.*B.Y(j).theta2./180)))./((((sin(pi.*B.Y(j).delta2./180 -
pi.*B.Y(j).theta2./180)).^2).*(((2.*B.gamma)./(B.gamma -
1)).*(B.Y(j).M2.*sin(pi.*B.Y(j).delta2./180)).^2 - 1)).^2);
%Differential used in calculating d_M3
dM3_dtheta2 = 2.*cos(pi.*B.Y(j).delta2./180 -
pi.*B.Y(j).theta2./180).*((2./(B.gamma - 1) +
(B.Y(j).M2.*sin(pi.*B.Y(j).delta2./180)).^2)./(((2.*B.gamma)./(B.gamm
a - 1)).*(B.Y(j).M2.*sin(pi.*B.Y(j).delta2./180)).^2 -
1)).//((sin(pi.*B.Y(j).delta2./180 - pi.*B.Y(j).theta2./180)).^3);
%Differential used in calculating d_M3
d_M3 = sqrt((dM3_dM2.*d_M2).^2 + (dM3_ddelta2.*d_delta2).^2 +
(dM3_dtheta2.*d_theta2).^2);     %Uncertainty of Mach number after
reflected wave

%Uncertainty output formatting
Unc.d_x = d_x;
Unc.d_y = d_y;
Unc.d_T = d_T;
Unc.d_t = d_t;
Unc.d_a = d_a;
Unc.d_alpha = 180.*d_alpha./pi;
Unc.d_beta1 = 180.*d_beta1./pi;
Unc.d_beta2 = 180.*d_beta2./pi;
Unc.d_beta = 180.*d_beta./pi;
Unc.d_M1 = d_M1;
Unc.d_delta1 = 180.*d_delta1./pi;
Unc.d_theta1 = 180.*d_theta1./pi;
Unc.d_M2 = d_M2;
Unc.d_delta2 = 180.*d_delta2./pi;
Unc.d_theta2 = 180.*d_theta2./pi;
Unc.d_M3 = d_M3;

B = rmfield(B,'Y');

function A = CoordTrans(X)

i = 1;
j = 1;
k = 1;

[a,b] = size(X);

while i <= b
    delx = X(i).delx;
    dely = X(i).dely;

    xg = X(i).xo - X(i).xo(a,1);
    yg = -(X(i).yo - X(i).yo(a,1));
    [c,d] = size(xg);
```

```
    while j <= c
        Xpol(j,:) = polyfit(xg(j,:),[0:delx:((d-1).*delx)],d-1);
        j = j + 1;
    end
    j = 1;
    while j <= d
        Ypol(j,:) = polyfit(yg(:,j)',[((c-1).*dely):-dely:0],c-1);
        j = j + 1;
    end
    j = 1;

    while j <= d
        Xpolx(j,:) = polyfit(yg(:,1),Xpol(:,j),c-1);
        j = j + 1;
    end
    j = 1;
    while j <= c
        Ypolx(j,:) =polyfit(xg(a,:),Ypol(:,j)',d-1);
        j = j + 1;
    end
    j = 1;

    xs = X(i).x - X(i).xo(a,1);
    ys = -(X(i).y - X(i).yo(a,1));

    f = length(xs);

    while k <= f
        while j <= d
            xpoli(j) = polyval(Xpolx(j,:),ys(k));
            j = j + 1;
        end
        j = 1;
        while j <= c
            ypoli(j) = polyval(Ypolx(j,:),xs(k));
            j = j + 1;
        end
        j = 1;

        xt(k) = polyval(xpoli,xs(k));
        yt(k) = polyval(ypoli,ys(k));

        k = k + 1;
        clear xpoli ypoli
    end
    k = 1;
    X(i).xtrue = xt;
    X(i).ytrue = yt;
    i = i + 1;
    clear xg yg  Xpol Ypol Xpolx Ypolx xs ys c xt yt
end

A = X;
```

Appendix C – Solid Edge Drawings

The design drawings of the shock tube insert of the 20 degrees are shown in this section.

Appendix D – Xenon Light Sources Specifications

The following section shows the full specifications of the two xenon light source (15W and 60 W) from Hamamatsu.

Appendix E – Photographs DVD

All the photographs taken during the project are given in separated folders of the DVD attached at the end of this report.